Charged Fusion Product Diagnostic on the Alcator C-Mod Tokamak

D.H.C. Lo

November 1996

Charged Fusion Product Diagnostic
on the Alcator C-Mod Tokamak

by

Daniel Hung Chee Lo

B.S., Nuclear Engineering, University of Wisconsin - Madison (1988)

Submitted to the Department of Nuclear Engineering
in partial fulfillment of the requirements for the degree of

Doctor of Philosophy

at the

MASSACHUSETTS INSTITUTE OF TECHNOLOGY

October 1996

Author ....
Department of Nuclear Engineering
October 14, 1996

Certified by ....
Réjean L. Boivin
Research Scientist, Plasma Fusion Center
Thesis Supervisor

Certified by ....
Richard D. Petrasso
Principal Research Scientist, Plasma Fusion Center
Thesis Supervisor

Certified by ....
Ian H. Hutchinson
Professor, Department of Nuclear Engineering
Thesis Reader

Accepted by ....
Prof. Jeffrey P. Freidberg
Chairman, Departmental Committee on Graduate Students

Charged Fusion Product Diagnostic
on the Alcator C-Mod Tokamak

by

Daniel Hung Chee Lo

Abstract

This thesis presents the development and experimental results of a charged fusion product (CFP) spectrometer for the Alcator C-Mod tokamak. Based on an ion-implanted silicon detector, the spectrometer has a reentrant design that brings the detector inside the vacuum vessel of Alcator C-Mod for intercepting CFPs. A 3-dimensional orbit code, EPSILON, has been written to calculate the CFP detection efficiency. The calculated efficiency has an overall uncertainty of 29% due to uncertainties in the poloidal field structure, the dimension/location of the spectrometer, and the fusion source profile.

The detection of D-D protons has made possible the independent measurements of the fusion rate in Alcator C-Mod. General agreement with fusion rates measured with the neutron diagnostic system were found. The plasma current dependence of the D-D proton flux agrees well with results from modelling by EPSILON. From the measured D-D proton linewidths in the energy spectrum, central ion temperature measurements have been made in ohmic discharges. These were found to compare well with the temperature measurements made from other diagnostics.

Through benchtop experiments and MCNP modeling, competing signals from neutron-capture γ rays and neutrons generated during plasma discharges are found to limit the operating range of the CFP spectrometer. Given the finite counting capability of the electronics, these counts dominate at high neutron rates. Consequently, fusion rate measurements have been possible for discharges with neutron rate of up to about 6×10^{12} /s, whereas satisfactory ion temperature measurements have been restricted to cases where the neutron rate is below 0.4×10^{12} /s. The combined effects of detector volume reduction, processing speed enhancement of the electronics, and optimized detector shielding need to be studied to eradicate the problem.

Thesis Supervisor: Réjean L. Boivin
Title: Research Scientist, Plasma Fusion Center

Thesis Supervisor: Richard D. Petrasso
Title: Principal Research Scientist, Plasma Fusion Center

Acknowledgments

I would like to thank my supervisors Réjean Boivin and Richard Petrasso for their advice and assistance at different stages of my graduate student career here. Heartfelt thanks to Réjean for his guidance, tolerance, understanding, and encouragement that have made the completion of my thesis possible and have kept me from going over the edge. And to Rich, thanks for introducing me to the many aspects of scientific research. I also thank Prof. Ian Hutchinson for his critical reading of my thesis and his many probing questions.

A warm thank-you also goes out to the many technicians, scientisits and engineers, and support staff of Alcator C-Mod. I want to especially thank Prof. Kevin Wenzel for his advice and friendship. I thank Dr. Catherine Fiore and Dr. John Rice for their discussion and assistance on various technical issues. I thank Dr. Bob Granetz for entertaining my many silly questions even when I caught him at the worst times. And to Frank Silva, Ed Fitzgerald, and Bob Childs, thanks again and again!

Thanks to my parents and my sister for their constant love and belief in me throughout my years at MIT. It brings me comfort and stability to know that you have always been behind me. And then there are all the friends, especially Vinh and PJ, who have kept me afloat when the weight felt too overwhelming. I also especially treasure the friendship of Maria, Mercedes, Gerry, Bob G., Chi Kang, Jody, Jim L., Jim R., Dimitri, and Cristina. Saving the best for last, I express my love and gratitude to Judith for having gone through it all with me.

For Judith

Contents

List of Figures

12

List of Tables

15

Chapter 1

Introduction

1.1 Fusion

The thermonuclear reaction or fusion of light nuclei creates fusion products and releases immense amounts of energy. Such thermonuclear reactions are responsible for the energy production and nucleosynthesis of the elements in stars. Almost all the energy sources on earth can be traced back to fusion reactions that took place in the sun.

The importance of fusion as a major energy source of the future with an essentially inexhaustible fuel supply was generally recognized decades ago [1]. Fusion reactors will be inherently safe from possible nuclear excursions and can present fewer radioactivity problems than fission reactors. Compared to the burning of fossil fuels, fusion is also less damaging to the environment. In addition, very efficient energy conversion should be possible in the future with fusion reactors exclusively. Therefore, fervent research activities in fusion have always evolved around the goal of harnessing thermonuclear fusion on earth safely and economically to provide power commercially for years to come.

The most relevant reactions in controlled thermonuclear fusion research are the

two particle branches of the D-D reaction:

$$D + D \longrightarrow p\,(3.02 \text{ MeV}) + T\,(1.01 \text{ MeV}) \tag{1.1}$$

$$D + D \longrightarrow n\,(2.45 \text{ MeV}) + {}^3\text{He}\,(0.82 \text{ MeV}) \tag{1.2}$$
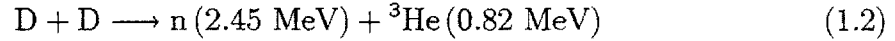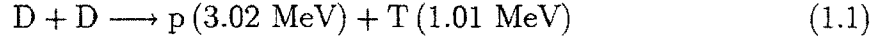
each of which occurs with roughly equal probability in the temperature regimes of modern-day fusion research. (The kinetic energy that each product of the reaction has in the center-of-mass frame of the system has been included.) The products T and ^{3}He are themselves fusible with deuterium, resulting in the secondary reactions

$$D + {}^3\text{He} \longrightarrow p\,(14.7 \text{ MeV}) + \alpha\,(3.6 \text{ MeV}) \tag{1.3}$$

$$D + T \longrightarrow n\,(14.1 \text{ MeV}) + \alpha\,(3.5 \text{ MeV}). \tag{1.4}$$
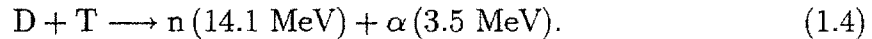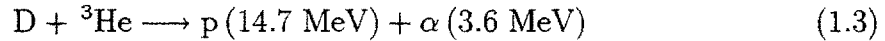
In fact, the D-T reaction, having the highest cross section for deuteron energies of less than 400 keV, is really the most promising fuel cycle. However, since tritium is radioactive (beta emitter with a half-life of 12.3 years), special handling is required if used as a fuel for research. Thus, fusion research has primarily been done with the D-D primary fuel cycle.

1.2 Tokamak

To achieve fusion, the nuclei of the fuel particles have to be brought to close contact (of order a Fermi or 10^{-15} m) for the reaction probability to become appreciable. Thus, the strong mutual repulsion of the positively charged nuclei has to be overcome. The most practical method is to heat the fuel particles as a whole to a sufficiently high temperature (of order 10 keV). This method is referred to as thermonuclear fusion.

18

At such temperature, the fuel particles are fully ionized. The resulting collection of ions and electrons is called a plasma.

How does one contain such a fuel mixture for fusion to take place in a controlled fashion? The most advanced design of a containment scheme is a torus known as the tokamak, which is a closed magnetic field device. Figure 1.1 is a schematic of a tokamak. The name is an acronym extracted from the Russian words TOroidalnaya KAmera ee MAgnitaya Katushka which stand for "Toroidal Chamber with Magnetic Coil." Tokamaks are designed to operate with toroidal magnetic field coils and plasma currents which act to magnetically confine plasma ions (like deuterons) and electrons. The principal magnetic field is the toroidal field which is provided by external magnetic field coils. The presence of a substantial toroidal plasma current, which is a fundamental feature of the tokamak design [2,3], gives rise to a poloidal magnetic field essential to the plasma equilibrium. There are also external poloidal field coils in the design — equilibrium coils necessary for the vertical stability of the plasma, and ohmic transformer coils for the ohmic heating of the plasma. The objective is to confine the fuel ions magnetically in this device to a high enough density and heat it to a high enough temperature (often with other forms of auxiliary heating) for fusion to occur.

1.3 Charged Fusion Products as a Diagnostic

In the presence of a magnetic field B, a charged particle with charge q, mass m, and velocity v undergoes a helical motion about field lines, characterized by the gyroradius (also called the Larmor radius)

$$\rho = \frac{mv_\perp}{qB} = \frac{v_\perp}{\omega_c}. \tag{1.5}$$

where ω_c is the cyclotron frequency, and $v_\perp$ is the component of the velocity that is perpendicular to the magnetic field vector $\mathbf{B}$.
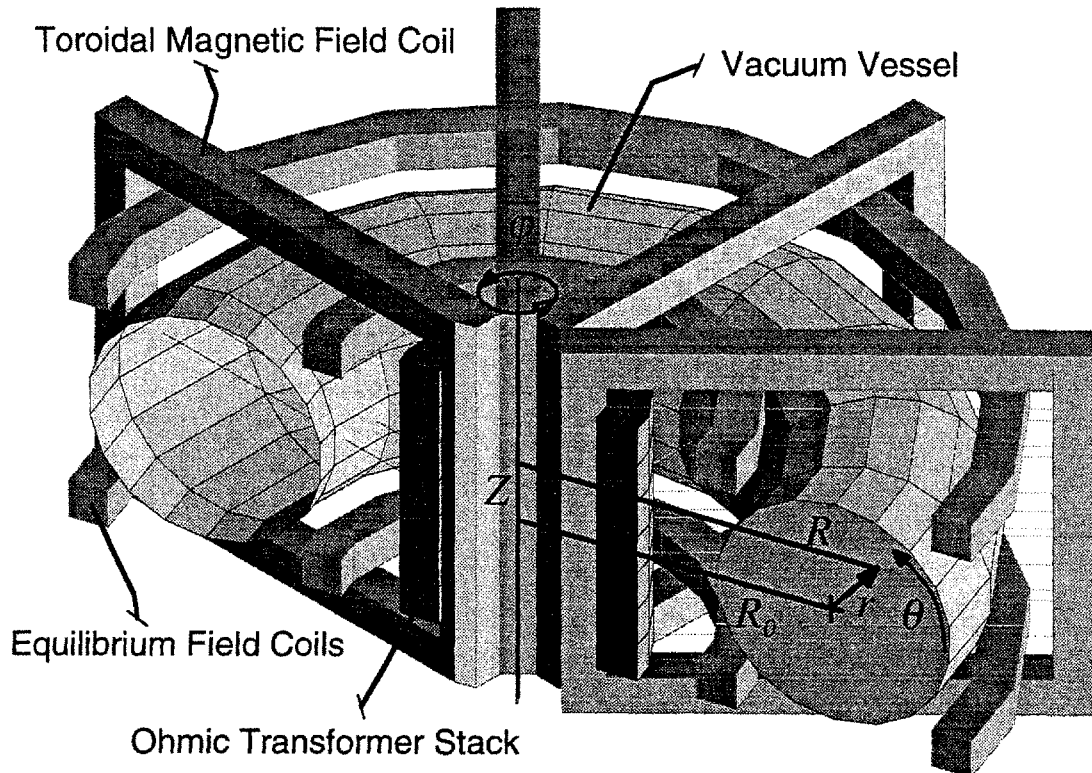
Figure 1.1: Schematic of a tokamak, indicating its major components. The toroidal coordinate system (R, Z, φ) and cylindrical coordinate system (r, θ, φ) are interchangeable. (Figure courtesy of Darren Garnier)

The poloidal field from the plasma current changes the field structure from a purely toroidal one to one that has a slight twist poloidally as well. A measure of this can be given, in the cylindrical approximation, by the quantity

$$q(r) = \frac{rB_o}{R_0 B_\theta} \qquad (1.6)$$

which is called the safety factor. Thus, charged particles gyrate about toroidal field lines that themselves are rotating poloidally around the plasma center in the tokamak geometry.

Now, a charged particle actually does not remain gyrating about the same field line when drift motions are present. The two most dominant drifts present in the tokamak are the ∇B drift and curvature drift (see, for instance, Ref. [4]). The ∇B drift comes about because the magnetic field, dominated by the toroidal field, is inversely proportional to the major radius R. This sets up a gradient ∇B which points radially inward in the tokamak. The curvature drift arises from the centrifugal force felt by the particle as it moves along the curved field lines. These two drifts in the tokamak are in the same direction, either up or down. Figure 1.2 shows the poloidal projections of different orbits followed by charged fusion products (CFPs) in a tokamak. The drift direction is down in this case. The particles can be classified as either being trapped or passing.

To understand these orbits, the parallel and perpendicular components (both relative to the local magnetic field) of a particle's energy, $E_\parallel$ and $E_\perp$, have to be examined. Even though the total energy of a particle is conserved (*i.e.*, $E = E_\parallel + E_\perp$), $E_\parallel$ and $E_\perp$ are changing with the local magnetic field. A quantity called the magnetic moment μ is invariant under a spatially and temporally varying magnetic field (see, for instance, Ref. [4]). It has the expression

$$\mu = \frac{E_\perp}{B} = \frac{mv_\perp^2}{2B}. \qquad (1.7)$$

21
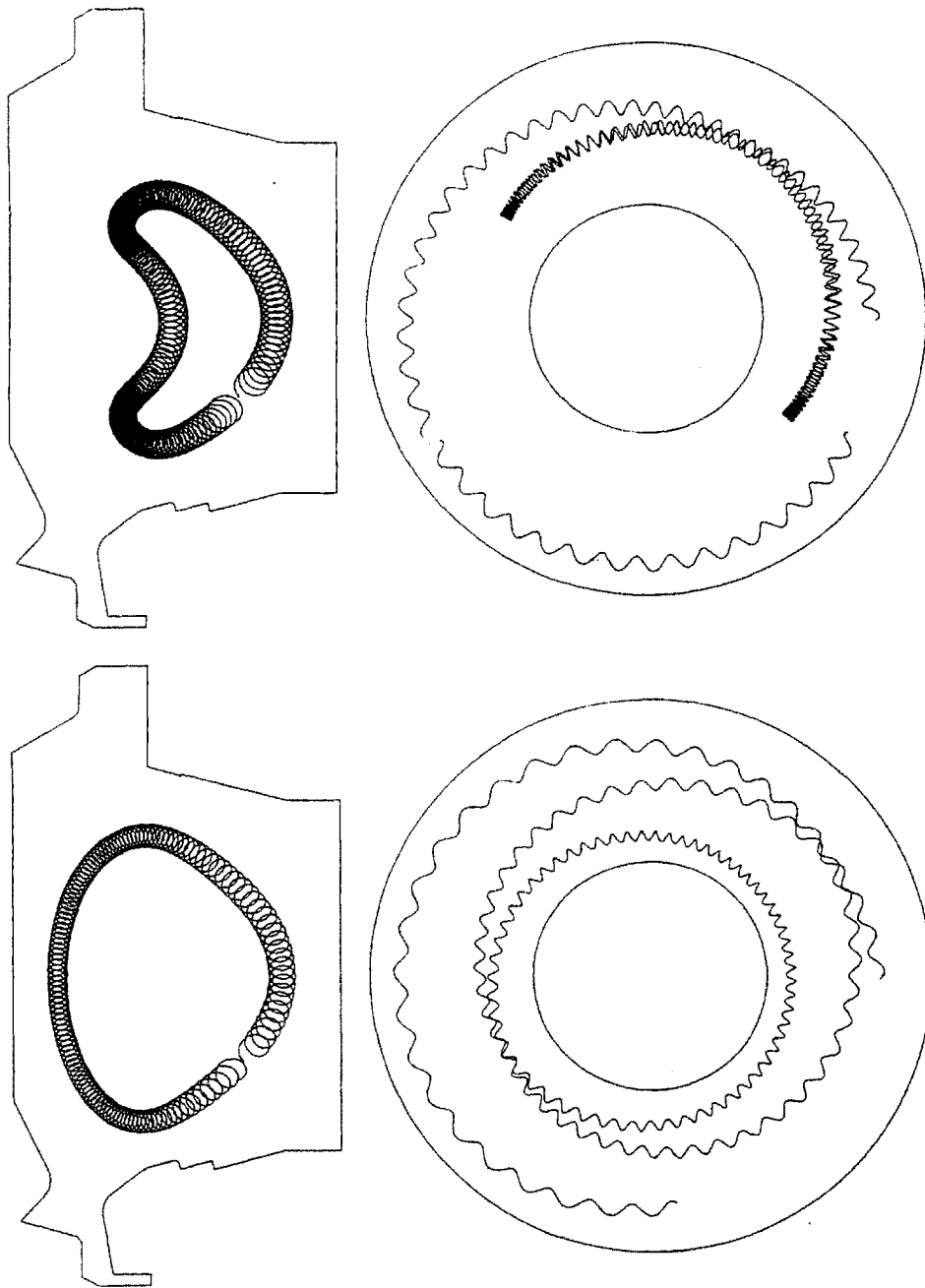
Figure 1.2: Charged fusion product orbits in tokamak, illustrating the trapped and passing orbits, poloidal and top views.

Now as a particle gyrates about field lines that bring it up the magnetic gradient (which is radially pointing inward in the tokamak), $v_\perp$ has to increase according to Eq. (1.7) such that μ remains constant. In turn, the parallel velocity component $v_\parallel$ of the particle decreases such that E is conserved.

A trapped orbit comes about when a particle's parallel velocity (parallel to the local magnetic field) continually transforms to its perpendicular velocity as it moves up the magnetic field gradient. A particle is trapped when its motion brings it to a point spatially such that the decreasing $v_\parallel$ vanishes and then becomes negative. The particle's translational motion will reverse its direction. However, the particle's guiding center will not retrace its steps because of the drift motion. These trapped orbits are also known as banana orbits in reference to their appearance. The point where $v_\parallel = 0$ is known as the banana tip. For another particle which has more of its energy in the parallel direction, the reversal in motion may not occur and the resulting orbit is a passing orbit.

Considering trapped orbits, the loss of charged particles should be significant when its typical banana width Δ becomes comparable to or larger than about half the minor radius [5], i.e.

$$\Delta \approx q\sqrt{\frac{R}{a}}\rho_{tor} > \frac{a}{2} \tag{1.8}$$

where q is the safety factor, R is the plasma major radius, a is the plasma minor radius, and ρ_{tor} is the toroidal gyroradius. If there is a population of sufficiently energetic ions, e.g. CFPs, a fraction of this population should be able to escape such a confinement scheme. This escaping fraction naturally can be used for diagnostic purposes.

The idea of using CFPs as a diagnostic of the plasma condition in fusion research is not new [6]. Even early on in fusion research [6], CFPs have been used as a diagnostic of the plasma condition. After the fusion program shifted emphasis from the open magnetic configurations to toroidal schemes which eliminated end losses,

however, detection of fusion products became more centered on the 2.45 MeV neutron from the D-D reaction because it is escaping readily from the plasma, unaffected by the presence of a closed toroidal magnetic field. Charged particles, on the other hand, have to have attained energies of order 1 MeV before a considerable fraction escapes the confinement. Even then, charged particle detectors have to be placed relatively close to the plasma, almost always requiring vacuum operation. The proximity of the detector to the plasma means that the detector has to operate in a hostile environment.

However, CFPs do have some decided advantages that make them an attractive candidate for diagnosing the plasma. Both CFP and neutron techniques are non-perturbative to the plasma. However, unlike neutrons, CFPs deposit their full energies in solids in short distances. Therefore, detectors of charged particles with essentially 100% detection efficiency can be made of very compact solid materials. In addition, very good energy resolution is possible when detecting charged particles, compared to neutrons. Furthermore, for certain aneutronic reactions, like the D-^{3}He reaction (see Eq. (1.3)), CFPs are the only way to measure the fusion yield. The physics issues that have been studied in the fusion community with escaping CFPs are very diverse. They include: α-emission profile [7], ^{3}He minority heating [8–10], plasma density measurements [11], ion temperature measurements [12–14], MeV ion confinement through ^{3}He burnup [15], and various loss mechanisms [5,16].

In this thesis, the development of a CFP spectrometer for the Alcator C-Mod tokamak is described. The original goal of deploying this diagnostic was to evaluate the effectiveness of ^{3}He minority RF heating through the broadened spectrum of unconfined 14.7 MeV protons from D-^{3}He reactions. Due to count-rate related problems that will be discussed in Chapter 8, this goal was not attained. Despite the problems, the spectrometer was able to measure the fusion rate (see Chapter 6) and the central ion temperature (see Chapter 7). These issues will be discussed in detail.

Parameter	Symbol	Nominal (Max.) Value	Unit
Major Radius	R_0	0.67	m
Minor Radius	a	0.21	m
Toroidal Field	B_T	5.3 (9)	T
Plasma Current	I_p	1.2 (3)	MA
Auxiliary Heating	P_{ICRF}	3.5 (8)	MW
Line average density	$< n_e >$	$\leqslant 1.1 \times 10^{21}$	m^{-3}
Electron temperature	T_e	$\leqslant 6$	keV
Elongation	κ	0.95–1.85	
Triangularity	δ	$\leqslant 0.4$	
Flat-top duration		~ 1 (7)	s
Plasma cross-section		diverted	

Table 1.1: Some of the important parameters of Alcator C-Mod. Nominal values are given with values in parentheses showing maximum values (some planned for future operation).

1.4 The Alcator C-Mod Tokamak

1.4.1 Machine Characteristics

Alcator[1] C-Mod is a high-magnetic-field high-density compact tokamak, following the same approach taken by the previous tokamaks in the Alcator series at MIT [17]. Table 1.1 lists some of the important parameters of Alcator C-Mod.

A cross section of Alcator C-Mod is shown in Fig. 1.3 depicting the overall structure of the machine. The important features of Alcator C-Mod include its capability to produce highly elongated single or double null diverted plasmas, its large auxiliary ICRF heating capability (ultimately up to 8 MW), and its molybdenum-tiled first wall, to name a few.

---

[1]Derived from ALtus CAmpus TORus, Latin meaning high field torus.
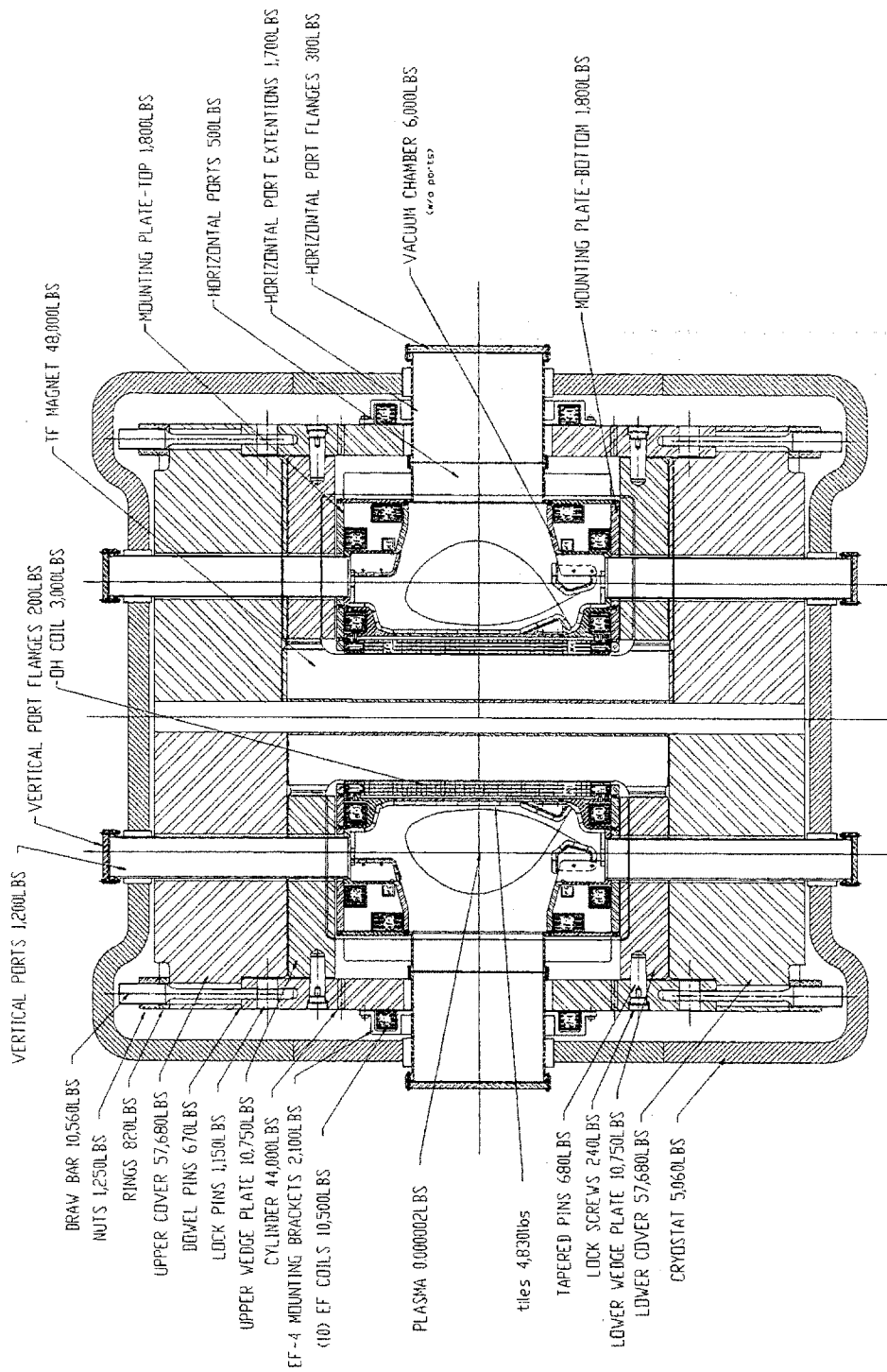
Figure 1.3: Cross-section of the Alcator C-Mod tokamak.

1.4.2 Description of Related Diagnostics and Systems

Neutron Diagnostics

Measurement of the global neutron production is performed with an array of detectors [18]: twelve fission chambers (with enriched ^{235}U) of varying sensitivity, four BF_3 counters, and four ^3He detectors. These are distributed in four moderator-detector stations around the experimental cell of Alcator C-Mod. The fission chambers were selected to cover the entire range of neutron rates from deuterium operation, between 10^{11} and 10^{16} neutrons per second. There is sufficient overlap between the operating ranges to allow cross calibration between detectors.

HIREX

A five-chord high-resolution x-ray (HIREX) spectrometer [19] provides measurements of the ion temperature profile. The measurement is based on the Doppler broadening of x-ray impurity lines, in this case, lines of hydrogen-like and helium-like argon injected into the machine. The spectrometer array was designed according to the compact von Hamos geometry due to space limitations inherent in the small size of Alcator C-Mod. The spectra are typically collected every 50 ms during a discharge for good counting statistics.

Two-Color Interferometer

A Two-Color Interferometer (TCI) system is used in Alcator C-Mod to measure the electron density with high spatial (≈ 2 cm) and temporal (≤ 1.0 ms) resolution [20]. The interferometer is in a two pass Michelson configuration. Ten CO_2 and four HeNe channels view the central 20 cm of the plasma through a vertical port. Each channel provides a line-integrated measurement of the electron density. The chordal measurements are inverted using standard matrix inversion techniques to yield the electron density profile. In addition to providing density profile information, the

TCI also supplies a signal to the hybrid control system of Alcator C-Mod for density feedback.

ICRF Heating

Alcator C-Mod utilizes two Radio Frequency (RF) generating units to deliver up to 4 MW of Ion Cyclotron Range of Frequency (ICRF) power through two antennae closely positioned to the plasma edge. In one mode of operation, the launched waves are resonant with the cyclotron motion of minority hydrogen ions (deuterium is the majority species) at the magnetic axis. For the transmitter frequency of 80 MHz, the resonance occurs at 5.3 T, the nominal magnetic field of Alcator C-Mod. In another mode, the minority ions are ^{3}He. The magnetic field on axis will then be at 8 T for heating to take place across the plasma center.

Magnetic and Current Diagnostics

An extensive array of magnetic diagnostics are installed to measure the magnetic fields, magnetic fluxes, plasma current, and coil currents of the tokamak. The EFIT code [21] takes these measurements and reconstructs the equilibria during the discharge. The magnetic geometry from EFIT is used directly in the calculation of the detection efficiency of the CFP spectrometer. (See Chapter 5.)

Hard x Ray Monitor

As will be discussed in Chapter 8, the charged fusion product spectrometer located inside the C-Mod vessel is sensitive to hard x rays. A hard x ray monitoring system based on a bismuth germanate ($Bi_4Ge_3O_{12}$) crystal scintillator is installed on C-Mod at K port. The high Z (=83) of bismuth gives a high photoelectric cross section (high counting efficiency) though the light output is low (low energy resolution) compared to conventional scintillation materials like NaI(Tl).

1.5 Thesis Organization

The thesis is structured as follows.

Chapter 2. Preparatory work with CFP detection performed with a Cockcroft-Walton linear accelerator is summarized. The accelerator acts as a fusion-product source through beam-target fusion.

Chapter 3. An experimental study of the charged particle sensitive depth of silicon-based detectors is reviewed.

Chapter 4. The design and construction of the CFP spectrometer for Alcator C-Mod is examined in detail.

Chapter 5. In this chapter, two orbit-following computer codes, EPSILON and PROMPT, are introduced. EPSILON is a 3-D code for calculating the detection efficiency of the CFP spectrometer. PROMPT is a Monte-Carlo simulation code for studying prompt losses of CFPs in C-Mod.

Chapter 6. Measurements of the fusion rate with the CFP spectrometer are presented and these are compared to measurements made by the neutron diagnostic system. Prompt losses of fusion protons as a function of the plasma current is also presented.

Chapter 7. The linewidths of the CFP spectra form the basis of the central ion temperature measurements made. The theory and the experimental data are discussed here and a comparison is made with the ion temperature measurements from other diagnostics.

Chapter 8. The development of the CFP spectrometer as a plasma diagnostic in Alcator C-Mod has been hampered by count rate related problems. The nature of this problem is identified and explained in this chapter.

Chapter 9. In the concluding chapter, a summary and suggestion of future work can be found.

Chapter 2

Charged Fusion Products from the Cockcroft-Walton Linear Accelerator

2.1 Cockcroft-Walton Linear Accelerator

The rebuilding of a 150-kV Cockcroft-Walton linear accelerator, located in a radiation vault area with $\sim$3-foot thick concrete walls, has been instrumental in the development of the charged fusion product (CFP) spectrometer for Alcator C-Mod. The accelerator was manufactured (*circa* 1962) by Texas Nuclear Corp. [22], but originally as a neutron source. It has been refurbished for use as a well-calibrated source of fusion products – charged particles [23], neutrons [23,24], gamma rays [25] – and Particle-Induced X-Ray Emissions [26].

The major components of the accelerator are shown schematically in Fig. 2.1. The ion source consists of a plasma bottle, radio-frequency (RF) oscillator rings, an extraction anode, a compression solenoid, and a focus electrode. An RF field (about 60 MHz) applied to the oscillator rings causes intense ionization of the source gas (*e.g.*, D or ^{3}He), resulting in a plasma discharge. The magnetic field from the solenoid

31
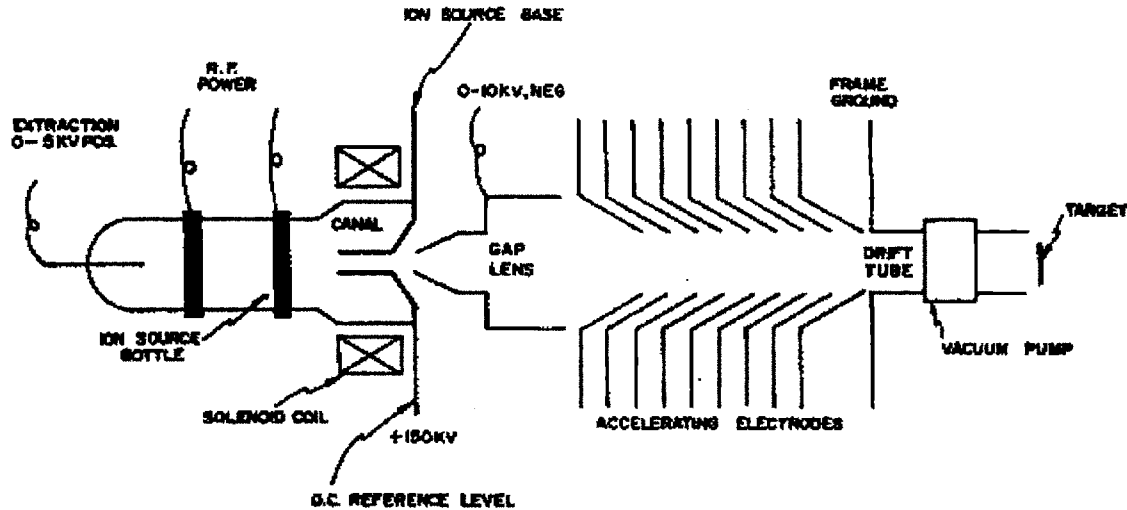
Figure 2.1: Schematic of the Cockcroft-Walton accelerator. Positive ions (*e.g.*, D or ^{3}He) produced in a radio-frequency type ion source are extracted by applying a potential across the ion source bottle. After extraction, the ions are focused by a gap lens focus electrode before they are accelerated through a potential of up to 150 kV distributed between 10 electrodes. The ions ultimately hit a water-cooled target where "beam-target" fusion products are produced. Voltages shown are relative to ion source base.

compresses the plasma and optimizes molecular break-up and gas ionization [22]. Ions are forced from the bottle by application of a potential of up to +5 kV on the extraction anode. After extraction, some beam focusing is achieved by applying up to -10 kV on a gap lens focus electrode located just downstream from the ion source.

The ions leave the gap lens focus electrode and enter the field of the accelerating column where they are accelerated through a potential of 150 kV. The method of producing this potential in the accelerator was invented by Schenkel and Greinacher and first used by Cockcroft and Walton [27] in 1932 in the construction of their accelerator. In these capacitor-rectifier circuits a transformer feeds alternating current of a smaller voltage into a rectifying and multiplying apparatus, called the cascade generator, and through the arrangement of capacitors and diodes the voltage is multiplied.

After leaving the accelerating tube, the ions first drift through a potential-free drift
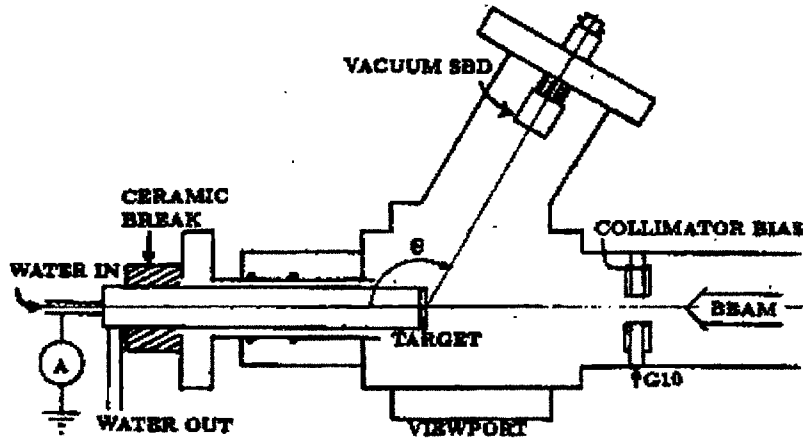
Figure 2.2: Schematic diagram of the target chamber. The water-cooled target and the collimator are positively biased to restrain secondary electrons from leaving. The beam current on target is measured directly. A surface barrier diode at angle θ is shown operating in vacuum to detect charged fusion products.

tube. The beam size is limited by a 1-cm-diameter stainless-steel collimator that is electrically insulated from the drift tube and located about 15 cm upstream from the target. (The collimator is biased at +300 V above ground to attract secondary electrons potentially created at the collimator edge.) The beam then strikes a solid target which is centrally located inside a target chamber for diagnostic access (see Fig. 2.2). The beam current on target is measured by a micro-ammeter connected between the target and ground. The water-cooled target is biased at +200 V to attract secondary electrons generated at the target surface and thus avoid misleading current measurement. The target chamber may be separated from the beam line by a gate valve to allow target changes without bringing the entire accelerator to air.

To minimize scattering of the ion beam, a vacuum is maintained in the entire system by a turbomolecular pump. The base pressure is ~ 0.5-1.0×10^{-6} torr, and the operating pressure ranges from 5×10^{-6} to about 5×10^{-5} torr depending on beam power, target conditions, and the particular diagnostics installed (e.g., vacuum is degraded when we use an ultra-thin-window gas-flow proportional counter to measure
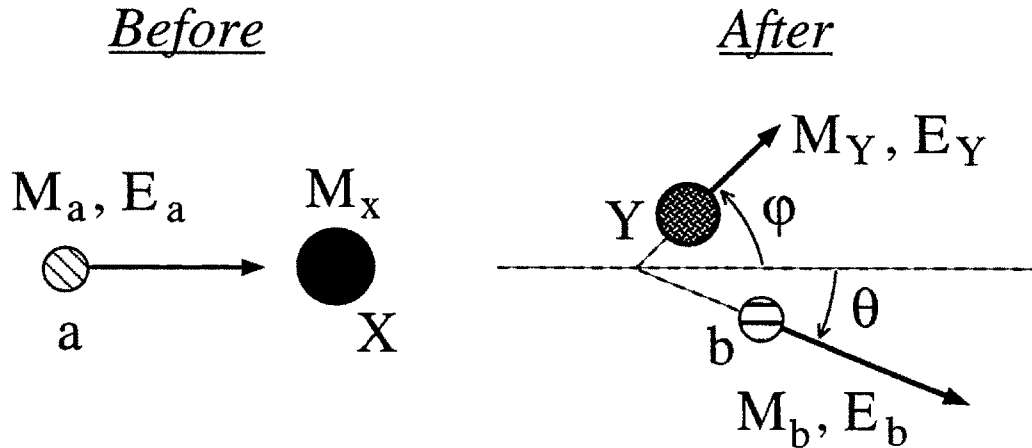
Before   **After**

Figure 2.3: Before and after a binary nuclear reaction in the laboratory system. The angle $0° \leq \theta \leq 180°$ is measured with respect to the beam (species a) direction. The system's dynamics are confined to one plane.

low energy x rays).

To achieve fusion [D(D,p)T, D(D,n)^{3}He, D(^{3}He,p)α, T(D,n)α] with the accelerator, the target material has to hold the stationary fusing isotope, *i.e.*, deuterium or tritium. This has been made possible by the use of loaded erbium ($ErD_{1.92}$, $ErT_{1.92}$) targets from Sandia National Laboratory.[1] The maximum reaction rates, normalized to the beam current, have been $R_{DD} \simeq 9 \times 10^5/(s~\mu A)$, $R_{D^3He} \simeq 3 \times 10^4/(s~\mu A)$, and $R_{DT} \simeq 4 \times 10^7/(s~\mu A)$.

2.2 Beam Target Reaction Kinematics

To understand some of the results, beam target reaction kinematics have to discussed. Consider a nuclear reaction of the type $X(a,b)Y$ (see Fig. 2.3) where a stationary target particle X is bombarded by particle a, resulting in two products, say, b and Y.

---

[1]Courtesy of C. L. Ruiz and R. J. Leeper, Sandia National Laboratory, Albuquerque, New Mexico 87185.
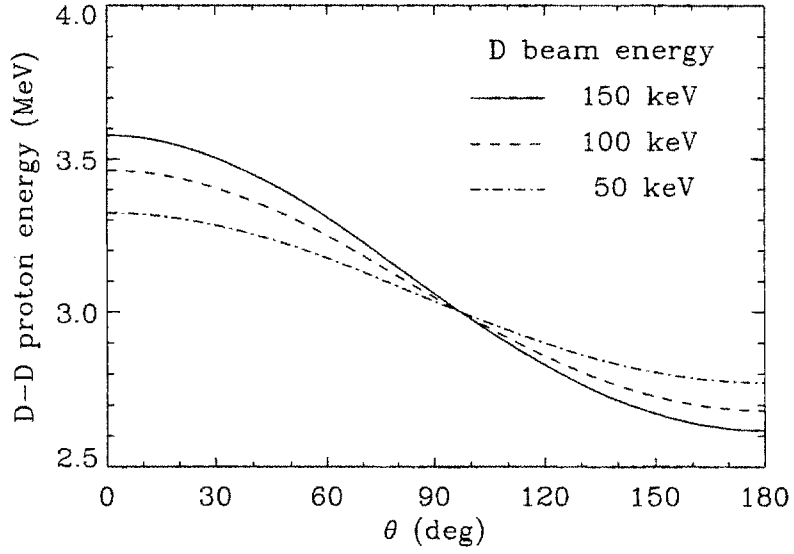
Figure 2.4: Kinematics of the D-D proton reaction illustrating the energy variation for D beam energies of 50 keV, 100 keV, and 150 keV.

(For bombarding energies below 100 MeV, it is usually the case that two products are generated [28].) In the laboratory system, conservation of energy gives

$$E_a + Q = E_b + E_Y \tag{2.1}$$

where Q is the nuclear disintegration energy (i.e. the change in the total rest mass in the system in the sense of mass-energy conservation). Since there are only two products in the reaction, θ and φ have to be coplanar and the dynamics of the system are confined to this two-dimensional plane. Conservation of linear momentum, thus, yields the two equations

$$\sqrt{2\,M_a\,E_a} = \sqrt{2\,M_b\,E_b}\cos\theta + \sqrt{2\,M_Y\,E_Y}\cos\varphi, \tag{2.2}$$

$$0 = \sqrt{2\,M_b\,E_b}\sin\theta - \sqrt{2\,M_Y\,E_Y}\sin\varphi. \tag{2.3}$$

35

These three conservation equations can be solved simultaneously (as outlined in Ref. [29]) to give the so-called Q equation:

$$Q = E_b \left(1 + \frac{M_b}{M_Y}\right) - E_a \left(1 - \frac{M_a}{M_Y}\right) - \frac{2}{M_Y} \sqrt{M_a E_a M_b E_b} \cos \theta \qquad (2.4)$$

This can be viewed and solved as a quadratic in $\sqrt{E_b}$. Therefore

$$\sqrt{E_b} = v \pm \sqrt{v^2 + w}, \qquad (2.5)$$

where

$$v = \frac{\sqrt{M_a M_b E_a}}{M_b + M_Y} \cos \theta, \qquad (2.6)$$

$$w = \frac{M_Y Q + E_a (M_Y - M_a)}{M_b + M_Y}. \qquad (2.7)$$

So given the knowledge of the Q value of the reaction and masses of all the reactants and products (in fact, only mass ratios are necessary), the fusion product energy observed in the laboratory depends on the beam energy and the angle of observation, θ, relative to the beam direction (see Fig. 2.2). The energetically possible reactions are those for which $\sqrt{E_b}$ is real and positive. Considering the fusion reactions [Eqs. (1.1)—(1.4)] relevant to the Cockcroft-Walton accelerator, in which M_a, M_b, M_X, and M_Y are all of the same order of magnitude, and the limiting 150 kV accelerator voltage ($Q \gg E_a = 150 keV$), w is always positive. Thus, the minus sign in Eq. (2.5) is unphysical and dropped. An illustration of this kinematic effect on the fusion product energy is shown in Fig. 2.4 for D-D protons. For a given accelerator voltage or beam energy, the D-D proton energy is seen to be maximized at $\theta = 0°$ and minimized at $\theta = 180°$. In addition, this energy "spread" is an increasing function of the beam energy of the accelerator.

36

2.3 Experimental Results

2.3.1 D-D Reaction

Charged Fusion Product Detection

Our standard charged fusion product diagnostic uses silicon surface-barrier diodes (SBDs) inside vacuum, viewing the target at $\theta \simeq 120°$. SBDs have intrinsic detection efficiency of 1.0 and energy resolution of $\lesssim 50$ keV for most charged particles, which is sufficient to uniquely differentiate the charged products of the aforementioned fusion reactions.[2] Thus, SBDs provide an absolute calibration of the fusion rate, given the geometry of the experimental setup.

We typically use a partially-depleted SBD (typical thickness $\sim$300 μm) the front of which is covered with a 1.5-μm-mylar filter to protect it from the undesirable fluence of backscattered beam particles. The presence of the mylar filter, however, precludes the detection of 0.82-MeV D-D ^{3}He particles, because they lose most of their energy to the mylar, bringing their spectral peak to the low-energy noise level and thus making them indistinguishable. Another limitation of these partially-depleted SBDs is that they cannot measure the *full energy* of the 14.6 MeV D-^{3}He proton (its range is about 1300 μm in silicon [30]). In order to measure their full energy, a 2000-μm thick fully-depleted SBD is used.

Charged fusion product emissions at different angles of observation θ measured with respect to the beam direction have been studied. For instance, Fig. 2.5(a) shows spectra of D-D tritons and protons taken with an SBD in vacuum at $\theta \simeq 65°$ and $\theta \simeq 115°$. (For an angle of $\theta \leqslant 90°$, a slanted target has to be used.) The energy of both the proton and triton shifted downward as θ was increased.

---

[2]Note that the different charged fusion product species cannot be identified positively as the SBD is only sensitive to the energy deposited, regardless of whether the energy is from a proton or a ^{3}He particle, say. To "identify" the particle species, more information is needed. For instance, one can allow the energetic particles to pass through a thin foil in front of the SBD and study the partial energy loss and the energy straggling as a result. Different particle species with identical energy can also be identified with magnetic and electrostatic separation techniques.
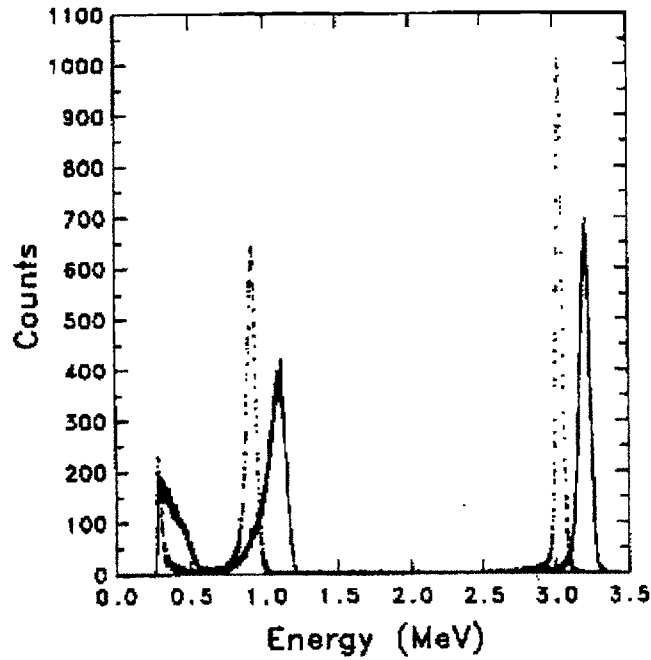
Figure 2.5: (a) D-D triton and proton spectra were collected with an SBD at $\theta \simeq 65°$ (solid spectrum) and $\theta \simeq 115°$ (dotted spectrum). The peaks in the vicinity of 1 MeV and 3 MeV indicate the presence of D-D tritons and protons, respectively. The difference between the two spectra is due to the kinematic effect. (b) D-D charged fusion product spectrum collected with the same SBD at $\theta \simeq 120°$. In this single run, both the protons and tritons show double peaks, indicating the presence of two components in the deuteron beam (D^+ with 150 keV and D_2^+ with 75 keV/deuteron, respectively).
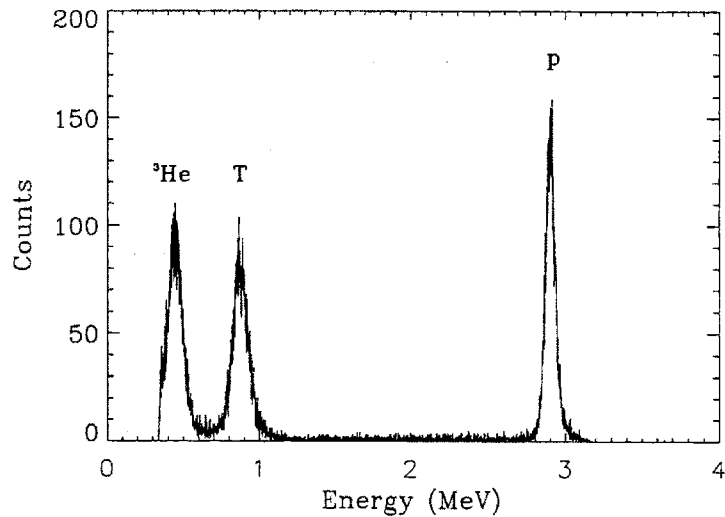
Figure 2.6: This D-D charged fusion product spectrum shows clearly the presence of the ^{3}He particle described in Eq. (1.2). The Cockcroft-Walton accelerator was run for almost 20 hours with a 26 keV deuteron beam at a beam current of around 12 μA. The SBD, with an aluminum front surface, was located at $\theta \simeq 120°$.

An example of the kinematic effect of the deuteron energy is seen in Fig. 2.5(b). In this single run, the accelerator voltage was constant at 150 kV and the detection angle was fixed at $\theta \simeq 120°$. Both the protons and tritons show double peaks, indicating the presence of two components in the deuteron beam (D^+ with 150 keV and D_2^+ with 75 keV/deuteron, respectively). By varying the detection angle θ and/or the accelerator voltage, these kinematic effects, as explained in the previous section, can be taken advantage of in providing a "tunable" source of monoenergetic particles for various purposes, *e.g.*, detector damage studies [31].

The D-D ^{3}He particle has actually been detected with an SBD in the accelerator vacuum with the mylar filter removed. Whereas the absence of the mylar reduces the energy loss of the ^{3}He particles before they hit the SBD, it also necessitates the lowering of the deuteron beam energy (*i.e.*, accelerator voltage) which in turn lowers the energy of the backscattered deuterons such that they do not affect the detection
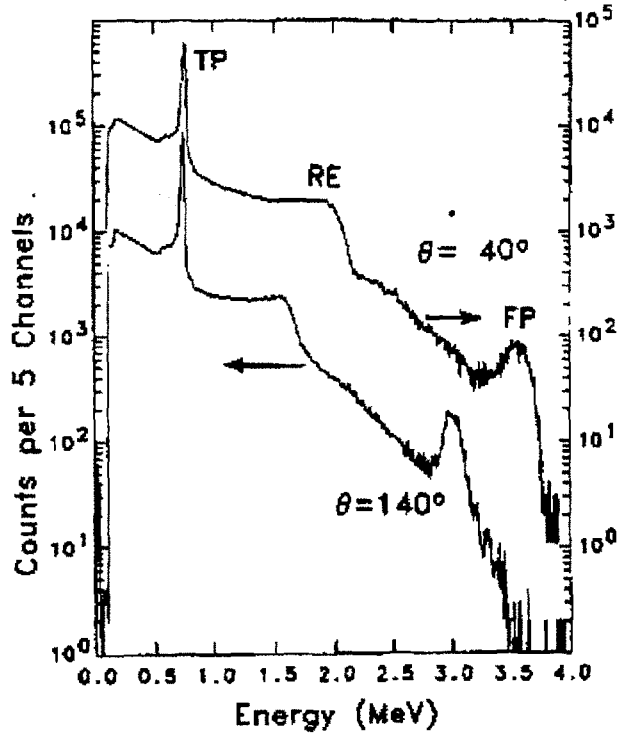
Figure 2.7: ^{3}He proportional-counter fast-neutron spectra were measured at $\theta \simeq 40°$ and $\theta \simeq 140°$. An energy calibration was obtained by using the thermal capture peak (at 765 keV) and the lowest edge due to the wall effect (at 191 keV). The "fast peak" (FP) and the recoil edge (RE) are at higher energies for forward angles (see Table 2.1).

of the ^{3}He particle. Fig. 2.6 shows the charged fusion product spectrum accumulated after running the Cockcroft-Walton accelerator with a 26 keV deuteron beam at a beam current of around 12 μA for almost 20 hours. The spectral energies of the peaks agree well with expected values when kinematic effect and the effect of ranging through the aluminum front surface of the SBD are accounted for.

Fusion Neutron Detection

The relative neutron flux is monitored with a ^{3}He or BF_3 thermal-neutron detector inside a moderating cylinder located a fixed distance from the target. Around the tar-

get chamber the time-integrated fast- and thermal-neutron doses are also monitored with neutron dosimeters. These detectors provide a quantitative comparison of the total number of neutrons produced during different experiments. This is important for radiation damage experiments, where the total dose on a sample is the important parameter.

θ	Measured Full Energy	Predicted Full Energy	Measured Recoil Edge	Predicted Recoil Edge
40°	3.57	3.60	1.92	2.13
90°	3.23	3.25	1.69	1.87
140°	3.01	2.95	1.58	1.64

Table 2.1: D-D neutron energies in MeV, measured (with a ^{3}He proportional counter; all in MeV) *vs.* calculated (on the basis of beam/target kinematics and neutron scattering by ^{3}He nuclei). The measured energies agree to about 10% with the predicted values.

We have used both ^{3}He and ^{4}He proportional counters to measure fast neutron spectra. Fig. 2.7 shows ^{3}He proportional-counter fast-neutron spectra taken at $\theta \simeq 40°$ and $\theta \simeq 140°$. For incident neutrons with energy E_n, each spectrum consists of three primary features [32]: (1) the thermal peak (TP at the capture reaction Q-value, 765 keV) and the corresponding wall-effect contributions; (2) the ^{3}He recoil edge at 75% of E_n (RE); and (3) the fast neutron capture peak (FP at Q + E_n). Table 2.1 compares the measured fast neutron energies with the values calculated based on kinematics for $\theta = 40°, 90°$, and 140°. The measured and calculated neutron energies agreed to about 10%. Some of the difference can be attributed to neutron scattering in the the experimental facility in general, *e.g.*, vacuum structure of the accelerator, the floor and ceiling of the laboratory, causing an overall lowering of the measured neutron energies.
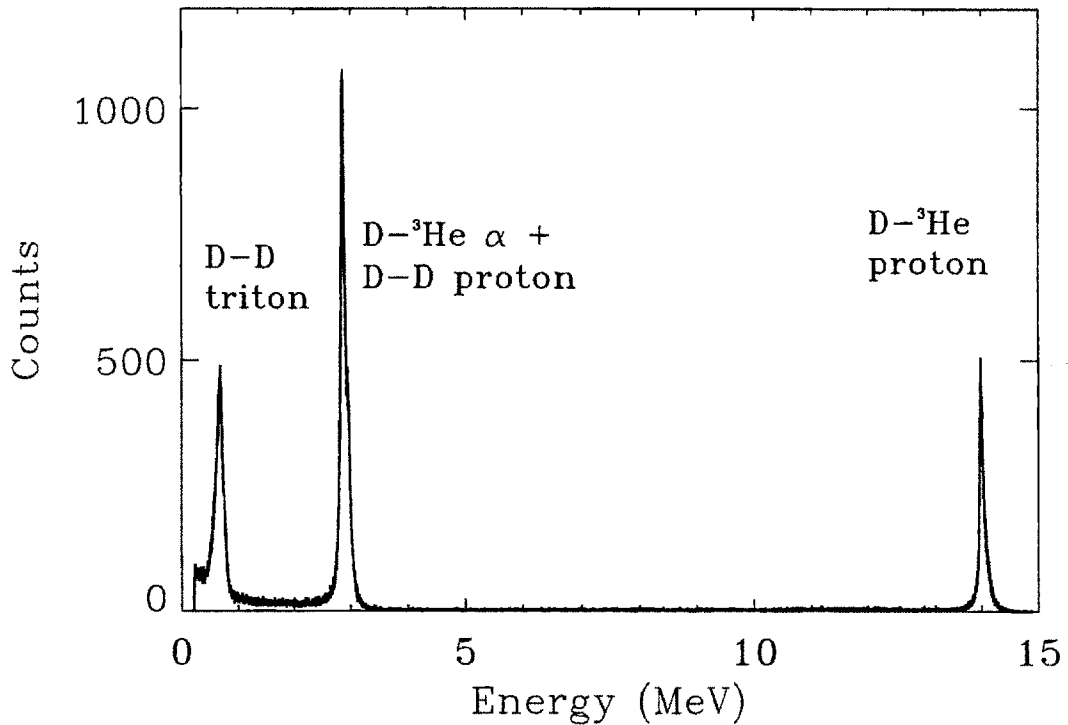
Figure 2.8: Spectrum of D-^{3}He fusion products. D-D fusion was also taking place because of the presence of small amounts of deuterium in the ^{3}He ion beam.

2.3.2 D-^{3}He Reaction

By switching the Cockcroft-Walton accelerator gas supply to ^{3}He, a ^{3}He ion beam bombarding a deuterated erbium target gives rise to D-^{3}He reactions. The resulting charged fusion product spectrum is shown in Fig. 2.8 contrasted with that from D-D reactions. The spectra were taken with an SBD in vacuum at $\theta \simeq 120°$. A D-^{3}He proton peak is clearly seen at 14.2 MeV, as expected given allowance for the kinematic effect and energy loss through the SBD's thin mylar window. However, because of the presence of small amounts of deuterium in the ion source bottle and the relatively higher cross section of the D-D reaction compared with the D-^{3}He reaction, D-D protons and tritons were still being produced. As a result, the spectral peak of D-
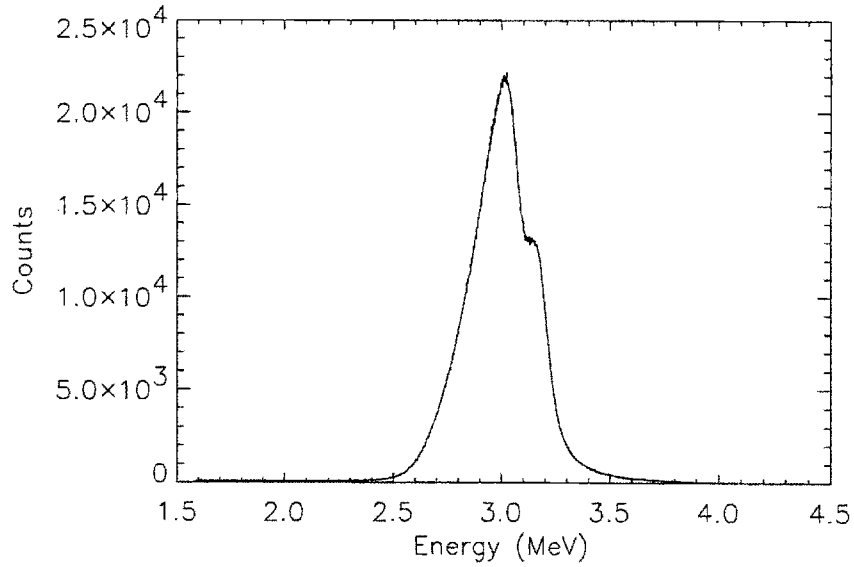
Figure 2.9: D-T α particle spectrum from an SBD placed at $\theta = 120°$ from the deuteron beam direction. Two distinct peaks, one at 3.10 and the other at 3.22 MeV, indicate the presence of two components in the deuteron beam (D^+ with 150 keV and D_2^+ with 75 keV/deuteron, respectively).

^{3}He α particles turned out to be too close to the spectral peak of the D-D protons to be resolved. (Taking into account the kinematic effect and the mylar window, $E_{proton} \sim 2.81$ MeV and $E_\alpha \sim 2.91$ MeV.) The number of counts under the combined peaks of D-D protons and D-^{3}He α particles is also consistent with this assertion.

2.3.3 D-T Reaction

Because of the radioactive nature of a tritiated erbium target, all D-T runs on the Cockcroft-Walton accelerator were performed using a dedicated target chamber. With a deuteron beam at 150 keV and beam current of 1.2 μA measured at the target, the reaction rate was measured to be $4.77 \pm 0.24 \times 10^7$ reactions per second [24]. This was deduced through the counting of α particles using an SBD placed at $\theta = 120°$ (see Fig. 2.9). The superposition of two distinct peaks, one at 3.05 MeV and the other at 3.21 MeV, in the α spectrum indicates again the presence of two components in the
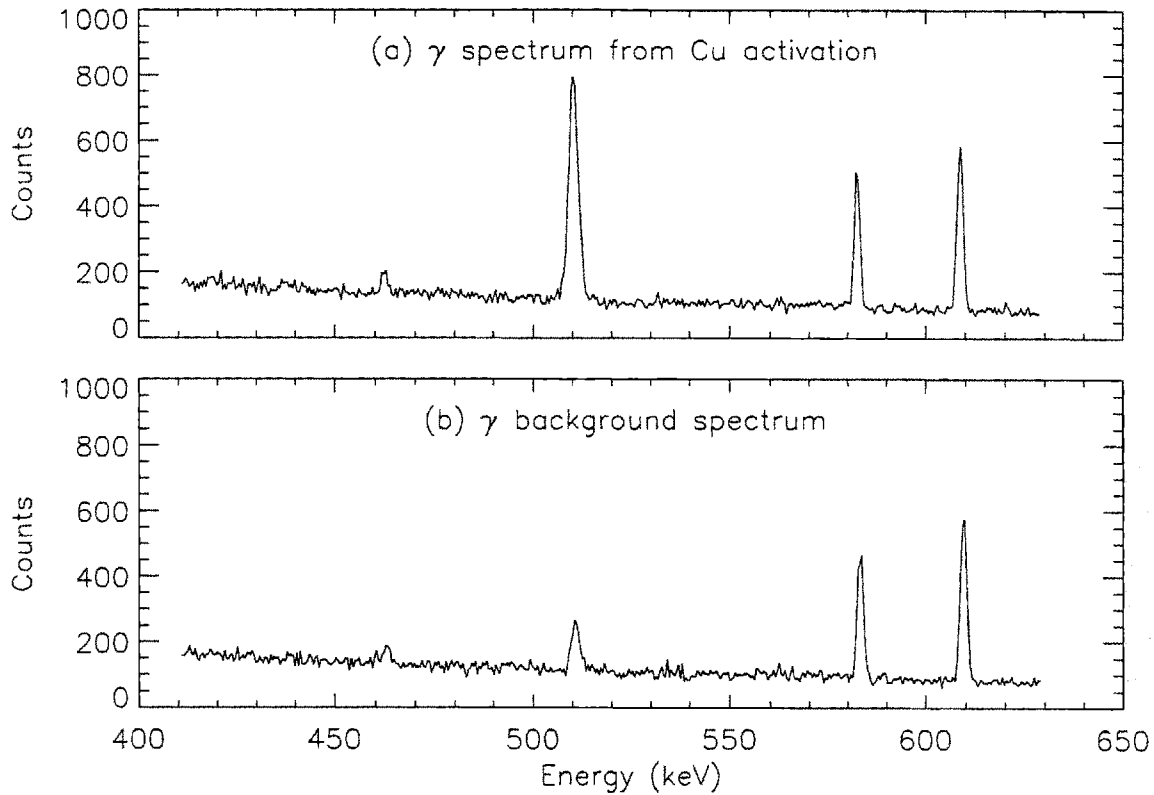
Figure 2.10: γ ray spectrum around 0.511 MeV of copper (a) after, and (b) before (*i.e.*, background) activation by D-T neutrons. The spectra were taken with a high purity germanium detector. The enhanced line at 0.511 MeV results from positron-electron annihilation as β^+ are emitted when ^{62}Cu decays to ^{62}Ni.

deuteron beam (D^+ with 150 keV and D_2^+ with 75 keV/deuteron, respectively). This compares well with the expected 3.10 MeV and 3.23 MeV.

Different diagnostic techniques were used [24] for the detection of the 14.1 MeV neutrons: copper activation, SBDs, and a ^{3}He proportional counter. Here, the results for one of these, copper activation, is included to illustrate the detection of the high energy neutrons. The technique is based on the reaction ^{63}Cu(n,2n)^{62}Cu which has a 10.9 MeV threshold, a cross section of 480 mb [33]. A natural copper foil was placed 4.8 cm from the $ErT_{1.92}$ target where neutrons were generated from deuteron bombardment. ^{62}Cu decays to ^{62}Ni (half-life of 9.73 min) by β^+ emission and about

39% of the positrons are annihilated in the foil generating characteristic 0.511 MeV γ rays. A high purity germanium detector, previously calibrated in efficiency with a ^{226}Ra source, was used to collect the γ spectrum in Fig. 2.10(a) from the copper foil. The background γ spectrum in Fig. 2.10(b) is included for comparison. As the γ spectrum was collected 155 s after the 3000-s irradiation of the copper foil, the interference of ^{65}Cu(n,2n)^{66}Cu (half-life of 12.7 h) is estimated to be 2.6%. The measured reaction rate of $4.71 \pm 0.73 \times 10^7$ per second compares well with that measured with the SBD from α counting.

2.3.4 Other Reactions

The accelerator generates γ rays via low-probability branches of fusion reactions, *e.g.*,

$$D + {}^3He \longrightarrow \gamma + {}^5Li, \qquad \mathrm{E}_\gamma = 16.38 \text{ MeV}; \tag{2.8}$$

$$p + {}^{11}B \longrightarrow \gamma + {}^{12}C, \qquad \mathrm{E}_\gamma = 15.96 \text{ MeV}; \tag{2.9}$$

$$p + {}^7Li \longrightarrow \gamma + {}^8Be, \qquad \mathrm{E}_\gamma = 17.25 \text{ MeV}. \tag{2.10}$$
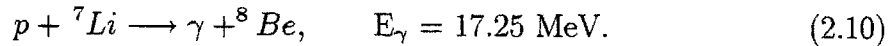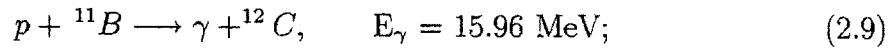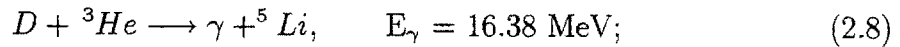
These reactions are used as well-calibrated high-energy γ-ray sources for characterizing γ-ray diagnostics [25], such as NaI(Tl) scintillators or a High-Purity Germanium high-resolution spectrometer. As an illustration, Fig. 2.11 shows the γ-ray spectrum taken with a NaI(Tl) scintillator from the ^{7}Li(p,γ)^{8}Be reaction.

X rays can be generated in the Cockcroft-Walton accelerator via two mechanisms. Particle-induced x-ray emissions (PIXE) [26], typically with energy <20 keV, result when a solid target is bombarded by an ion beam. The x rays are characteristic line radiation from the target material. We measure PIXE x-ray spectra with a Si(Li) detector for x rays with energy $\gtrsim 1$ keV, and thin-window gas-flow proportional
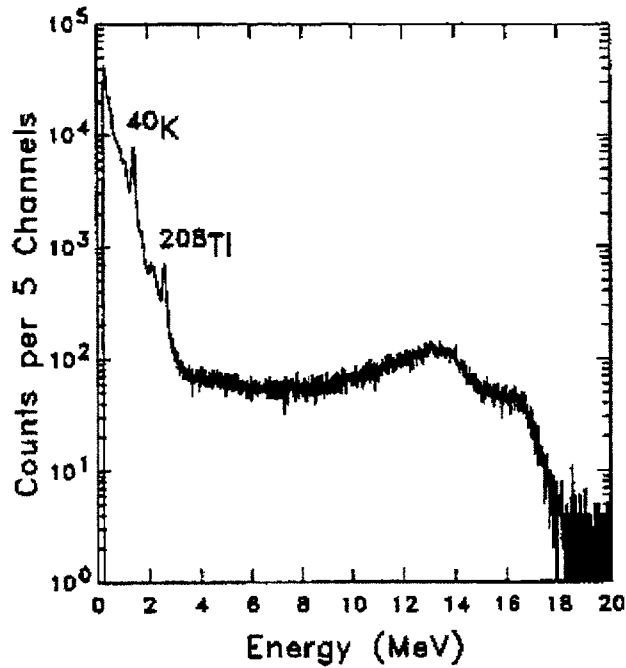
Figure 2.11: The γ rays (at 17.3 and 14 MeV) from the ^{7}Li(p,γ)^{8}Be reaction were measured with a 3" × 3" NaI(Tl) scintillator. A natural lithium target was used, but the 5.6-MeV ^{6}Li(p,γ)^{7}Be γ rays were not observed in the NaI(Tl) data because of the small γ-ray branching ratio. (The background lines of ^{40}K and ^{208}Tl are also present at 1.46 MeV and 2.61 MeV respectively.)

counters for x rays with energy $\lesssim 1.5$ keV [26]. Secondly, a very much smaller but undesired x-ray flux is generated near the ion source when secondary electrons are accelerated back up to the high voltage section of the accelerator, generating high-energy bremsstrahlung in the process.

46

Chapter 3

Experimental Studies of Charged-Particle Sensitive Depth in Silicon Detectors

As part of an on-going effort to develop diagnostics for energetic charged particles from laboratory and space experiments, we examined the possibility that particle identification could be expedited by varying the applied bias voltage on silicon-based charged particle detectors, specifically, silicon surface barrier detectors (SBDs). When the applied bias voltage changes, the thickness of the depletion layer, commonly acknowledged to be the active layer for charged particle detection, changes in a predictable fashion. For a given change in the bias voltage, the resulting change in the energy spectrum should be idiosyncratic of the charged particle species, given the knowledge of the species' stopping power and range in silicon.

This chapter begins with a discussion of charged particle interaction with matter. This leads directly into the application of silicon-based diodes for charged particle detection. Using MeV protons and tritons, we performed spectroscopy experiments whereby we observed changes in the energy spectrum as a function of the bias voltage [34]. These particles were generated via the Cockcroft-Walton linear accelerator

discussed in Chapter 2 as fusion products. The results indicate that, contrary to commonly held belief, the detector sensitive depth is not generally the depletion region thickness. Indeed for partially depleted SBDs, the performance is not greatly degraded even for zero bias.

3.1 Charged Particle Interaction with Matter

A charged particle interacts with matter primarily through Coulomb forces between its charge and the negative charges of the orbital electrons of the absorber atoms. This is commonly referred to as electron stopping. However, in the latter part of the particle's trajectory, nuclear stopping, *i.e.*, energy loss to the absorber's nuclei, dominates. Electrons along the track of the charged particle may receive sufficient energy from the charged particle's close encounter to be either excited (raised to a higher lying shell) or ionized. The latter case leaves behind a vacancy, or a hole, in the lattice of the absorber medium.

The energy loss per unit length, or the stopping power, is described by the *Bethe formula*

$$ -\frac{dE}{dx} = \frac{4\pi\, z^2\, e^4}{m_o\, v^2}\, NZ \left[\ln\frac{2\, m_o\, v^2}{I} - \ln(1-\beta^2) - \beta^2 - \sum_i \left(\frac{C_i}{Z}\right) - \delta \right], \quad (3.1) $$

where e is the electronic charge, m_o is the electron rest mass, ze and v are the incident particle's charge and velocity, N and Z are the absorber's number density and atomic number, I is the mean ionization potential of the absorber atoms, and β is v/c. For a 3 MeV proton, $\beta = 0.08$, and the correction due to relativistic effects is small. The second to last term in the square bracket is a shell correction term which comes about because electrons in different shells of the absorber atoms contribute differently to the stopping power. The ith term represents the correction for the ith atomic shell. Finally, δ is a density correction to account for the absorber atoms not being free, but it is negligible for incident particle energies less than several hundred MeV. Thus, for

48

nonrelativistic charged particles, only the first term within the square bracket of Eq. (3.1) is significant.

The Bethe formula begins to fail at low particle velocities when nuclear stopping dominates because (1) charge exchange between the particle and absorber atoms will alter z,[1] (2) corrections for nonparticipating electrons in the inner shells affect I, and (3) the logarithmic term passing through zero to negative values when $2\,m_o\,v^2 = I$, which is equivalent to the particle having energy $E_p = m_p\,v^2/2 = (m_p/4\,m_o)I$, or about 0.1 MeV for protons in silicon. Therefore, to accurately calculate the range, one cannot just integrate the inverse of Eq. (3.1) from a particle's initial energy to zero. Instead, the stopping power and range of any particle in a specific absorber quoted in this thesis are calculated using the TRIM code, based on stopping cross sections both calculated and compiled from experiments [35].

Whereas electronic stopping (collisions with electrons) determines energy loss, nuclear stopping (collisions with the nuclei) is predominantly responsible for pitch angle scattering. The mean square of the average angle of deflection Θ among a large number of the same charged particles through an absorber thickness t is [36]

$$\langle\Theta^2\rangle \simeq 4\pi N \left(\frac{zZe^2}{E}\right)^2 \ln\left(204\,Z^{-\frac{1}{3}}\right) t. \tag{3.2}$$

If one substitutes a characteristic stopping length of $E(-dE/dx)^{-1}$ (taking the non-relativistic case) for t in Eq. (3.2), the mean square angle for MeV particles evaluates to

$$
\begin{aligned}
\langle\Theta^2\rangle &\simeq 4\pi N \left(\frac{zZe^2}{E}\right)^2 \ln\left(204\,Z^{-\frac{1}{3}}\right) \Big/ \left(\frac{4\pi\,N\,Z\,z^2\,e^4}{E^2}\,\frac{m_p}{2\,m_o}\,\ln\frac{2\,m_o\,v^2}{I}\right) \\
&= \frac{2\,Z\,m_o}{m_p}\left[\frac{\ln\left(204\,Z^{-\frac{1}{3}}\right)}{\ln\frac{2\,m_o\,v^2}{I}}\right] \ll 1. \tag{3.3}
\end{aligned}
$$

---

[1]The extreme case is when the particle is near the end of its track. It would have gained z electron(s) and become a neutral atom.

Thus, the path taken by a charged particle in its slowing down process tends to be quite straight. The mean range, or range, of a charged particle in a specific absorber medium is a fairly unique quantity.

Particle	Source	Energy (MeV)	Range (μm)
^{1}H	D-D	3.0	91
	D-^{3}He	14.7	1300
^{3}H	D-D	1.0	9.8
^{3}He	D-D	0.82	2.7
^{4}He		3.0	11.6
	D-^{3}He	3.6	14.8

Table 3.1: A list of energetic charged particles from different sources, their initial energies, and their ranges in silicon [35].

Different charged particles have different ranges in a given material. Table 3.1 lists an array of charged particles and their ranges in silicon [35]. The short range of these particles in solids — for instance, a 3 MeV proton stops in 91 μm of silicon, or 35 μm of stainless steel — means that the size of the detector can be very compact, though most practically, it has to be housed in vacuum lest the particles lose most or all their energy traversing other materials.

3.2   Semiconductors as Charged Particle Detectors

Silicon surface barrier detectors (SBDs) have been widely used for the detection of charged particles [12, 13, 37], neutral particles [38], and x rays [39–42]. They belong to the family of detectors commonly known as semiconductor diode detectors. They are characterized by their relatively high energy resolution, fast timing properties, and compact size as charged particle detectors [43].

The overall significant effect when a charged particle passes through a slab of semiconductor like silicon is the production of many electron-hole pairs along its track. On average, every 3.6 eV deposited in silicon by any light charged particle at room temperature results in the generation of an electron-hole pair, which serves as

a charge carrier.[2] The smallness of this number (compared to, say, typically 30 eV required to create an ion pair in typical gas-filled detectors) results in the dominant advantage of semiconductors as detection media for charged particles. The statistical fluctuation in the number of charge carriers per incident particle becomes a smaller fraction of the total as the number of charge carriers is increased. This is usually the main factor determining the limiting energy resolution of a detector.

In addition, the "ionization energy" of 3.6 eV per electron-hole pair has two other implications. First, the response of the detector exhibits a simple linearity between the energy of the incident charged particle and the number of the charge carriers generated per particle. This is a desirable feature for any spectroscopic detection system. Secondly, the silicon detector is intrinsically unable to distinguish between different particle species when they have the same energy. It is sensitive only to the deposited energy.

The operation of silicon detectors is based on the favorable properties of the junction created between the n- and p-type regions. (In an SBD, instead of having both n- and p-type silicon, one is replaced by an equivalent metal layer, and the junction is formed where the metal meets the silicon. If the SBD bulk silicon is p-type, a junction is formed by depositing a layer of aluminum; if the bulk is n-type, a gold layer is used.) At the junction (see Fig. 3.1), the majority carriers of each side (holes in the p-type, electrons in the n-type) diffuse across the junction continuously, the effect of which is that a net negative space charge on the p side and a net positive space charge on the n side of the junction are established. This creates an electric potential, called the contact potential, across the junction with an electric field E_d pointing toward the p side. This retards further diffusion of majority carriers across the junction and leads to an equilibrium. The contact potential is usually about 0.5 V for silicon junctions. This region with the steady-state charge imbalance is called the depletion region.

---

[2]However, for heavy ions like fission fragments, the "ionization energy" required does become larger [43].
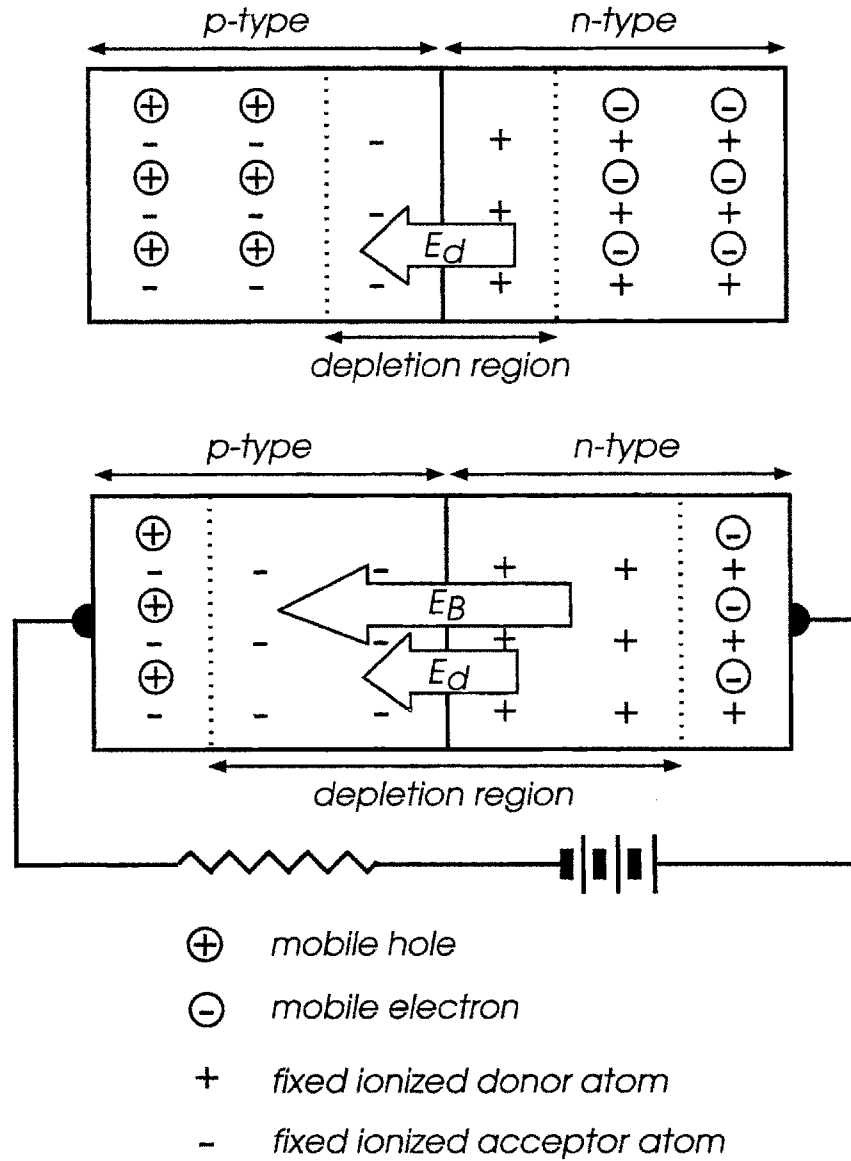
Figure 3.1: Unbiased and reverse biased p-n junctions. Shown in the sketches are also the electric field E_d due to the contact potential, and the the electric field E_B arising from the applied reverse bias voltage. Note that only majority carriers are shown.

In the depletion region, any electron created is swept toward the n-type side by the electric field; similarly, any hole is swept toward the p-type side. The region is "depleted" in the sense that the concentration of mobile holes and electrons is greatly diminished. The charges set up in the depletion region are due to the immobile ionized donor sites on the p side and the depleted acceptor sites on the n side. As these charges do not contribute to conductivity, the depletion region exhibits a very high resistivity compared to the n- or p-type regions on either side. Silicon detectors are constructed such that the depletion region is as close to the front side as possible. In SBDs, for instance, the aluminum front layer is typically only about 1500 Å thick.

Still, to ensure that all the electron-hole pairs formed along the track of an incident charged particle can be swept by the electric field, the depletion region has to be thick enough to fully enclose the entire particle track. After all, it is the total charge due to the number of electron-hole pairs created that carries the information about the incident particle's energy. To significantly increase the depletion region thickness, a reverse bias voltage, which has the same polarity as the contact potential, is applied to the junction. Virtually all the applied bias falls across the depletion region because of its high resistivity. It is generally believed that the depletion region thickness d is proportional to the square root of the voltage V (the sum of the contact potential and applied bias) across the junction (*e.g.*, Ref. [43]):

$$d \cong \sqrt{2\,\epsilon\,V\,\mu\,\rho_d}\,, \tag{3.4}$$

where ϵ is the dielectric constant of the silicon, μ is the mobility of the majority carrier, and ρ_d is the resistivity of the doped silicon. Furthermore, it is widely accepted that the sensitive depth of a silicon diode detector like the SBD is the depletion region thickness [43]. If one can externally control the sensitive depth, that is, the depletion region thickness, one potentially can differentiate between particles of different species even when they have the same energy because each particle species has a different stopping power in silicon. This is the motivation for the work discussed in this chapter.

If a charged particle's range is greater than the sensitive depth of the SBD, the SBD would not be expected to detect the full energy of the particle, since some of this energy is dissipated in a part of the SBD that is beyond the sensitive depth. Consider the detection of 3 MeV protons and 3 MeV α particles with an SBD whose bias voltage is set such that the depletion region thickness is, say, 50 μm, which is between the ranges of these two particle species. (See Table 3.1.) They can now be differentiated because not all of the electron-hole pairs created by each proton can contribute to the signal pulse. In the energy spectrum, the proton will show a peak at an energy less than 3 MeV. The thinner the depletion region, the bigger the downshift of the proton peak in the energy spectrum. With the knowledge of the stopping power of any particle in silicon, one is able to calculate the energy shift at any bias voltage. And in principle, given the shifted energy spectrum, the reverse can be carried out to uniquely identify an unknown particle.

Using different charged particles, we performed spectroscopy experiments whereby we observed the energy shift and the spectral shape change as a function of the bias voltage. We found, however, that the depletion region thickness is not generally the charged-particle sensitive depth, a conclusion also reached for x rays [41].

3.3 Apparatus and Source of Charged Particles

Numerous SBDs, all manufactured by EG&G Ortec, were used in this study. (See Table 3.2.) SBD #30-020A, which is n-type, is fully-depleted with maximum bias. All the other SBDs, henceforth to be referred to collectively as the Group, are "ruggedized" p-type and partially-depleted when maximum bias is applied. The electronics included an ORTEC 142 preamplifier, an ORTEC 590 amplifier, and a PC-based pulse-height analysis system.

We report here on studies done with 3 MeV protons and 1 MeV tritons produced via beam-target D-D fusion using the Cockcroft-Walton accelerator (see Chapter 2). The SBD viewed a deuterated-erbium target at 120° relative to the incident direction

I.D. #	Max. Bias (V)	Depl. Region Thickness (μm)	Silicon Thickness (μm)	Resistivity (Ω-cm)
26-454B	-100	$\approx$100	530	15700
16-662D	-75	$\approx$100	335	3000
18-312C	-100	$\approx$100	484	3000
17-380F	-150	$\approx$100	461	4400
18-365E	-100	$\approx$100	292	3500
16-848A	-75	$\approx$100	328	3000
16-821D	-75	$\approx$100	544	3500
17-381G	-100	$\approx$100	321	4000
18-748A	-100	$\approx$100	334	4400
30-020A	+355	2000	2000	75000

Table 3.2: The SBDs used in this study are listed with maximum applied bias voltage, the corresponding depletion region thickness at that bias, the nominal physical thickness of the silicon, and the resistivity of each SBD. Note that SBD #30-020A is fully-depleted at +355 V.

of the 150 keV deuteron beam. A 1.5 μm mylar filter placed in front of the SBD was used to stop back-scattered deuteron beam ions from reaching the SBD. Consequently, the D-D protons and tritons suffered small energy losses ($\approx$30 keV and $\approx$120 keV respectively), while the 0.8-MeV D-D ^{3}He particles were ranged out.

3.4 Results and Discussion

Figure 3.2 shows a series of spectra of D-D protons and tritons obtained with SBD #16-662D as the applied bias was varied from -75 V (providing $\approx$100 μm of depletion region) to 0 V. The fusion products incident on the SBD do not have their full energies because of kinematic effects and ranging through mylar. This agrees well with our prediction. The double peaks due to D^+ and D_2^+ species in the accelerator beam are observable in Fig. 3.2(a) for the tritons. In general, the response exhibited in Fig. 3.2 is representative of the SBDs in the Group. There is always a gradual energy downshift and a degradation of the resolution as the bias is lowered. At zero bias, the
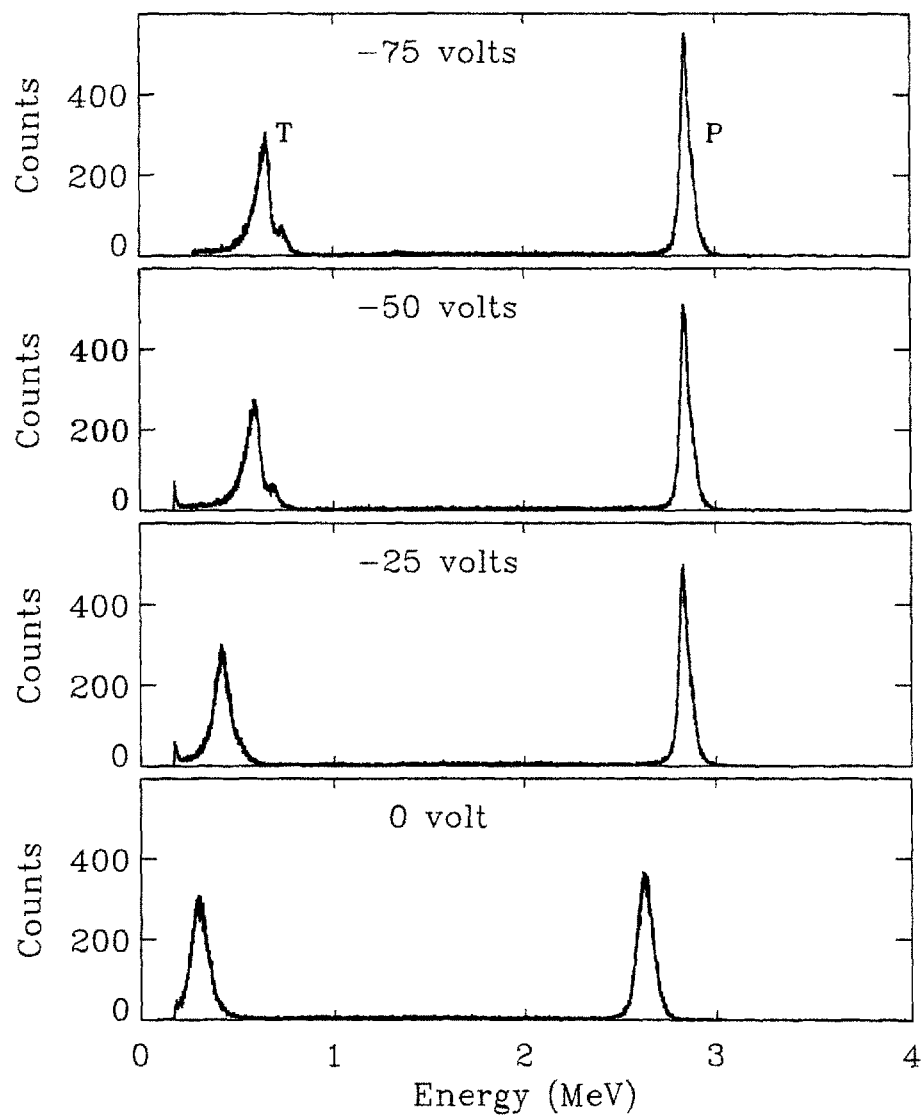
Figure 3.2: A series of spectra of D-D protons (P) and tritons (T) collected with SBD No. 16-662D at different applied bias. The presence of double peaks, due to D^+ and D_2^+ species in the accelerated beam, is especially noticeable in the triton peak. It is surprising that the spectrum stays intact even at zero applied bias.

energy downshift for the various SBDs in the Group ranges from <5% to ~50%; and the change in energy resolution, as measured by the change in spectral width, varies from practically none to >300% increase. A striking feature is that the spectrum nonetheless remains intact even at 0 V bias. From the practical point of view, this could be important since it indicates that counting experiments are possible without applied bias, though spectroscopy may be precluded or at least made difficult.
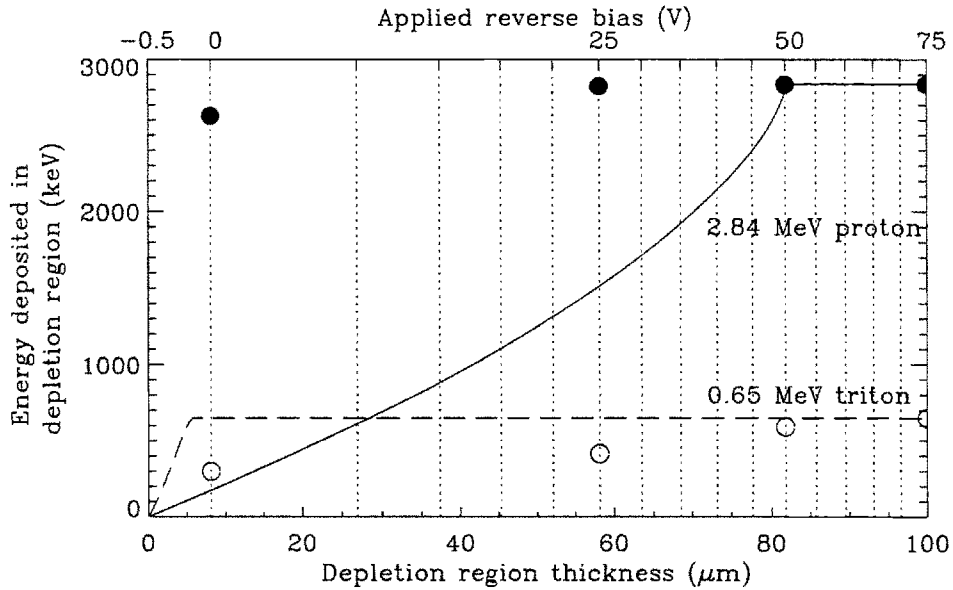
Figure 3.3: A comparison of the observed and expected (from model) energy deposition in SBD No. 16-662D as a function of the applied bias voltage.

Based on the accepted model for the depletion depth given in Eq. (3.4), this result is unexpected. Figure 3.3 shows a comparison of what is observed with what the accepted model predicts for SBD No. 16-662D. The solid curve is the predicted energy deposited by a 2.84 MeV proton in the depletion region (according to the model, the active region) of the SBD as a function of the depletion region thickness. The energy deposition calculation is made using the TRIM code [44]. The top and bottom x axes are interchangeable, showing through Eq. (3.4) the relationship between the applied

bias voltage and the depletion region thickness. A contact potential of 0.5 V has been assumed. Plotted also are the observed energies as a function of the applied bias voltage for the protons (solid circles) and the tritons (hollow circles).

So, for instance, at an applied bias voltage of 25 V, the depletion region is expected to be about 58 μm deep, which is far short of the 2.84 MeV proton's range of 82 μm. A 2.84 MeV proton is expected to lose about 1500 keV while traversing this thickness of depleted silicon; the energy remaining will be lost in the inactive region beyond the depletion region. Therefore, one expects that SBD No. 16-662D would register a peak at about 1.5 MeV while biased at 25 V when detecting 2.84 MeV protons. However, the SBD in the experiment detected protons at 2.82 MeV.

Analogously, the long-dashed curve indicates the energy expected to be deposited by a 0.65 MeV triton as a function of the depletion region thickness. The model predicts that even at 0 V applied bias, a 0.65 MeV triton should deposit all its energy in the depletion region. This is because the 0.65 MeV triton has a short range of 5.8 μm. In other words, the triton peak should be the same in all cases. However, in the experiment, the triton peak downshifted with a lowering bias voltage. At 0 V bias, less than half of the 0.65 MeV of the triton was recorded.

Fig. 3.4 shows the response of SBD #30-020A to D-D protons and tritons as the applied bias was varied from +355 V (providing a depletion region of 2000 μm) to +50 V. The spectrum immediately begins to degrade and downshift in energy when the applied bias is not close to maximum. At 0 V, the spectrum has totally disappeared.

Figure 3.5 shows the expected energy deposited, according to the model, as a function of the depletion region thickness for SBD 30-020A. The predicted picture is clear: the spectrum is not expected to change with the bias voltage, except for the 2.84 MeV protons when the bias is 0 V. At virtually all bias voltages, the depletion region is thick enough for the energy of both particles to be deposited within it. Thus, no electron-hole charge pair should be lost to the inactive region behind the depletion region. The observation, once again, proves that the accepted model fails. Another

58
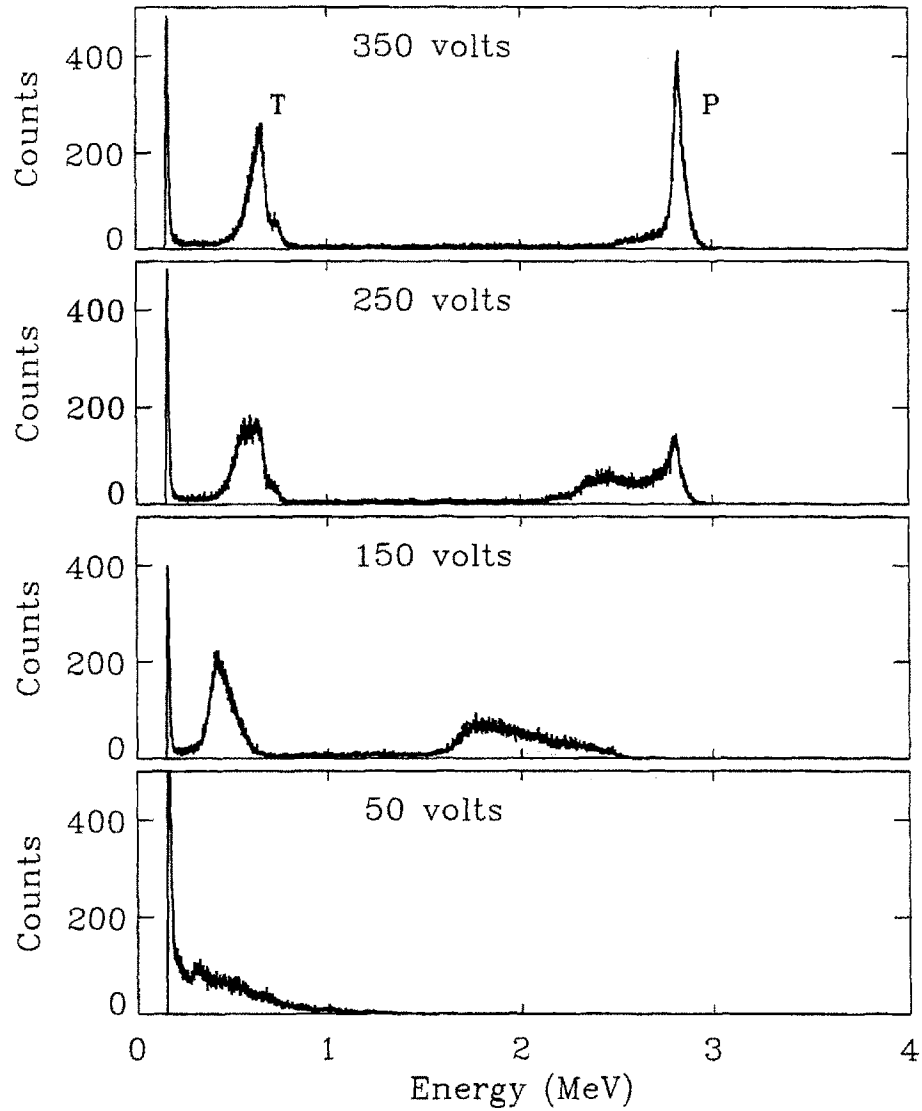
Figure 3.4: A series of spectra of D-D protons (P) and tritons (T) collected with SBD No. 30-020A at different applied bias. At 0 volt, the spectrum is essentially empty. The changes of the spectrum with decreasing applied bias cannot be explained quantitatively (based on the accepted model that an SBD's sensitive depth is the thickness of the depletion region).
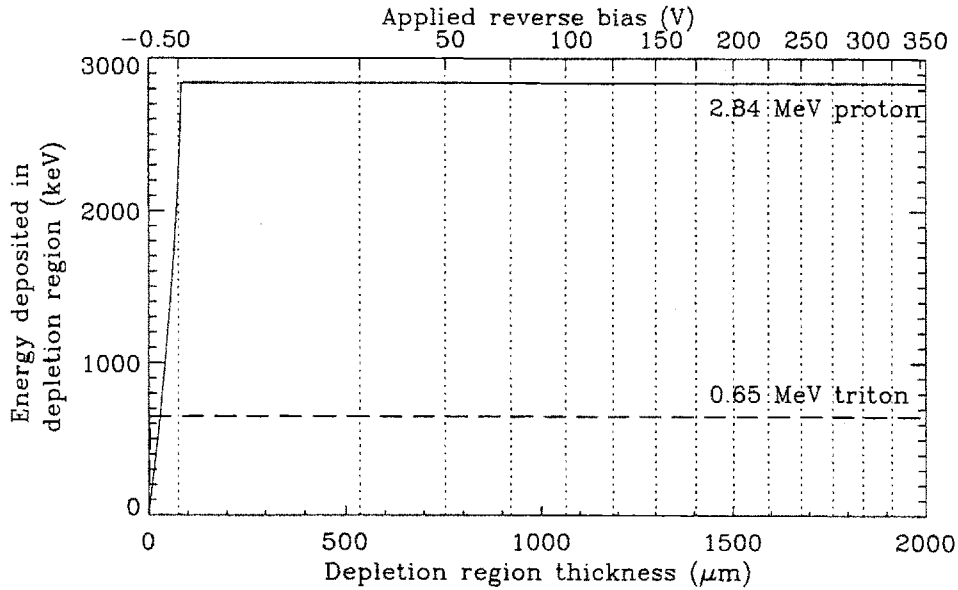
Figure 3.5: Expected energy deposition in SBD No. 30-020A as a function of the applied bias voltage.

interesting observation is that the response of this SBD and of the SBDs in the Group are markedly different; we do not understand this difference at this time.

Thus, we arrive at the conclusion that the charged-particle sensitive depth of SBDs is not generally the depletion region thickness. *It is important to emphasize that this result is contrary to what is commonly believed.* Also, this result is completely analogous to the conclusion reached about the x-ray sensitive depth [41]. In order to clarify these charged-particle results, it would be useful to perform comprehensive studies using various SBDs with different characteristics, such as thickness, doping type (p or n), resistivity, and so on. For the CFP spectrometer, the detectors will be operated at full bias to avoid any complication to the energy spectrum that may arise.

Chapter 4

The Charged Fusion Product Spectrometer

The ultimate goal of deploying the charged fusion product (CFP) spectrometer was to evaluate the effectiveness of ^{3}He minority heating through the broadened spectrum of unconfined 14.7 MeV protons from D-^{3}He reactions. Even though this objective was not accomplished in this thesis, studies of fusion rate scaling (Chapter 6) and ion temperature measurements (Chapter 7) were made. In the present chapter, the design of the spectrometer is presented at length.

4.1 Mechanical Design

Because of the complicated trajectories that CFPs follow and their short range in matter (see §3.2), their detection and, more importantly, the measurement of their energy spectrum require the positioning of the spectrometer inside the vacuum vessel. The experimental arrangement used in Alcator C-Mod is illustrated in Fig. 4.1. Points of interest include a bakeable ion-implanted-silicon detector, multiple apertures of choice, and in-vessel calibration by radioactive sources.

   The spectrometer's body is a cylindrical probe (5.72 cm o.d.) which is located
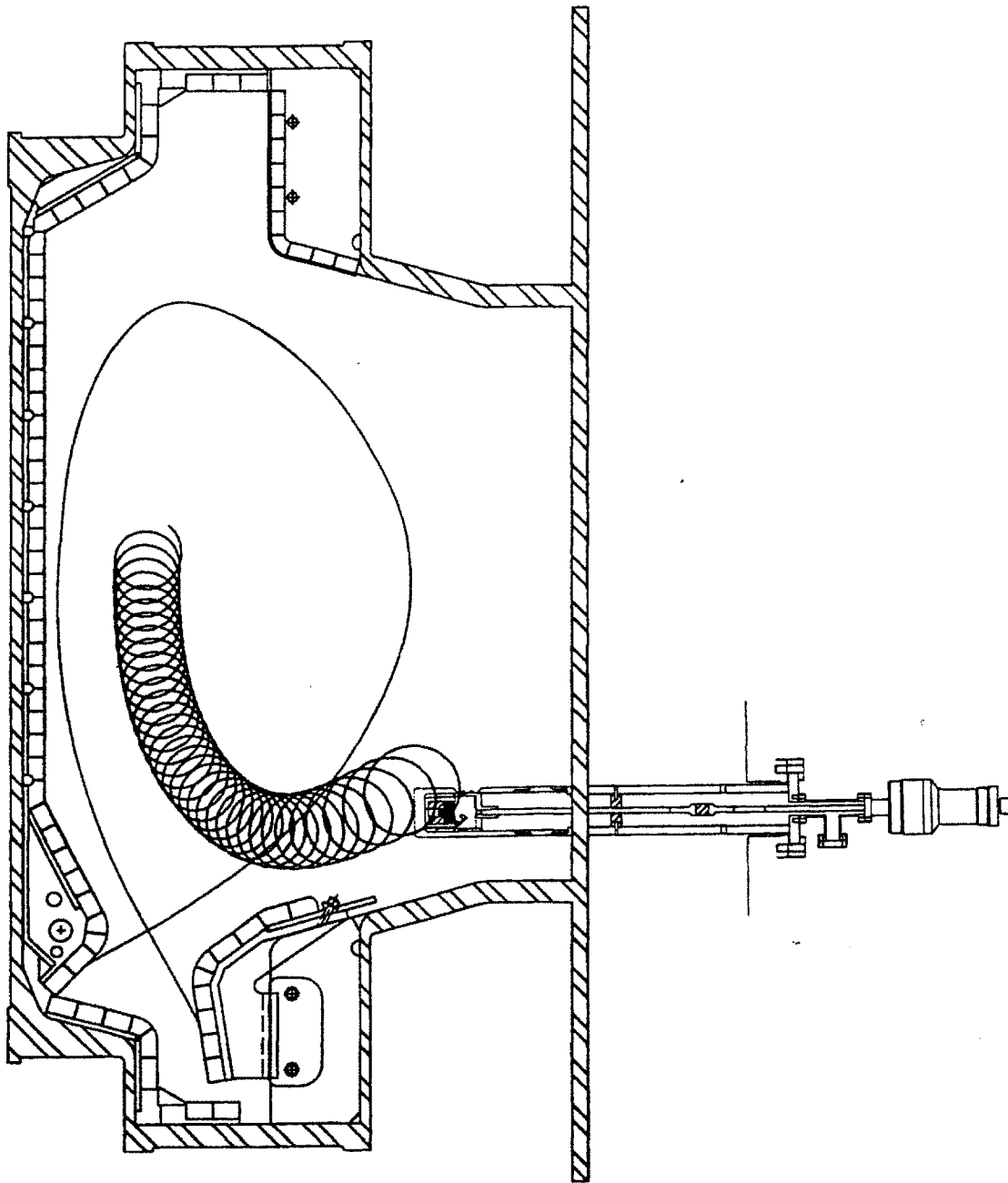
Figure 4.1: Poloidal view of the charged fusion product spectrometer on Alcator C-Mod. The cylindrical structure is located 25.8 cm below the midplane and its front end is at $R = 87.6$ cm.
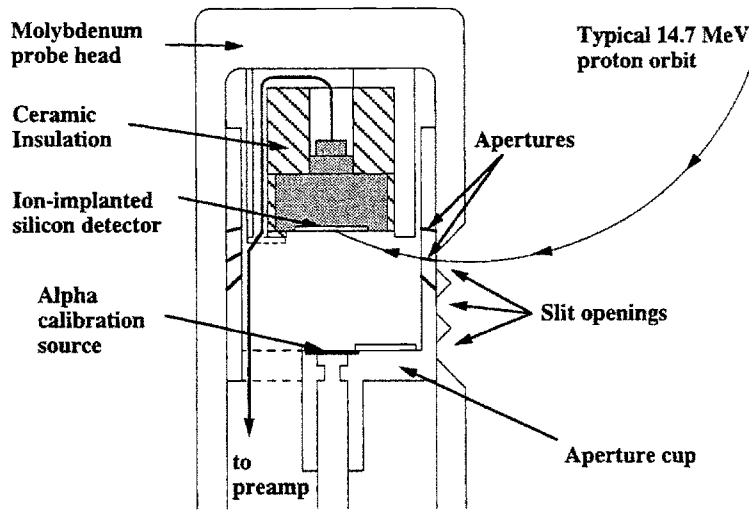
Figure 4.2: Sectional view of the spectrometer head assembly.

25.8 cm below the midplane at K port. The front end of the spectrometer probe is at $R = 87.6$ cm. The radial position of the spectrometer was chosen based upon two main concerns. First, this position is within a range of positions where the signal level expected would be adequate considering the fusion rate expected on Alcator C-Mod. Calculations of the expected signal level were made with the detection efficiency code described in Chapter 5. Secondly, the chosen radial location puts the CFP spectrometer safely in the shadow of three RF limiters which are toroidally 90°, 114°, and -54° away. This ensures that the probe does not encounter too much energy deposition through an excessive particle flux from the plasma, which it is not designed to withstand. While the probe support is principally made of 0.95 cm thick stainless steel, the head, which is facing the plasma, is made of 1.27 cm thick molybdenum, not just because of its favorable high temperature properties but also because molybdenum is the same first wall material that Alcator C-Mod employs. Since the probe is not retrievable without a vacuum break, all components in vacuum have to tolerate periodic baking at temperatures of up to ≈150 °C.

The heart of the spectrometer is an ion-implanted-silicon detector (see Fig. 4.2) that is bakeable up to 200 °C. It is located at $R = 92.4$ cm and has an active area of 100

mm^2. Its nominal depletion depth of 300 μm [the physical thickness of the silicon is (525±25) μm] is thick enough to stop all types of charged fusion products produced, except the 14.7 MeV proton from the D-^{3}He reaction.[1] The ion-implanted-silicon detector (EG&G ORTEC Ultra series) is similar to the SBD discussed in Chapter 3. Whereas the junction in an SBD is formed between the silicon wafer and a front metal layer, the one in an ion-implanted-silicon detector is a p-n junction formed by changing the dopant type at the front of the n-type silicon wafer to p-type. The dopant ions are "implanted" on the front surface of the silicon by an ion beam from an accelerator.

Fitted within the molybdenum probe head is a cylindrical stainless steel aperture cup with three rows of six apertures each — 18 apertures in all (see Fig. 4.3). Each aperture is defined by its "gyro" angle (see also Fig. 4.4), dimensions, and the thickness of its aluminum foil (mounted on the inside of the cup). The cup can be rotated a full 360° and translated up to 2.5 cm along the probe's axis. This freedom of motion is possible through the coupling of the cup to a manually operated combination rotary and linear motion feedthrough.

There are three slits at three different major radii on the molybdenum probe head. Only one aperture at a time can be aligned with one slit. This design gives flexibility in the experimental setup since one can

- vary the CFP pitch angle by changing the tilt angle (the position of the chosen aperture with respect to the 60° wide slit),

- vary the observation gyroangle (the viewing angle of the aperture with respect to the detector normal),

- choose to eliminate certain particle species (thickness of aluminum foil),

- control the signal level (dimensions of the aperture and/or choice of slit).

---

[1]As it turned out, a detector that is thick enough to stop 14.7 MeV protons and that fulfills the baking temperature requirement is not available. With a range of about 1300 μm in silicon, a 14.7 MeV proton, while traversing the depletion depth of the present detector, deposits about 2 MeV [35].
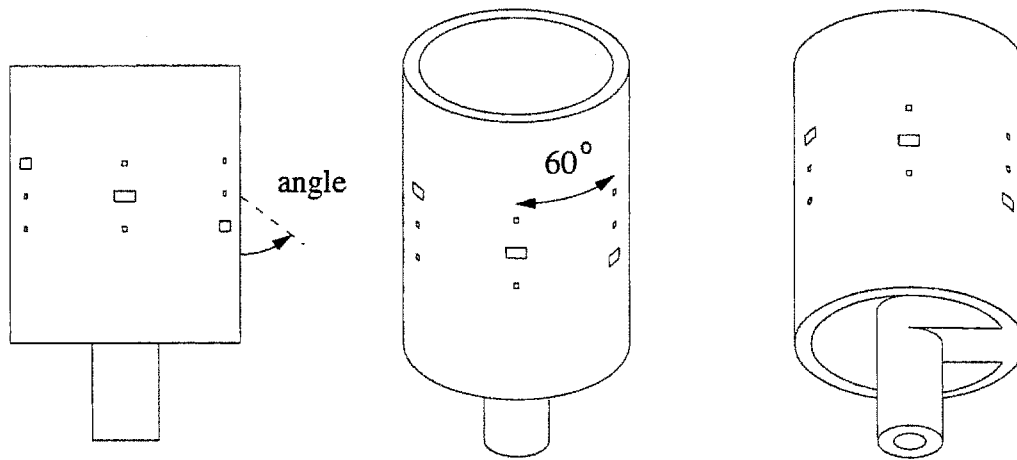
degrees mm microns	Column 1	Column 2	Column 3	Column 4	Column 5	Column 6
angle dimensions* Al thickness	80 4x2 100	80 1x1 100	80 1x1 20	80 4x2 20	110 1x1 0.65	110 1x1 0
angle dimensions* Al thickness	no hole	80 0.4 d 100	80 0.4 d 20	70 0.4 d 3	70 4x2 3	70 1x1 3
angle dimensions* Al thickness	50 0.4 d 100	50 1x1 100	50 4x2 100	60 0.4 d 20	60 1x1 20	60 4x2 20

Figure 4.3: Detailed look at the aperture cup. Each aperture is defined by its gyro angle, dimensions, and the thickness of its aluminum foil. Dimensions are either width x height, for a rectangular hole, or diameter (with "d"), for a circular hole.
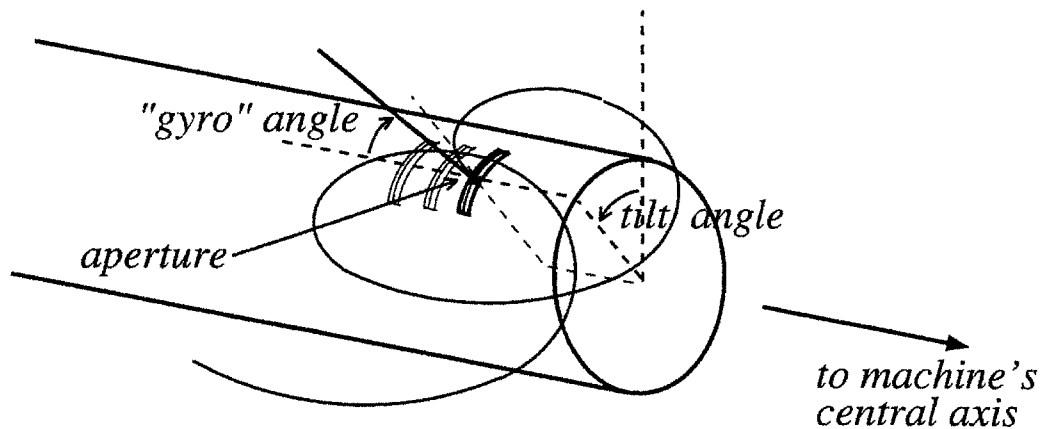
Figure 4.4: Sketch of slit/aperture of the CFP spectrometer. Besides its position (R, Z), the aperture used for detection is characterized by its dimensions, its tilt angle, its gyro angle, and the thickness of the aluminum foil behind it.

The alignment of any aperture with the detector offers no direct line of sight between the detector and the plasma itself. The presence of the aluminum foil also serves as a shield of the detector against visible light from outside the spectrometer assembly. This is important because the ion-implanted-silicon detector is sensitive to visible light. The slits on the molybdenum probe head, which are on the upward-facing side of the probe, are designed for Alcator C-Mod's magnetic field helicity with a downward ion ∇B drift. When the ion ∇B drift is upward for certain runs where the magnetic field and the plasma current direction are reversed, the spectrometer is not expected to detect any CFPs.

4.2 Electrical Design

When a charged particle strikes the silicon detector, electron-hole pairs are created along the track of the charged particle through the silicon. For each charged particle event, the separation and collection of the electrons and holes at the opposite ends
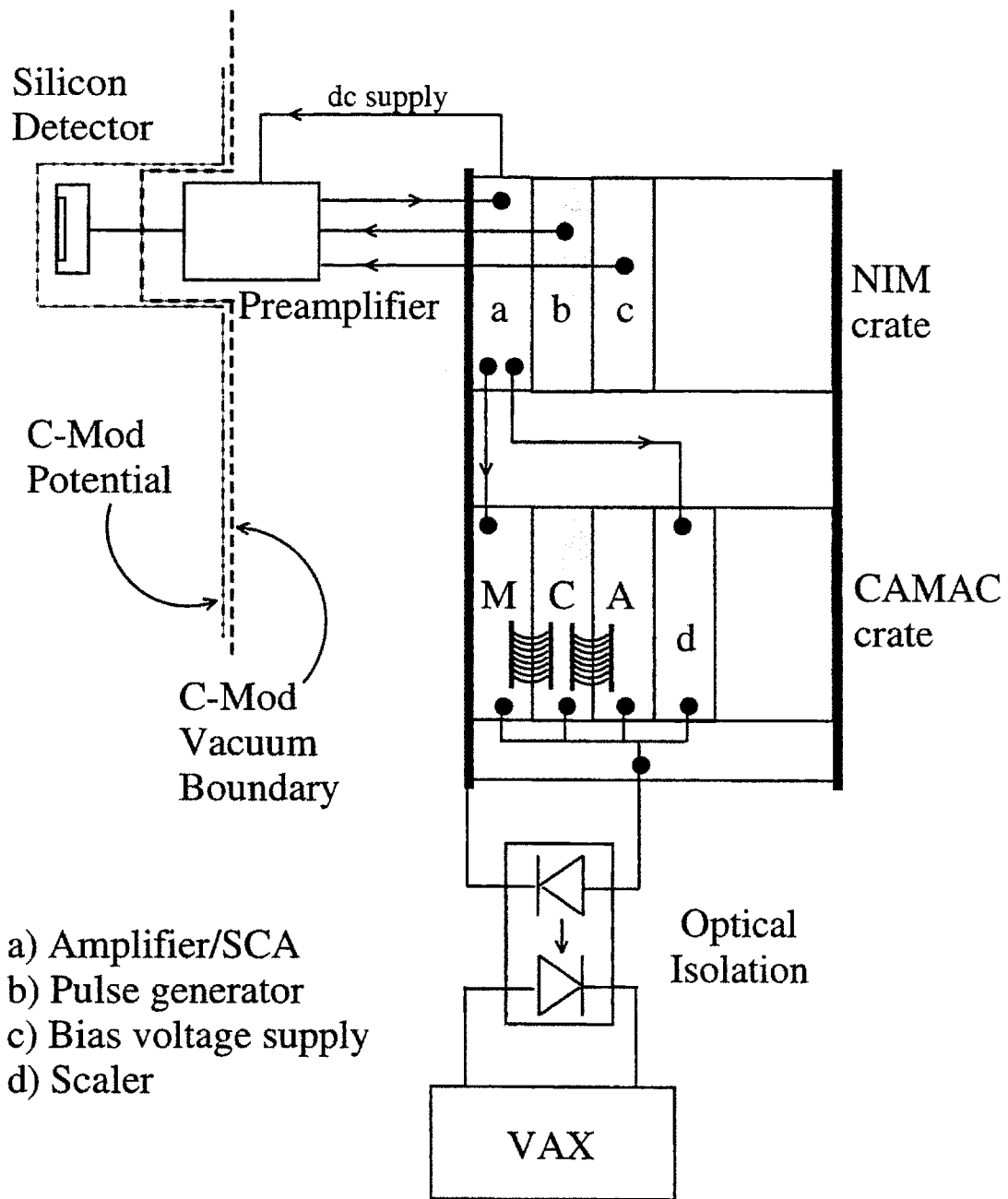
Figure 4.5: Schematic diagram of the electronics of the CFP spectrometer. The only component in the electronics chain that is in the C-Mod vacuum is the silicon detector. None of the system is connected directly to the potential of C-Mod. Data is sent to the VAX computer via optical fiber.

of the silicon junction constitute a current pulse. The number of electron-hole pairs generated, i.e. the number of charges in the current pulse, is directly proportional to the initial energy of the charged particle. See Chapter 3 for a detailed discussion of the physics around the charge generation in the silicon.

A schematic diagram of the electronics for the spectrometer is shown in Fig. 4.5. Every charge pulse leaving the silicon detector is converted by a charge-sensitive preamplifier[2] to a voltage pulse the amplitude of which is proportional to the total charge. The preamplifier is located just outside the vacuum feedthrough. The pulse is further amplified and shaped by a linear amplifier[3] before it is processed by a multichannel analyzer (MCA)[4] for pulse height analysis. Roughly speaking, the MCA digitizes the pulse amplitude of each pulse and sorts them into a histogram of number of events *vs.* pulse amplitude, which is equivalent to number of events *vs.* energy.

The amplifier module also has a built-in single channel analyzer (SCA), which operates in parallel with the MCA. The SCA takes the output pulse from the amplifier and produces a corresponding logic pulse if the amplifier pulse's amplitude falls within some preset range (*e.g.*, 2–8 V). These logic pulses are then recorded over a fixed period of time by a scaler. Whereas the MCA typically collects a spectrum every 100 ms 16 times for the purpose of pulse height analysis, the scaler records counts at a higher rate of repetition, typically every 2 ms for over 2 s. The silicon detector operates under a reverse bias of 100 V which is provided by a bias voltage supply module through the preamplifier circuit to the detector.

Towards the later part of the 94–95 campaign, a pulse generator (pulser) was installed in the system. The pulser injects periodic pulses of a fixed magnitude into the preamplifier. These pulses, acting as mock charged particles, are converted into counts centered about a certain channel in the energy spectrum and a localized pulser peak is formed. The pulser peak typically has a full width at half maximum of about

---

[2]EG&G ORTEC 142A preamplifier.

[3]EG&G ORTEC 590 amplifier/SCA.

[4]LeCroy 3512 buffered analog-to-digital converter, 3587 data router, and 3588 histogramming memory modules.

3–4 channels (there are 1024 channels in the full scale of the MCA). Changes to the size and shape of the pulser peak provide a way to monitor the possible changing behavior of the electronics during a plasma discharge. For instance, any pulser peak broadening is a measure of the spectral broadening that exists through the electronics and can be accounted for.

The amplifier, bias voltage supply, and pulser are installed in a NIM crate while the MCA and the scaler are in a CAMAC crate. Both crates are housed in the same diagnostic cabinet in the Alcator C-Mod experimental cell. The whole spectrometer system is isolated from the potential of the vacuum vessel through insulation and an isolated coaxial vacuum feedthrough, and is grounded at the ground of the diagnostic cabinet. The pulse height analysis signals are passed via an optical link to the VAX computers where they are archived.

4.3   Later Modifications

Certain modifications to the design of the CFP spectrometer were made for Alcator C-Mod's operating campaign starting in the fall of 1995. First, most of the length of the cable connecting the detector and the preamplifier in the design described earlier has been eliminated. In the new design shown in Fig. 4.6, the preamplifier input is only about 3 inches from the detector. The reduction of the cable preceding the preamplifier serves to minimize noise pickup due to the capacitive loading. Secondly, the back of the detector is shielded with tungsten to reduce the hard x ray flux on the detector. In addition, a 1.27-cm stainless steel shield has been added to the outside of the spectrometer for added shielding.

As a result, several other changes have to be made. The requirement for close proximity between the detector and the preamplifier results in the use of a reentrant design. The head of the probe is still made out of molybdenum, but the stainless steel body of the reentrant probe (5.72 cm o.d.) is only 1.6 mm thick to give as much room within as possible. A new tubular preamplifier that can be placed deep inside this
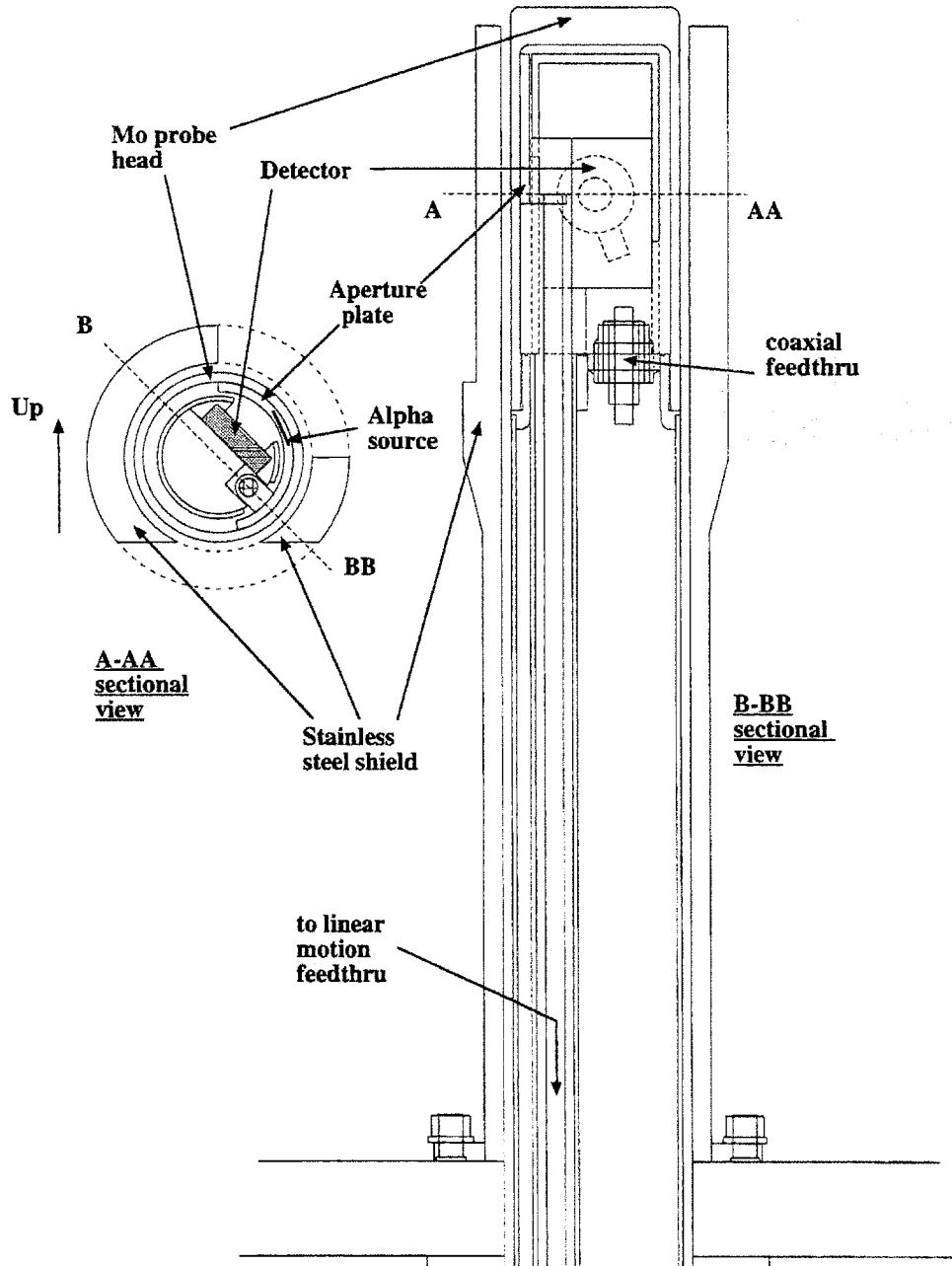
Figure 4.6: In this new design of the CFP spectrometer, the vacuum boundary is brought close to the detector to minimize distance between the preamplifier (not shown) and the silicon detector. In addition, the back of the detector is shielded with tungsten to reduce the hard x ray flux on the detector. A stainless steel shield is also added outside of the probe.
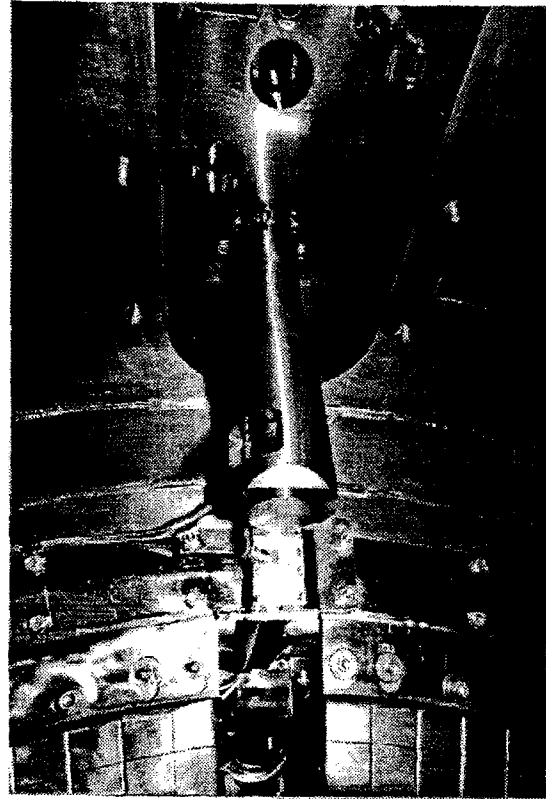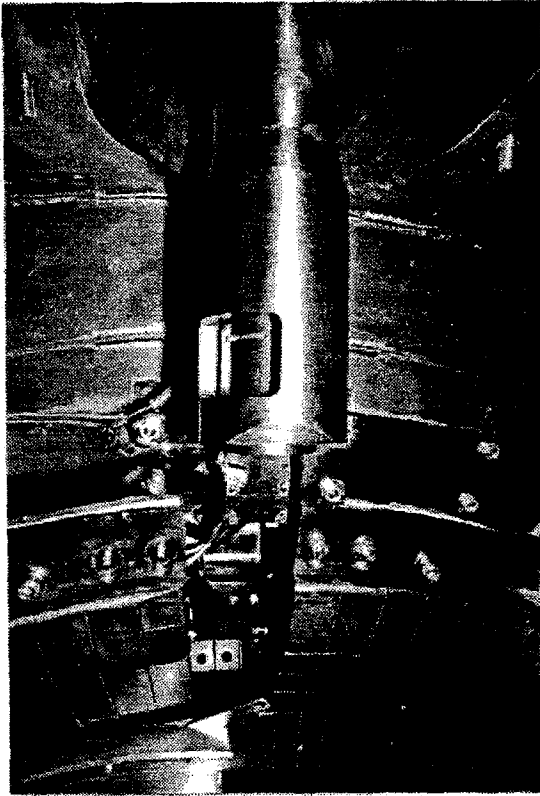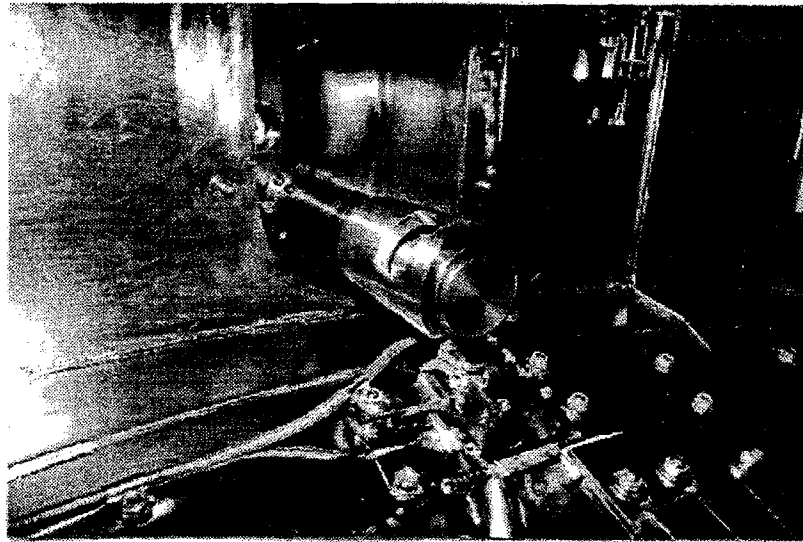
Figure 4.7: In-vessel pictures of the modified version of the CFP spectrometer at K port. Top: Side front view, looking from the direction of G port toward K port. Bottom left: Top view, showing slit on the molybdenum head behind the large opening through the stainless steel shield. Bottom right: Top front view.

71

reentrant tube has been built. The SMA-type isolated coaxial vacuum feedthrough at the deep end of the reentrant tube allows for easy installation and removal of this preamplifier. However, in the same reentrant tube has to been placed the hardware for changing apertures, if a variety of apertures is still desired. Therefore, a new aperture plate which allows axial movement with respect to the probe replaces the original aperture cup, as the controlling shaft is shifted off-centered from the probe's axis. The 20 apertures in this aperture plate give a selection of 5 distinct tilt angles, 2 aperture sizes (1 mm by 1 mm, or 1 mm by 4 mm), and a choice of two aluminum foil thicknesses (3 μm and 20 μm).

Due to the spatial constraint added by the tungsten, two changes have been made to the detector. The new detector is identical to the old one except that a side connection mount is used. In the previous version, the connection mount is on the back of the detector. At the same time, the new detector is turned facing the apertures such that the normal vector of the detector's front is 45° off vertical.

4.4 Calibration

In-vessel calibration is provided by a weak radioactive source of α particles. This mixed source of a total activity of 0.1 μCi has two dominant α lines: ^{241}Am at 5.48 MeV and ^{244}Cm at 5.80 MeV. The use of two isotopes give two separate energies for establishing the calibration. The precise distance between the detector and the source varies as the source is mounted on the movable aperture cup/plate in the old/new design. To avoid radiation damage from the α particles, the source is covered by an aperture which keeps the rate of α particles reaching at of order 100/min. A calibration spectrum taken with the spectrometer in vacuum is shown in Fig. 4.8. The detector has been tested to have an energy resolution of $\sim$20 keV.
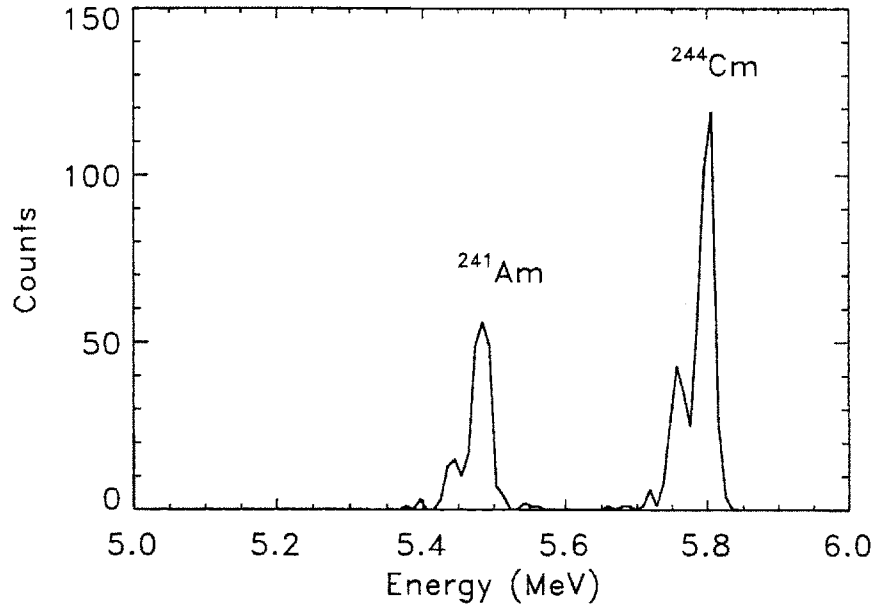
Figure 4.8: In-situ calibration is routinely performed in vacuum. The two prominent lines are from ^{241}Am (5.48 MeV) and ^{244}Cm (5.80 MeV).

4.5 Dead Time Correction

In a charged particle detection system, two successive particles can be distinguished and recorded as separate only if they are detected a certain minimum amount of time apart. The time is needed for the signal pulse to be processed by the electronics. This minimum time separation is called the dead time τ_{dead} of the system. Because of the random nature of fusion reactions, there is always a finite probability that a CFP reaching the detector is not recorded because it hits the detector too soon after a preceding CFP's impact. When high count rates ($\gtrsim$ 10% of $1/\tau_{dead}$) are encountered, the losses due to dead time become significant and measures to account for the effect need to be implemented.

The dead time response of the CFP spectrometer system is studied experimentally during plasma discharges by observing the pulser signals in the energy spectrum. The periodic signal from the pulser and the random signals from CFPs, neutrons,
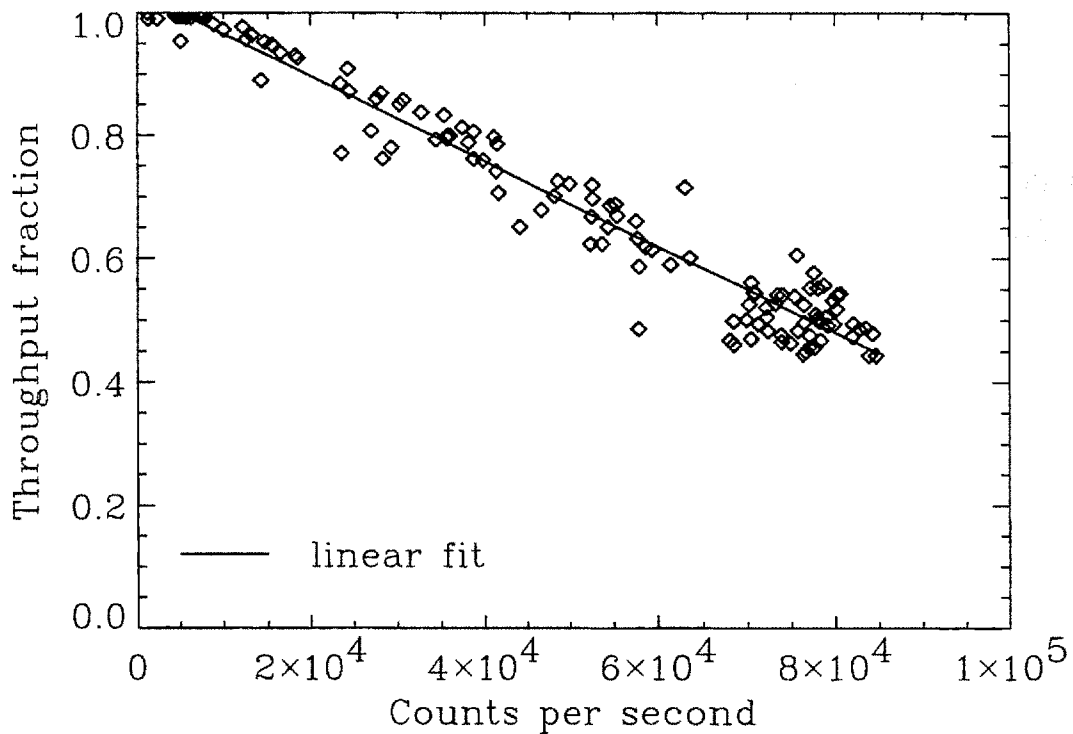
Figure 4.9: Pulser signal throughput (*i.e.*, ratio of recorded counts to expected counts) of the system as a function of the total recorded count rate. The observed throughput reduction is due to the dead time of the system.

etc. during a discharge are all processed by the CFP spectrometer system. Since the pulser pulse frequency is a pre-determined constant, any reduction to this expected pulser count rate in the resulting spectra gives a measure of the deadtime correction that has to be made. The count rate of CFPs can be expected to be reduced by the same fraction. If a relationship can be found between the fraction of counts that is lost and the observed count rate, then a correction to the observed count rate can be made.

Figure 4.9 shows the pulser signal throughput (ratio of recorded counts to expected counts) of the CFP spectrometer system as a function of the total recorded count rate.
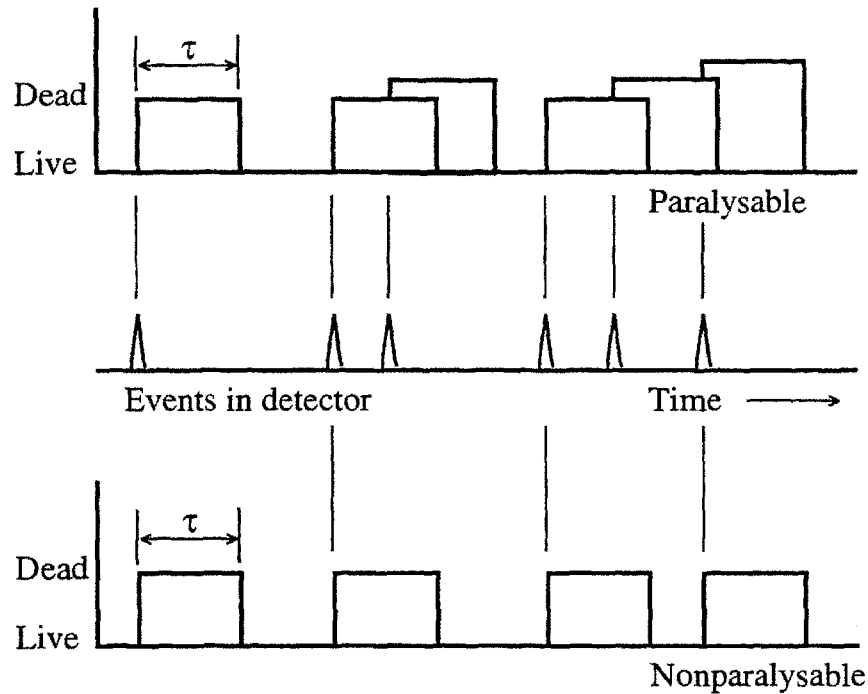
Figure 4.10: Illustration of the *nonparalysable* and *paralysable* models of dead time behavior in a radiation detection system.

The data suggests a linear fit of

$$f = 1.04 - 6.94 \times 10^{-6} c_{rec}, \tag{4.1}$$

where f is the throughput as measured from the pulser signal, and c_{rec} is the recorded count rate in counts per second (cps). The throughput of the system is unity when the count rate is low, and is seen to decrease monotonically with an increasing recorded count rate.

The observation can be explained by the so-called *nonparalysable* model for dead time response (see, for instance, Ref. [43]). The model assumes that a particle event during the dead period is lost and leaves no effect whatsoever on the behavior of the detector. It is as if the "lost" particle were not there in the first place. An opposite to this is the *paralysable* model which assumes that a particle event during a pre-existing

dead period would prolong it by initiating a new dead period of the same dead time starting when that particle arrives. The particle is still lost, but the effective dead time becomes longer the higher the count rate. These two contrasting models are shown in Fig. 4.10.

In the nonparalysable model, the fraction of all time that the system is "dead" is given simply by $c_{rec}\ \tau_{dead}$. Therefore, the rate at which true counts are lost is simply $c_{true}\ c_{rec}\ \tau_{dead}$. Since the rate of true count losses is also $c_{true} - c_{rec}$, these two expressions are equivalent, i.e.,

$$c_{true} - c_{rec} = c_{true}\ c_{rec}\ \tau_{dead}, \tag{4.2}$$

which leads to

$$c_{true} = \frac{c_{rec}}{1 - c_{rec}\ \tau_{dead}}. \tag{4.3}$$

This equation has exactly the same form as Eq. (4.1) since f is just c_{rec}/c_{true}. Thus, the experimentally determined dead time of the system's electronics is 6.94×10^{-6} s, or about 7 μs. This corresponds to the manufacturer's specification of a 7 μs dead time in the MCA. The dead time behavior of the system is nonparalysable and is limited by the MCA. Dead time correction can now be applied to the CFP data to compensate for CFP counts that are lost through the electronics.

Chapter 5

Orbit Calculations

5.1 Charged Fusion Product Orbits

In the presence of a magnetic field, a charged particle with finite energy undergoes a helical motion, characterized by the Larmor radius described in Eq. (1.5). At the nominal toroidal field of 5.3 T in Alcator C-Mod, the Larmor radius of a 3 MeV proton (or a 1 MeV triton) is about 25% of the minor radius, and that of a 14.7 MeV proton is half the minor radius. These scalelengths, of course, are increased substantially when Alcator is operating at a lower toroidal field because the Larmor radius is inversely proportional to the magnetic field. To model the dynamics of MeV charged fusion products in this machine, it seems clear that a full orbit calculation of the trajectories should yield more accurate results compared to the simpler guiding center treatment.

Two FORTRAN computer codes, both using the same "engine" routines for integrating the Lorentz force equation to calculate the orbit of a single charged particle, have been developed. EPSILON is a 3-D code for calculating the detection efficiency of the aforementioned CFP spectrometer (see Chapter 4). Given the location of the detector, its aperture, and the magnetic field, EPSILON follows an orbit inversely in time (from the detector through the aperture back to the plasma) and performs an

integration to obtain the efficiency. The second code, PROMPT, is a Monte-Carlo simulation program for studying prompt losses of CFPs in C-Mod.

5.1.1 Physics Model of Code

As the fusion products of concern are charged particles, their motion is under the influence of electromagnetic forces. With energy in the MeV range, the forces on these charged fusion products due to electric fields in the toroidally confined plasma are much smaller than those from either the toroidal or poloidal magnetic fields present. Therefore, the electric field is always ignored, and the equation of motion of charged particles, or the Lorentz force equation is:

$$m\frac{d\mathbf{v}}{dt} = q\,\mathbf{v} \times \mathbf{B},$$

(5.1)

where m is the particle's mass, $\mathbf{v}$ is the particle's velocity, t is time, q is the particle's charge, and $\mathbf{B}$ is the magnetic field. Integrating Eq. (5.1) and

$$\frac{d\mathbf{x}}{dt} = \mathbf{v}$$

(5.2)

over t yields the space coordinates $\mathbf{x}(t)$ of the charged particle as a function of time, i.e. the orbit. The integration is performed with the IMSL routine, DIVPAG [45], which solves an initial-value problem for ordinary differential equations using Gear's backward difference method [46]. This is the calculation that both EPSILON and PROMPT are built upon.

As orbits are rarely traced beyond one complete trapped banana (or passing) orbit, no collisions are included in the modeling. This is well justified because the bounce frequency ν_{bounce}, which characterizes the motion of these ions trapped between the tips of their banana orbits, is orders of magnitude larger than the collision frequency for energy loss, the highest being that between these MeV ions and electrons ν^{ie}. The

bounce frequency is given by

$$\nu_{bounce} = \frac{1}{2\pi} \frac{v}{R_0 q} \sqrt{\frac{2r}{R}}, \tag{5.3}$$

while the collision frequency for energy loss, ignoring electron thermal motion, is

$$\nu^{ie} = n_e \frac{Z^2 e^4}{(4\pi\epsilon_o)^2} \frac{8\pi \ln \Lambda}{m_e m_i v_i^3}. \tag{5.4}$$

where subscripts i and e refer to the charged fusion product and the electron, respectively. Assuming that $\ln \Lambda \cong 15$, $n_e = 10^{20} m^{-3}$, and $q \sim 2$–3, one finds that for a typical 3 MeV proton in Alcator C-Mod, $\nu_{bounce} \sim 1 MHz \gg \nu^{ie} \cong 100 Hz$. Therefore, without treating collisions in the formalism of the code, a particle's energy is supposedly constant throughout the calculations. The tracking of the energy usually shows $\sim 1\%$ variation during a particle's first orbit.

As the orbit is followed in time, a decision has to be made on whether a particle has hit the wall. At each timestep, this becomes a two-dimensional problem and the appropriate poloidal projection of the vacuum vessel's cross section is used. Figure 5.1 shows the different polygonal boundaries used to include the presence of the RF limiters at certain toroidal locations around the Alcator C-Mod vessel (a split limiter between G and H ports, and two full limiters between F and G ports and between A and B ports). A reliable and fast algorithm developed by Chen and Townsend [47] that minimizes the number of floating point operations per query is used to handle the point inclusion problem (to determine whether or not a point is contained within a polygonal boundary). The algorithm, written in C, is based on the principle of using binary coded coordinate systems and parity counting of the number of intersections of the polygon boundary with an infinite vector.

79
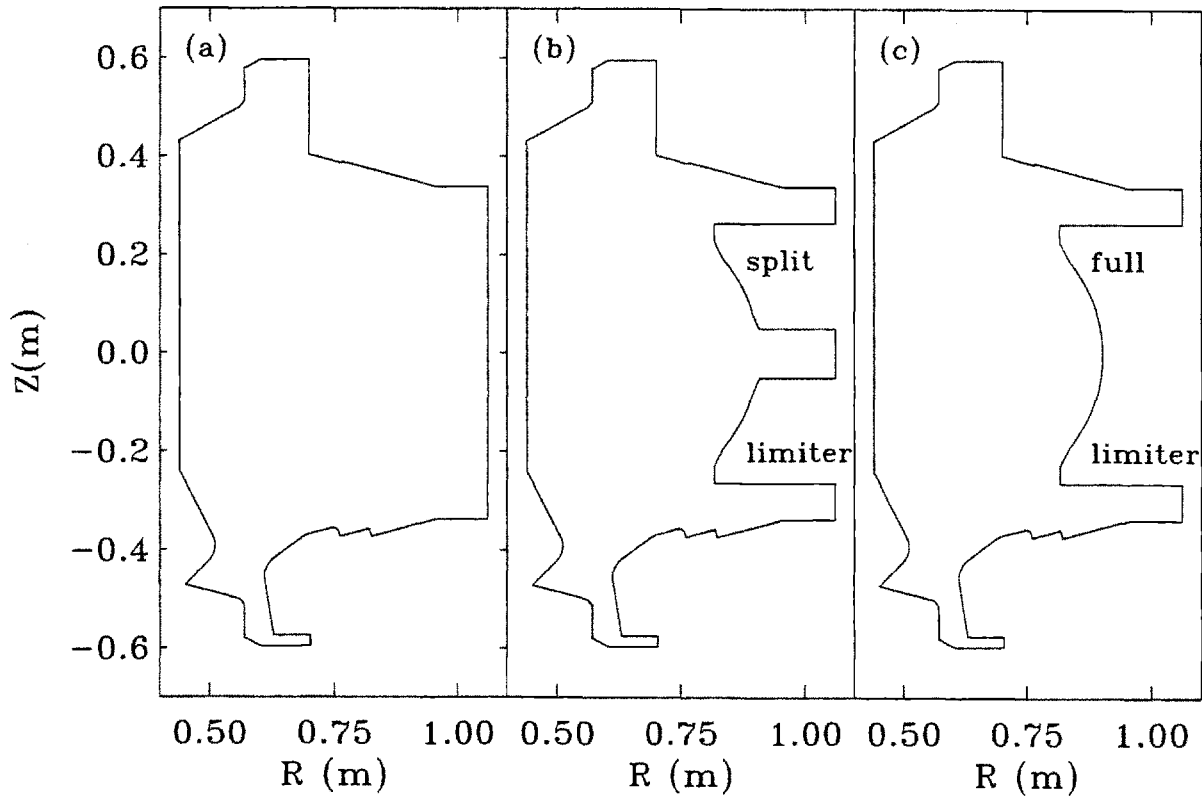
Figure 5.1: The bounding surfaces on the left (a) signify the first wall of Alcator C-Mod defined by molybdenum tiles and divertor plates. This is used at most toroidal locations for checking whether a particle is lost. However, there are 3 outboard RF limiters around the tokamak such that the bounding surfaces are more confining. A split RF limiter (b) is located between G and H ports. The other two, located between F and G ports and between A and B ports are full limiters (c).
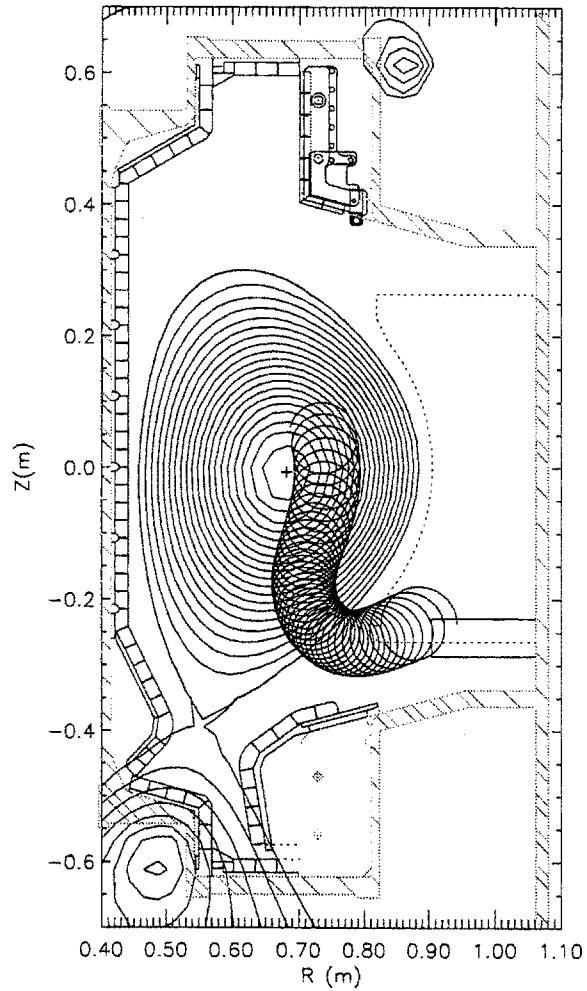
Figure 5.2: Typical orbit of a trapped 3 MeV proton (or 1 MeV triton) at $B_\varphi = 5.3$ T and $I_p = 820$ kA. The bounding surfaces surrounding the orbit signify the first wall of Alcator C-Mod defined by molybdenum tiles and divertor plates. This particular particle clears the RF limiter (dotted lines) and is intercepted by the spectrometer.

5.1.2 Inputs

The calculation utilizes the interchangeable toroidal (R, Z, φ) and cylindrical (r, θ, φ) coordinates. (Refer to Fig. 1.1 for a schematic.) One of the inputs is the magnetic field geometry, which is assumed to be axisymmetric. Both the toroidal magnetic field $B_\varphi(R, Z)$ and the poloidal magnetic field, given in B_R and B_Z, are specified in a finite grid structure on the poloidal plane. There are 33 evenly spaced grid points in both the R (from 0.4 m to 1.1 m) and Z (from -0.7 m to 0.7 m) directions. Linear interpolation provides the magnetic field at any point on this grid.

In cases involving an Alcator C-Mod plasma discharge, the magnetic field geometry is supplied through equilibrium reconstruction calculations using magnetic and coil current measurements and the EFIT code [21]. When the CFP spectrometer was being designed before C-Mod operation began, precalculated equilibria from an MHD database [48] was the source of the magnetic field geometry and a vacuum toroidal field was assumed.

Other general inputs include the charge, the mass, the energy, the initial position and initial direction of the particle. Figure 5.2 shows a typical particle orbit for a 3 MeV banana-trapped proton starting from inside the plasma. (This can also be interpreted as a 1 MeV triton orbit as these two particles have identical momenta.) The vacuum vessel bounding surface as it appears in the figure is the first wall defined by the molybdenum tiles and divertor plates.

5.1.3 Fusion Source Profile

In both EPSILON and PROMPT, a certain fusion product source profile S has to be assumed. The fusion source rate is given by

$$S = \frac{1}{2} n_D^2 \langle \sigma v \rangle_{DD} \tag{5.5}$$

82
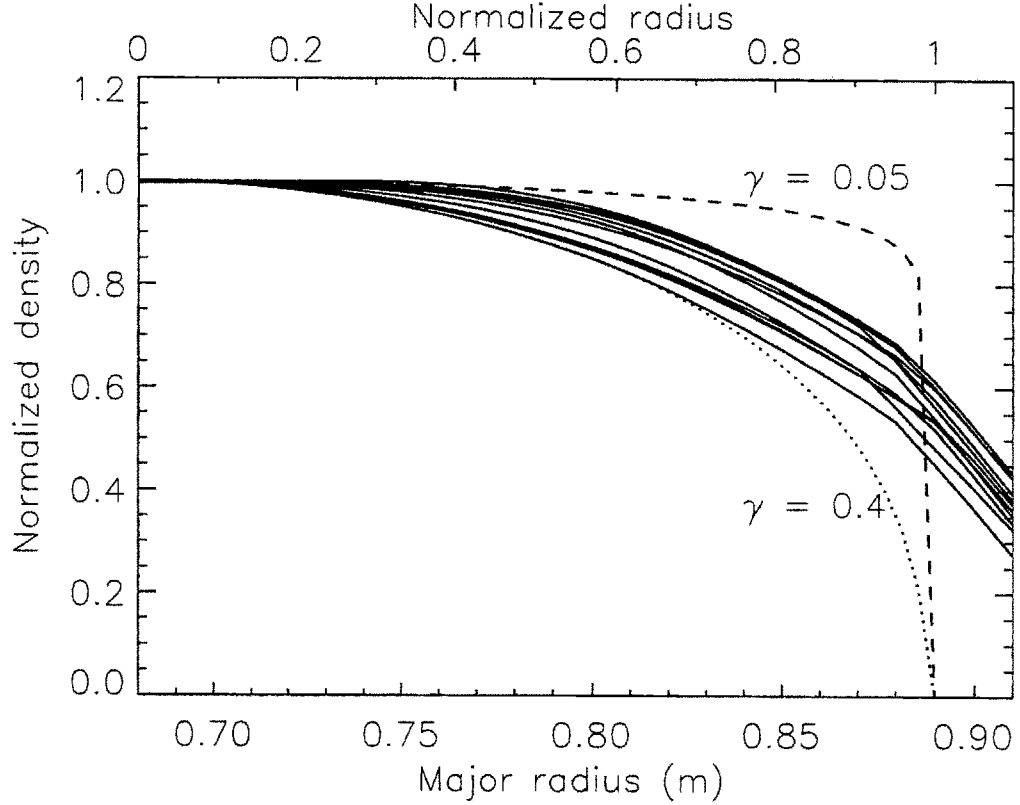
Figure 5.3: Density profiles (solid traces) at $t = 0.2, 0.3, \ldots, 1.2$ s observed in Alcator C-Mod during a typical ohmic discharge (flattop from 0.5 to 1.0 s). The profiles are typically quite flat and falls within parabolic profiles with exponent of $0.05 \leq \gamma \leq 0.4$.

where n_D is the deuterium ion density, and $\langle \sigma v \rangle_{DD}$ is the D-D fusion reactivity averaged over the deuterium velocity distribution function. For ion temperature $T_i \lesssim$ 25 keV, the following approximation (in units of $cm^3 s^{-1}$) can be used [49]:

$$\langle \sigma v \rangle_{DD} = 2.33 \times 10^{-14} T_i^{-2/3} \exp(-18.76 \ T_i^{-1/3}) \ , \tag{5.6}$$

where T_i is in keV.

Through Eqs. (5.5) and (5.6), the idea is to arrive at a convenient analytical form of the source profile, $S(\mathbf{r}) = S(r)$, using density and temperature profiles seen in Alcator C-Mod. It turns out that an electron density profile of $n_e \propto [1 - (r/a)^2]^{\gamma}$

with a density peaking factor γ between 0.05 and 0.4 can be assumed. In Fig. 5.3, the normalized electron density profiles at $t = 0.2, 0.3, \ldots, 1.2$ s during an ohmic discharge in Alcator C-Mod with a current flattop from 0.5 to 1.0 s are shown. These profiles are obtained from the two-color interferometer system [20]. Bounded between these profiles are the representative parabolic profiles with $0.05 \leq \gamma \leq 0.4$. Making the reasonable assumption that the plasma Z_{eff} in Alcator C-Mod is roughly constant in space, these profiles can be interpreted as deuterium ion density profiles. The ion temperature profile in Alcator C-Mod plasma is not measured routinely by the five-chord high-resolution x-ray (HIREX) spectrometer. However, an assumed ion temperature profile of $T_i \propto [1 - (r/a)^2]^\delta$ with a temperature peaking factor $\delta \sim 1.5 \pm 0.5$ is reasonable to use [50].

Figure 5.4 shows calculated fusion source profiles using Eqs. (5.5) and (5.6) and parabolic density and temperature profiles with a reasonable range of peaking factors γ's and δ's. Superimposed on each plot for comparison are assumed source profiles bearing the form

$$S(\mathbf{r}) = S(r) = S_o \left[1 - \left(\frac{r}{a} \right)^2 \right]^\alpha \qquad (5.7)$$

for a range of source peaking factor α $(2, 4, \ldots, 12)$. It turns out that the shapes of the assumed centrally peaked source profiles given by Eq. 5.7 (dotted curves) are reasonably good approximations to the calculated profiles. The advantage of using an assumed profile as an approximation is that it has a simple analytic form. For a fixed temperature profile, the variation in the fusion source profile is small within the assumed range of $0.05 \leq \gamma \leq 0.4$. So, for $\delta = 1.5$, a good assumed source profile to use seems to be one with $\alpha = 8$. Variation of the temperature profile in terms of $\delta = 1.5 \pm 0.5$ results in a source profile variation characterized by $\alpha = 8 \pm 2$. In both EPSILON and PROMPT, α is a user-defined constant, and $\alpha = 8$ is typically assumed. A sensitivity study of the effect of the source profile on the detection efficiency can be found in §5.2.3.
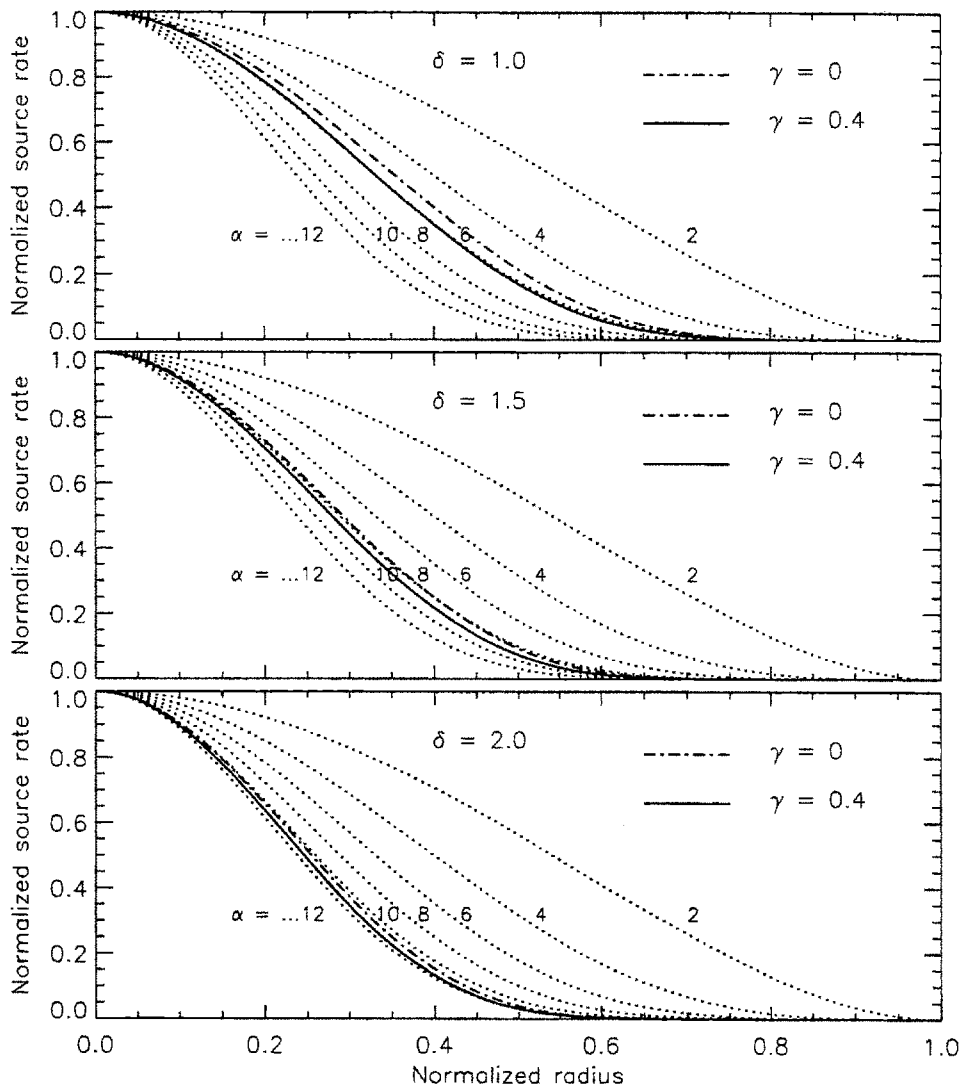
Figure 5.4: Calculated source profiles (solid and dash-dot traces) for different temperature and density peaking factors based on Eqs. (5.5) and (5.6). Superimposed on each plot for comparison are assumed parabolic fusion source profiles with different source peaking factor for comparison.
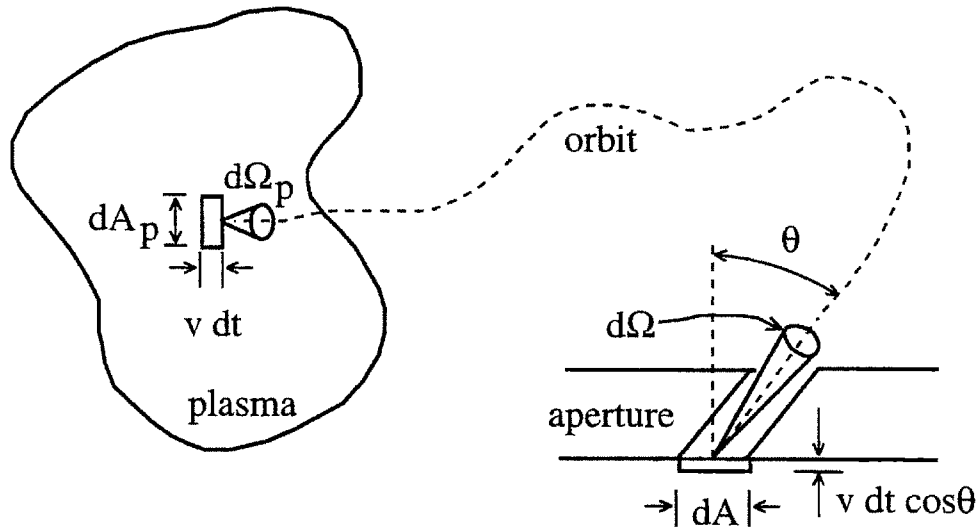
Figure 5.5: Picture of the phase space volume element in the plasma that sends CFPs into the phase space volume element in the aperture. The detector, not shown in this picture, can be right behind the aperture or some distance away. In the latter case, a check has to be made in the efficiency calculation to make sure that an orbit ends on the detector.

5.2 Detection Efficiency Calculations

5.2.1 The Code EPSILON

The detection efficiency ϵ of a charged particle detector is defined as the fraction of all the charged particles emitted from the plasma that is collected by the detector. In an environment with no magnetic field, this can be found by simply considering issues of acceptance solid angle formed between the particle source and the detector. However, in the tokamak environment, the determination of the detection efficiency of the CFP spectrometer requires an orbit calculation. This is the function of the code EPSILON. As the magnetic field geometry varies throughout a plasma discharge, the detection efficiency is affected as the collection of orbits accepted by the fixed aperture of the spectrometer go through different portions of the plasma. In the initial design phase of the spectrometer, the code was also instrumental in estimating the expected signal

level as a function of the proposed spectrometer location under a given condition.

For a charged fusion product detector, the detection efficiency can be expressed in an analytical form, developed by Chrien [51]. Consider a small area dA_p in the plasma that emits CFPs into a solid angle $d\Omega_p$ for a time dt (see Fig. 5.5). This volume in phase space in the plasma is given by $dA_p(v\,dt)(v^2\,d\Omega_p dv)$. (With no energy loss assumed, the velocity $v = |\mathbf{v}|$ is constant.) Since each charged particle's equation of motion Eq. (5.1) originates from a Hamiltonian, phase space is conserved throughout each particle's motion from the plasma to the detector. In other words, the six-dimensional phase-space volume of the plasma that emits the particles successfully measured by the detector is exactly equal to the six-dimensional phase-space volume defined by the aperture's acceptance solid angle to the detector. This volume at the bottom of the aperture is $\cos\theta dA(v\,dt)(v^2\,d\Omega dv)$ where A is the area of the aperture, Ω is the solid angle defined by the aperture, and θ is the angle formed by the incident proton orbit and the normal to the aperture plate. The quantity $v\,dt$ can further be replaced by the differential orbit length dl.

The detection efficiency is the sum of all the six-dimensional volumes the detector views divided by the total six-dimensional volume of the plasma, each weighted by the fusion source function $S(r)$ to reflect the likelihood of fusion products being created in a given part of the plasma. This has the expression [52]:

$$\epsilon = \frac{\iiint S\cos\theta\,dl\,d\Omega\,dA}{\iiint S\,dl\,d\Omega_p\,dA_p} = \frac{\iiint S\cos\theta\,dl\,d\Omega\,dA}{4\pi \int S\,dV} \tag{5.8}$$

where S is the fusion source function given, again, by Eq. (5.7), and $dV = dl\,dA_p$ is the plasma volume element in coordinate space.

Starting from the detector through the specified aperture back into the plasma, the particle orbit is followed backward in time and the code performs a source (i.e., S) weighted integral along the orbit dl. In the calculation, the aperture to the detector is assumed to be rectangular in shape; to perform a calculation for an aperture of a different shape, an equivalent rectangular aperture has to be used instead. The finite
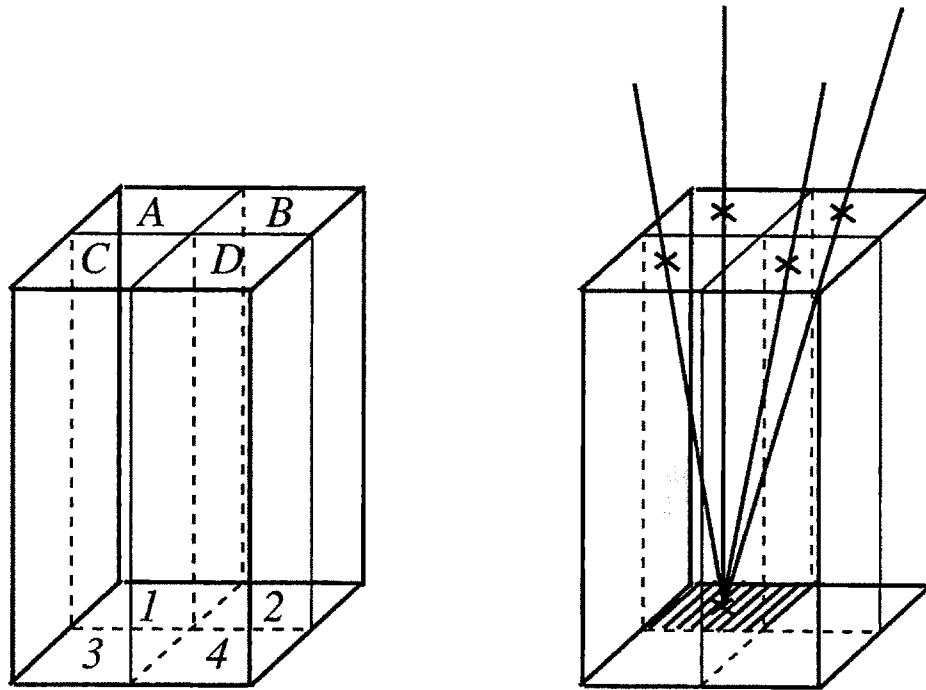
Figure 5.6: To achieve a more precise result in the detection efficiency calculations, the aperture can be subdivided into a finer rectangular array of sub-apertures for which efficiencies are calculated separately, and summed. Shown here are 2×2 arrays where 16 calculations have to be added together at the end. Sketched on the right are four trajectories: 1-A, 1-B, 1-C, and 1-D.

dimensions of the inner and the outer openings of a particular aperture determine the solid angle in the integration calculation. To achieve a more precise result, the aperture can be subdivided into a finer rectangular array $(n \times n)$ of sub-apertures for which efficiencies are calculated separately, and summed. Figure 5.6 shows an example of an array of 2×2 sub-apertures. Figure 5.7 shows the convergence of the calculated efficiencies for three arbitrary aperture arrangement. In light of the fast convergence of the calculated efficiency with increasing degree n of aperture subdivision, typical efficiency calculations for 1 mm × 1 mm apertures are done using 3×3 arrays to

88
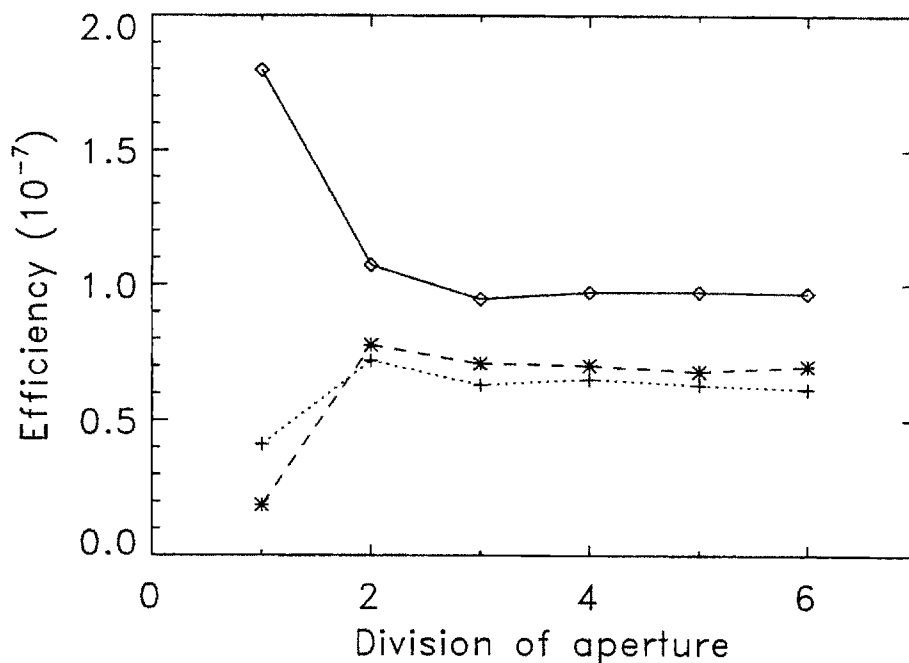
Figure 5.7: Convergence of calculated efficiency with increasing degree of aperture subdivision for three arbitrary conditions. (A division of 2, for instance, means a 2×2 subdivision.) In light of the fast convergence of the calculated efficiency with increasing degree of aperture subdivision, a 3×3 array is typically used.

conserve computation time. (Computation time goes as n^4.)

In the case of a detector that is not immediately behind the aperture, but some distance away, a check has to be made first to determine whether an orbit through the aperture/sub-aperture indeed intercepts the detector. In such a case, each orbit that is followed backward in time from the aperture into the plasma is preceded by an orbit that is followed forward in time to make this check. If the check result is negative, then no orbit is followed into the plasma for that aperture/sub-aperture.

At the selected location of the charged fusion product spectrometer ($R = 92.4$ cm, $Z = -25.8$ cm; see Chapter 4) with an aperture of 1 mm^2 and under the conditions of $B_\varphi = 5.3$ T and $I_p = 0.8$ MA, ϵ for 3 MeV protons is calculated to be in the range of
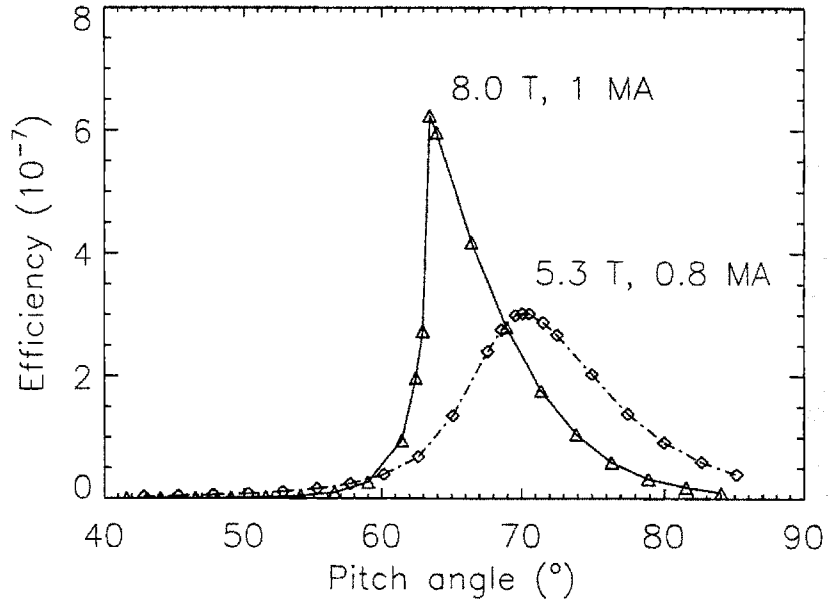
Figure 5.8: Study of efficiency *vs.* pitch angle at the aperture ($R = 83.3$ cm, $Z = -25.8$ cm) of the detector.

$\sim 10^{-8}$–10^{-7}. If, instead, $B_\varphi = 8$ T and $I_p = 1$ MA, the expected ϵ is $\sim 10^{-9}$–10^{-8}. As the fusion rate of Alcator C-Mod is to be in the range of $\sim 10^{11}$–10^{13} per second, the signal level was judged to be adequate.

At any point, a CFP is characterized by a pitch angle χ, which is the angle between its velocity vector and the local magnetic field vector. Explicitly, the pitch angle is given by

$$cos(\chi) = \frac{v_\parallel}{v} , \qquad (5.9)$$

where $v_\parallel$ and v are the parallel (to the local magnetic field) velocity and total velocity, respectively. One test to check that the results of EPSILON make sense is to evaluate the detection efficiency at a given detector/aperture location as a function of the local pitch angle. However, because the CFP spectrometer's designed location is in the vicinity of the vessel's boundary, it is not a good location for performing this check
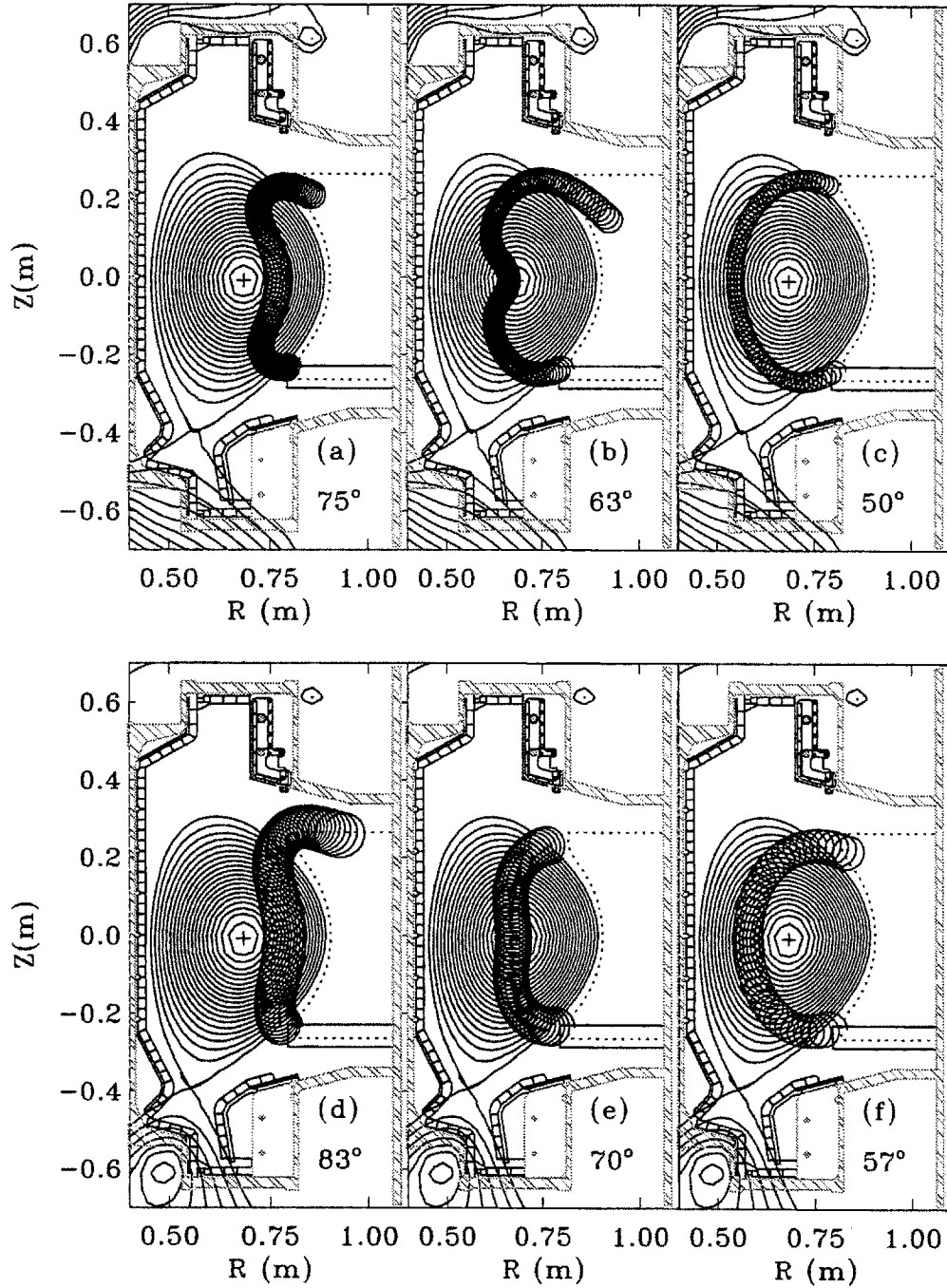
Figure 5.9: Different orbits for the 3 MeV protons. At 8T, 1 MA: (a–c) trapped ($\chi = 75°$), critical ($\chi = 63°$), and passing ($\chi = 50°$); and at 5.3T, 0.8 MA: (d–f) trapped ($\chi = 83°$), critical ($\chi = 70°$), and passing ($\chi = 57°$).

because its proximity to the walls and the RF limiter (when projected onto the same poloidal plane) may decide whether any orbits reach the detector. So the assumed detector location was set, instead, at $R = 0.82$ cm with the aperture at $R = 0.833$ cm for this study. The result for 3 MeV protons at two different conditions is plotted in Fig. 5.8.

The expected pitch angle dependence of CFP loss during its first orbit should peak around a "critical" pitch angle. This corresponds to the pitch angle marking the transition between being banana-trapped and passing. The banana is the fattest, and the orbit travels the closest to the magnetic axis (in this case actually going through it). Since the magnetic axis is also the hottest part of the plasma, the efficiency of detecting these protons should reach a maximum. Figure 5.9 gives an illustration of the different orbits for the two cases.

In the 8 T case, moving away from the critical χ of about 63° (see Fig. 5.8), the fall in the detection efficiency is found to be more gradual in the higher-χ side (trapped CFPs) than in the lower-χ side (passing CFPs). Let's examine the orbits of different χ's that reach the detector. Starting with a deeply trapped orbit (high χ), the orbit passes progressively closer to the plasma center as χ comes down. The efficiency is, thus, seen to gradually rise as χ drops. The efficiency reaches its maximum value at the point of transition from trapped to passing because the corresponding orbit spends the most time closest to the plasma center. As χ falls further, however, the passing CFP's orbit never makes it close to the plasma center and the efficiency is reduced considerably. This change happens for a small change in χ, thus explaining the sharp edge on the low-χ side of the plot.

In the 5.3 T case, however, a similarly rapid change in the efficiency with pitch angle is not seen. In Fig. 5.9(e), the bounce points of the orbit corresponding to the trapped-passing transition are at the same major radius as the magnetic axis. Thus, the transition from trapped to passing is not expected to dispel the orbit very far from the plasma center for a small change in χ. As a result, the sharp feature of the

92
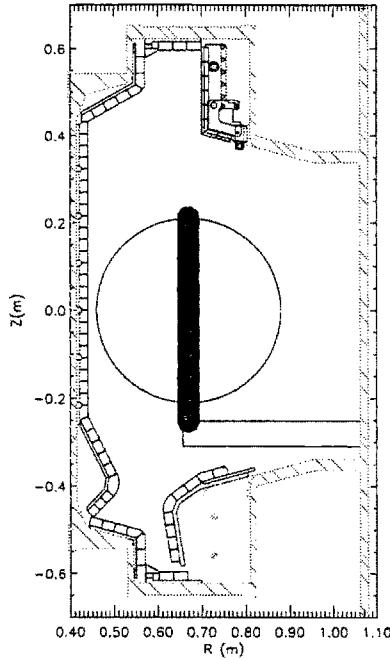
Figure 5.10: 3 MeV proton orbit in a circular plasma with $B = 10$ T and $I_p = 1$ kA.

peak at the critical angle is not found.

The presence of a sharp drop of the efficiency in the 8 T case, as calculated by the EPSILON code for an aperture withno subdivision, is sensible since changes to one single orbit is considered. In reality, the sharp feature cannot be expected for an aperture of any finite size. Such an aperture will introduce geometrical pitch angle broadening, and the effects due to a collection of orbits will have to be included. Therefore, in the calculation of the detection efficiency for any aperture, a subdivision of the aperture into at least a 3×3 array has been used.

5.2.2 Validity Check

For a given aperture, the efficiencies of detecting a 1 MeV triton and a 3 MeV proton are calculated by EPSILON to be the same. This is as expected since the two particles

have identical momenta. To convince ourselves that the calculation of efficiency is correct not just in a relative sense, cases with very low plasma current and a varying toroidal field have been studied. Low I_p cases were picked because whereas a D-D proton still gyrates due to the magnetic field (thus, providing a check of the orbit dynamics), the guiding center simply drifts downward along a straight trajectory of constant B field. The proton's gyro radius along the orbit stays unchanged. This makes it possible for the efficiency to be evaluated analytically, which can be compared to the efficiency computed by EPSILON. Figure 5.10 shows the poloidal projection of an orbit at $B = 10$ T and $I_p = 1$ kA.

This test case is set up such that the plasma is circular with $R_0 = 0.67$ m, $a = 0.21$ m, and $I_p = 1$ kA. The detector is modeled to be located at the bottom of the machine to intercept protons with orbits passing through the center of the plasma. Any obstruction of the orbit by the hardware of the spectrometer is ignored. Protons reach the detector via an aperture facing vertically upward. The aperture openings used are both 1 mm × 1 mm and they are 3.18 mm apart vertically. The aperture geometry only allows protons with little or no $v_\parallel$ to get through. In other words, protons detected are characterized by $v_\perp \gg v_\parallel$.

Now, the drift velocity v_{drift} is the sum of the ∇B drift velocity $v_{\nabla B}$ and the curvature drift velocity v_R:

$$
\begin{aligned}
\mathbf{v}_{drift} &= \mathbf{v}_{\nabla B} + \mathbf{v}_R \\
&= \frac{m}{q} \frac{\mathbf{R} \times \mathbf{B}}{R^2 B^2} \left(v_\parallel^2 + \frac{1}{2} v_\perp^2 \right) \\
&\approx \frac{m v_\perp^2}{2q} \frac{\mathbf{R} \times \mathbf{B}}{R^2 B^2} .
\end{aligned}
$$
(5.10)

The fact that B stays constant along the guiding-center trajectory allows for a simplification to the expression for the detection efficiency given in Eq. (5.8). The orbit $dl = v\,dt$, which appears in the numerator of Eq. (5.8) can be expressed in terms of

94

the trajectory of the guiding center dz by the scaling

$$
\begin{aligned}
dl &= dz \frac{v_\perp}{v_{drift}} \\
&\approx dz \frac{2\,q\,R\,B\,v_\perp}{m\,v_\perp^2} \\
&= dz \frac{2R}{\rho}
\end{aligned}
\tag{5.11}
$$

This shows that the length of the orbit (which is the summing of all dl in the plasma) scales as B, or $1/\rho$. This is because v_{drift} decreases with increasing B. Since the detection efficiency is calculated by integrating over the length of the orbit through the plasma, the efficiency should increase with the B field. Chrien [51] has also pointed out the dependence of the detection efficiency on the B field due to the drift velocity.

The line integral $\int S\,dl$ can now be approximated by integrating along the guiding-center trajectory. S is modeled by $S_0[1 - (r/a)^2]^8$, where S_0 is the source rate at the center of the plasma. The evaluation of S along the guiding-center trajectory as opposed to along the exact orbit is an approximation – a guiding-center average. (In the particular case of a guiding-center trajectory along $R = R_0$, this averaging tends to overestimate the true efficiency.) So we write (refer to App. B)

$$
\int S\,dl \approx \int_{-a}^{a} S \frac{2R}{\rho}\,dz = \frac{4R}{\rho} \int_0^a S\,dz = \frac{1.20R}{\rho}\,a\,S_0 \ .
\tag{5.12}
$$

The volume integral $\int S\,dV$ in Eq. (5.8) evaluates simply to $S_0\,V_{plasma}/9$ (App. B). Therefore, the expression for the detection efficiency given by Eq. (5.8) evaluates, in this special case, to

$$
\epsilon = \frac{\int dA \int \cos\theta\,d\Omega \int S\,dl}{4\pi \int S\,dV} = \frac{A_{aperture}\Omega_{aperture}\,(1.20\,a\,S_0\,R/\rho)}{4\pi S_0\,(2\pi^2\,R_0\,a^2)/9} \ .
\tag{5.13}
$$

Table 5.1 shows the efficiencies calculated both analytically and by EPSILON. As expected from our discussion, the efficiency, to first order, is proportional to the

95

Toroidal Field, B (T)	5.3	10	20
Proton gyro radius, ρ (cm)	4.72	2.50	1.25
Major radius of aperture, $R_{aperture}$ (m)	0.72	0.70	0.68
$\epsilon_{EPSILON}$ ($\times 10^{-7}$)	3.56	7.61	16.0
ϵ from Eq. (5.13) ($\times 10^{-7}$)	4.38	8.26	16.5

Table 5.1: Some of the important parameters of Alcator C-Mod. Nominal values are given with values in parentheses showing maximum values (some planned for future operation).

magnetic field. In other words, the volume in coordinate space of protons reaching the detector through the aperture increases with the magnetic field. The agreement between Eq. (5.13) and the EPSILON calculation is good, improving with increasing magnetic field. This is because the analytic approximation of ϵ improves with an increasing B field because the error from the averaging of S decreases as ρ is reduced.

5.2.3 Uncertainty

The uncertainty in the efficiency calculation stems from the uncertainty in the fusion source profile, the error introduced from the uncertainty in the poloidal magnetic field, and the uncertainties in the dimensions/location of the aperture of the CFP spectrometer. These are determined separately by varying the assumed source profile, the plasma current, and the different geometric factors of the aperture.

Source Profile

Since the CFP detection efficiency ϵ is a line integral of the fusion source function, or profile, along the proton's orbit, variation in the fusion source profile obviously affects the detection efficiency. The fusion source profile is modeled as a parabolic profile raised to some power α [Eq. (5.7)]. Typically, $\alpha = 8$ is used in orbit calculations to model the peakedness of the fusion source function at the center of the plasma. An α as low as 2 or 4 only approaches the realistic situation when the plasma current is low.
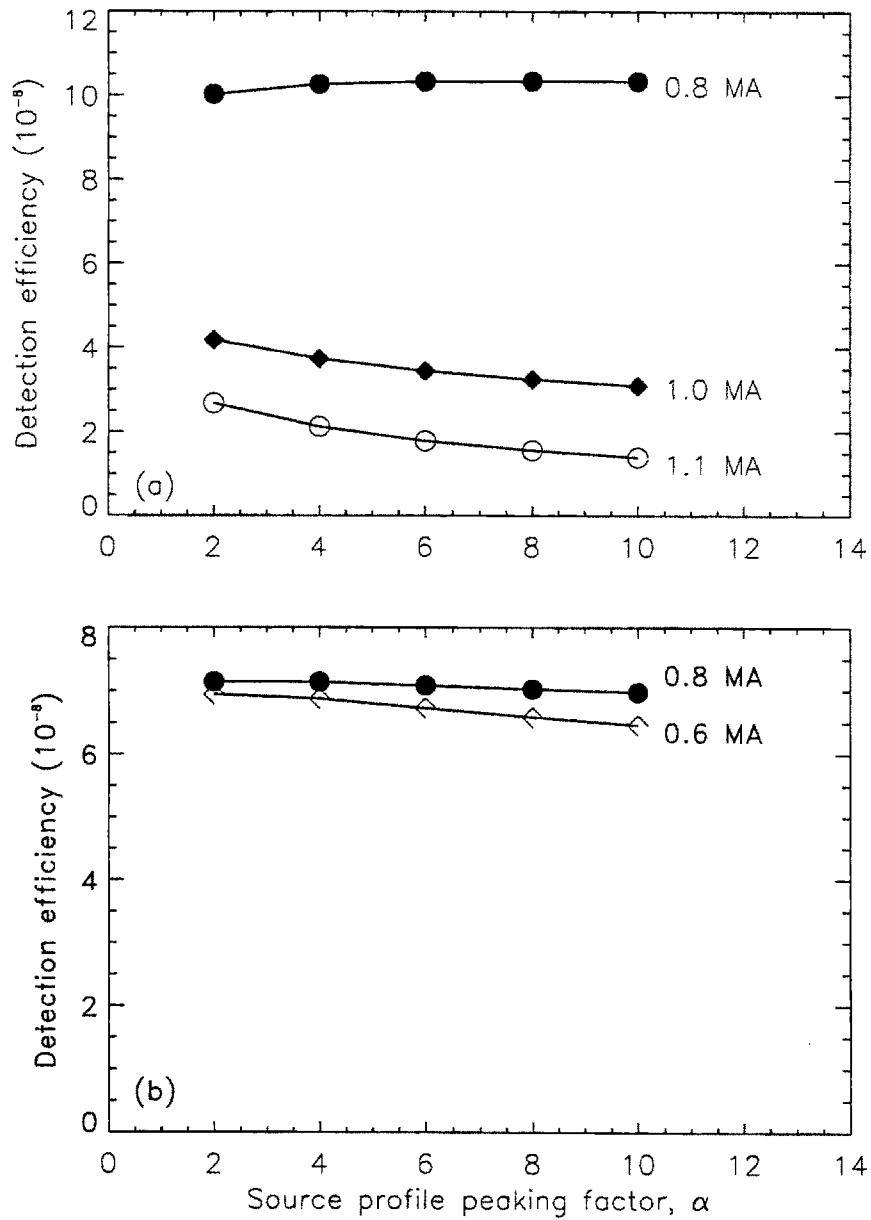
Figure 5.11: Effects of source profile on the detection efficiency for (a) run 960130 (refer to Figs. 6.9 and 6.10), (b) run 940603 (refer to Figs. 6.11 and 6.12). The conditions of these runs will be discussed in §6.3 on the current scan experiments.
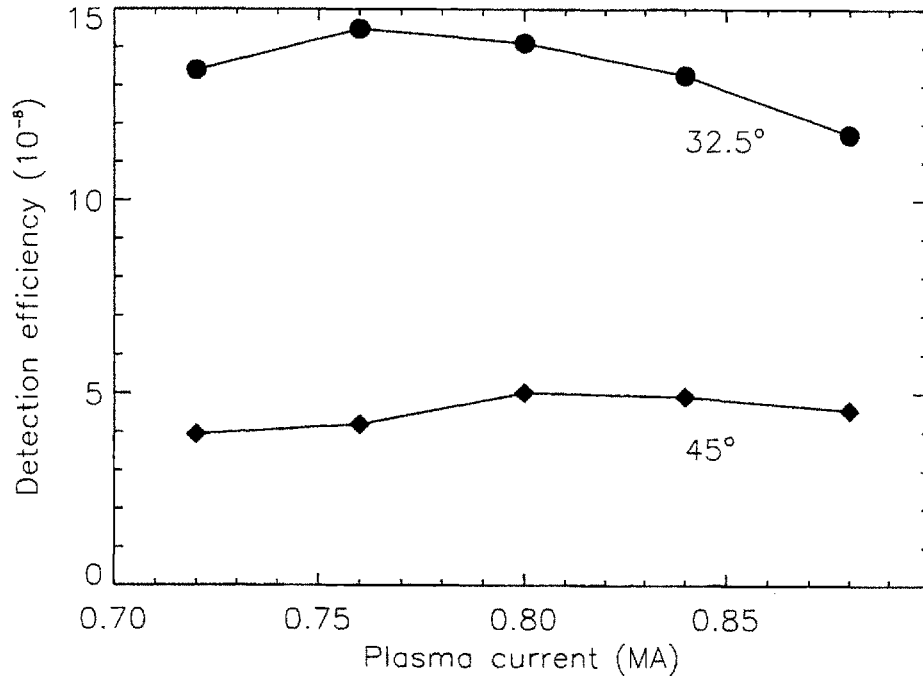
Figure 5.12: Effects of current uncertainty on the detection efficiency. The base case is for a plasma with $R_0 = 0.67$ m, $a = 0.21$ m, $B_\varphi = 5.3$ T, and $I_p = 0.8$ MA. Values for two different tilt angles are given.

Fig. 5.11 shows the sensitivity of the calculated efficiency to the power parameter, α, for different current conditions. The orbits in case (a) are banana-trapped orbits, while those in case (b) are passing orbits. (The specific cases presented will be discussed fully in §6.3 on the current scan experiments.) It is found that the sensitivity of the calculated ϵ to the parameter α is not high. When $\alpha = 8$, variation of α by ± 2, corresponding to assumed uncertainty in the ion temperature profile (see §5.1.3), results in about 5% variation in the efficiency calculation.

Plasma Current

A poloidal magnetic field B_θ is generated in Alcator C-Mod because the plasma sustains a toroidal current. The poloidal magnetic field, derivable from the current

profile, is an input to the orbit code and is calculated by the EFIT equilibrium code. An estimate of the uncertainty in B_θ from EFIT is σ_{B_θ}(Tesla) $\approx 0.035 \times I_p$(MA) [53]. This amounts to about 5% uncertainty in the values of B_θ. The uncertainty in the efficiency calculation introduced by the uncertainty in the poloidal magnetic field is determined through the varying of the plasma current.

The magnetic field used in these calculations (and also in the validity check calculations in §5.2.2) is calculated using the lowest-order approximation[1] (in an inverse-aspect ratio expansion) to the magnetic field in an axisymmetric toroidal geometry [54]:

$$B_\varphi = B_0 \frac{R_0}{R} \ , \qquad B_R = -B_\theta(r) \sin\theta \frac{R_0}{R} \ , \qquad B_Z = B_\theta(r) \cos\theta \frac{R_0}{R} \qquad (5.14)$$

where r and θ are the coordinates of concentric circular surfaces:

$$r = \sqrt{z^2 + (R - R_0)^2} \ , \qquad \sin\theta = \frac{z}{r} \ . \qquad (5.15)$$

The poloidal field B_θ is approximated by the field produced by a longitudinal current $j \propto [1 - (r/a)^2]^\beta$ in a cylinder, according to Ampere's Law:

$$B_\theta = \frac{\mu_0 I_p}{2\pi \ r}\{1 - [1 - (r/a)^2]^{\beta+1}\}. \qquad (5.16)$$

when $r \leqslant a$. When $r \geqslant a$, B_θ is assumed to fall off inversely with r.

The base case is for a plasma with $R_0 = 0.67$ m, $a = 0.21$ m, $B_\varphi = 5.3$ T, and $I_p = 0.8$ MA. Variation of I_p of up to $\pm 10\%$ is allowed. The effects of current uncertainty about the base case on the detection efficiency are shown in Fig. 5.12. Values for tilt angles of $32.5°$ and $45°$ are given. For any I_p variation (analogous to variation of B_θ) of 5%, the efficiency varies by $\lesssim 16\%$. For a 10% variation, the efficiency variation

---

[1] Note that this is a crude approximation because a) the model magnetic field is not divergenceless, b) the aspect ratio $r/R \sim 0.3$ in Alcator C-Mod is not a small expansion parameter, and c) a circular plasma is assumed.

is still $\lesssim 21\%$. (Note, though, that drastic changes in the efficiency could arise from a small change in I_p when the CFP orbit becomes obstructed by vacuum structure in one of the cases.) To be conservative, we assume the higher value of 21% as the uncertainty due to the error in B_θ.

Overall Uncertainty

The uncertainties related to the physical dimensions/location of the aperture of the spectrometer has been studied in a manner similar to the other sensitivity studies. In order of increasing importance, the different factors include the aperture cup/plate thickness, the area of the aperture, the physical location (R, Z) of the aperture, and the tilt angle of the aperture cup (which is directly related to the pitch angle of incoming protons). An upper bound of about 20% uncertainty can be attributed to these physical factors. As a result, the overall uncertainty of ϵ is: $\sqrt{0.05^2 + 0.21^2 + 0.20^2} = 29\%$.

5.3 Prompt Loss Studies

If the trajectory of a charged fusion product intersects the wall before it completes a full poloidal orbit, it is lost to the wall. Such a loss mechanism is referred to as prompt loss. (In practice, this also includes losses due to impact upon any structure inside the vessel, such as a diagnostic probe or the RF antenna.) Built on the same charged particle orbit algorithm, PROMPT has been written for the studying of the distribution of promptly lost charged fusion products in the Alcator C-Mod vessel. A sufficiently large ensemble of charged fusion products are allowed to be born inside the vessel. Their trajectories are followed forward in time until they either are promptly lost to the wall or are confined classically (first orbit fails to intersect the wall). The prompt-loss fraction is statistically deduced from such results.

Each particle's initial velocity is set at random. Its initial position is generated in a Monte-Carlo fashion as well, but weighted according to the fusion product source

Starting and Ending Points of Lost Particles
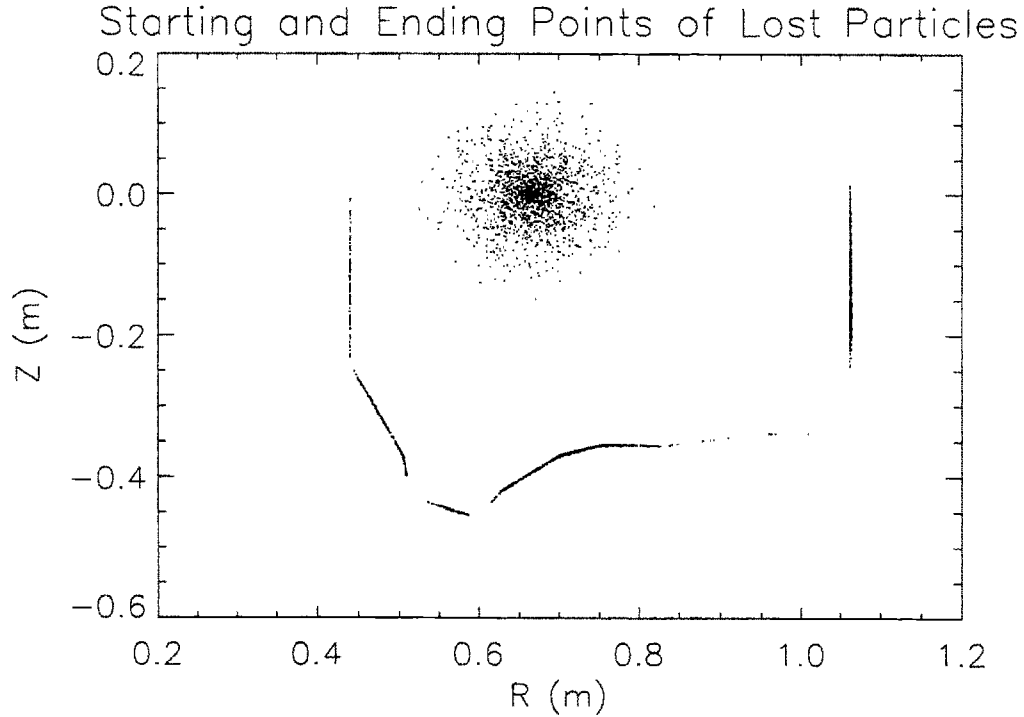
Figure 5.13: The initial and final positions of promptly lost 3 MeV
protons are shown. The ∇B drift is down in this case,
and to no surprise, no particle is lost to the first wall
in the upper portion of the vessel. Note also that the
helical nature of the orbits make it a rare event for a
proton to be lost to points on the first wall that are in
the vicinity of any outward corners.

function $S(r)$ given by Eq. (5.7). Figure 5.13 shows the initial and final positions
of all subsequently lost 3 MeV protons in a simulation. The toroidal field on axis
is $B_\varphi = 5.3$ T and the plasma current is $I_p = 0.82$ MA. As expected, no particle is
lost to the upper portion of the machine as the ∇B drift direction is downward. The
prompt-loss fraction is calculated to be about 20%. A simulation run for 14.7 MeV
protons from D-^{3}He fusion yields a prompt-loss fraction as high as 86% under the
same conditions.

Figure 5.14 shows how the prompt-loss fraction converges as the number of 3 MeV
protons used in the simulation is augmented. Acceptable statistics for the simulation
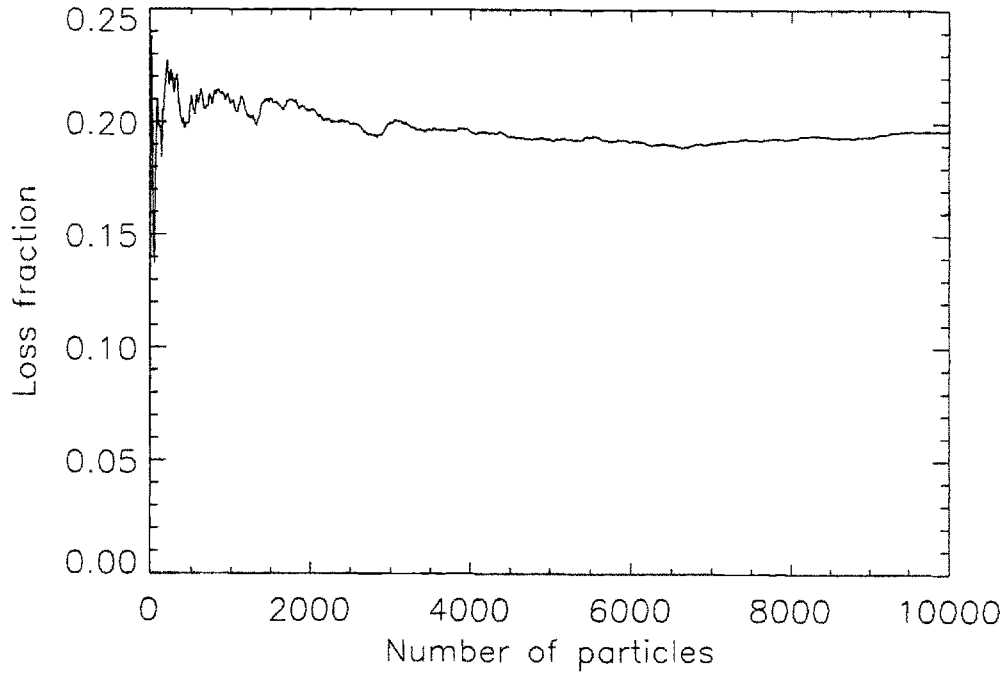
Figure 5.14: The prompt-loss fraction of this simulation converges as
the number of 3 MeV protons used in the simulation in-
creases. The toroidal field is $B_\varphi = 5.3$ T and the plasma
current is $I_p = 0.82$ MA.

($\pm$ 1% of the calculated prompt-loss fraction) are reached with an ensemble of 10^4 particles. Nonetheless, the simulation is expected to give results that are accurate only to about 10% due to error in the modeling of the vacuum vessel and the error in the finite timestep integration routine itself in the orbit calculation.

Figure 5.15 shows how the prompt-loss fraction scales with the plasma current. At a higher plasma current of, say, 1.17 MA and the same magnetic field as considered before, it is calculated that the prompt-loss fraction of 3 MeV protons has dropped to 12%. (As expected, the results for 1 MeV tritons are the same within the uncertainty of the Monte Carlo simulation.) Similarly, the prompt-loss fraction of 14.7 MeV protons has dropped to 63% at 1.17 MA.

A simple axisymmetric, neoclassical confinement model predicts that all MeV
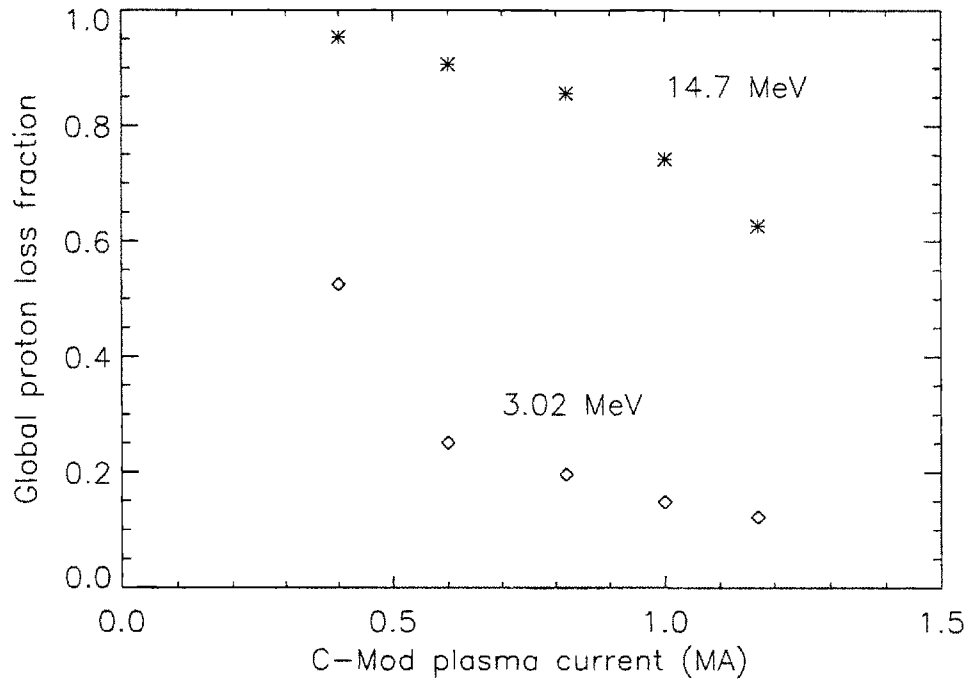
Figure 5.15: The prompt-loss fraction decreases with increasing plasma current. The behavior is predicted according to a simple axisymmetric, neoclassical confinement model [55,56].

charged particles which are confined on their first orbit will stay confined until they become thermalized, since energy drag dominates pitch angle scattering during the thermalization process [55,56]. Therefore, loss of charged fusion products should be significant when the typical banana width Δ becomes comparable to or larger than about half the minor radius [Eq. (1.8)]. This qualitatively explains the results in Fig. 5.15. A higher prompt-loss fraction can be expected for a larger Δ, with everything else fixed. Between the 3 MeV D-D proton and the 14.7 MeV D-^{3}He proton, the latter has a larger gyroradius, and thus a larger Δ. Therefore, the prompt-loss fraction for 14.7 MeV protons is considerably and consistently higher. For each species of protons, raising the plasma current lowers the safety factor q, and thus, Δ. Therefore, the prompt-loss fraction is seen to fall with increasing plasma current.

Chapter 6

Fusion Reaction Rate Measurements

The charged fusion product (CFP) spectrometer was first operating in the Alcator C-Mod tokamak during the spring campaign of 1994. The spectrometer offers independent measurements of Alcator C-Mod's fusion rate, which are summarized in the present chapter. Different scenarios are presented to positively identify the detection of D-D protons and tritons. The fusion rate measurements are also compared to those measured with the neutron diagnostic system. Finally, the plasma current dependence of the detected D-D proton flux is presented. The data are shown to compare well with the modelled behavior based on orbit calculations using EPSILON (refer to Chapter 5).

6.1   Charged Fusion Products from Alcator C-Mod

6.1.1   Spectral Time Evolution

Figure 6.1 shows a number of spectra taken during different 100 ms time intervals of an ohmic discharge (discharge 951130008) in Alcator C-Mod ($B_\varphi = 5.3$ T, $I_p = 820$ kA). In-situ energy calibration is achieved via the α sources within the CFP spectrometer
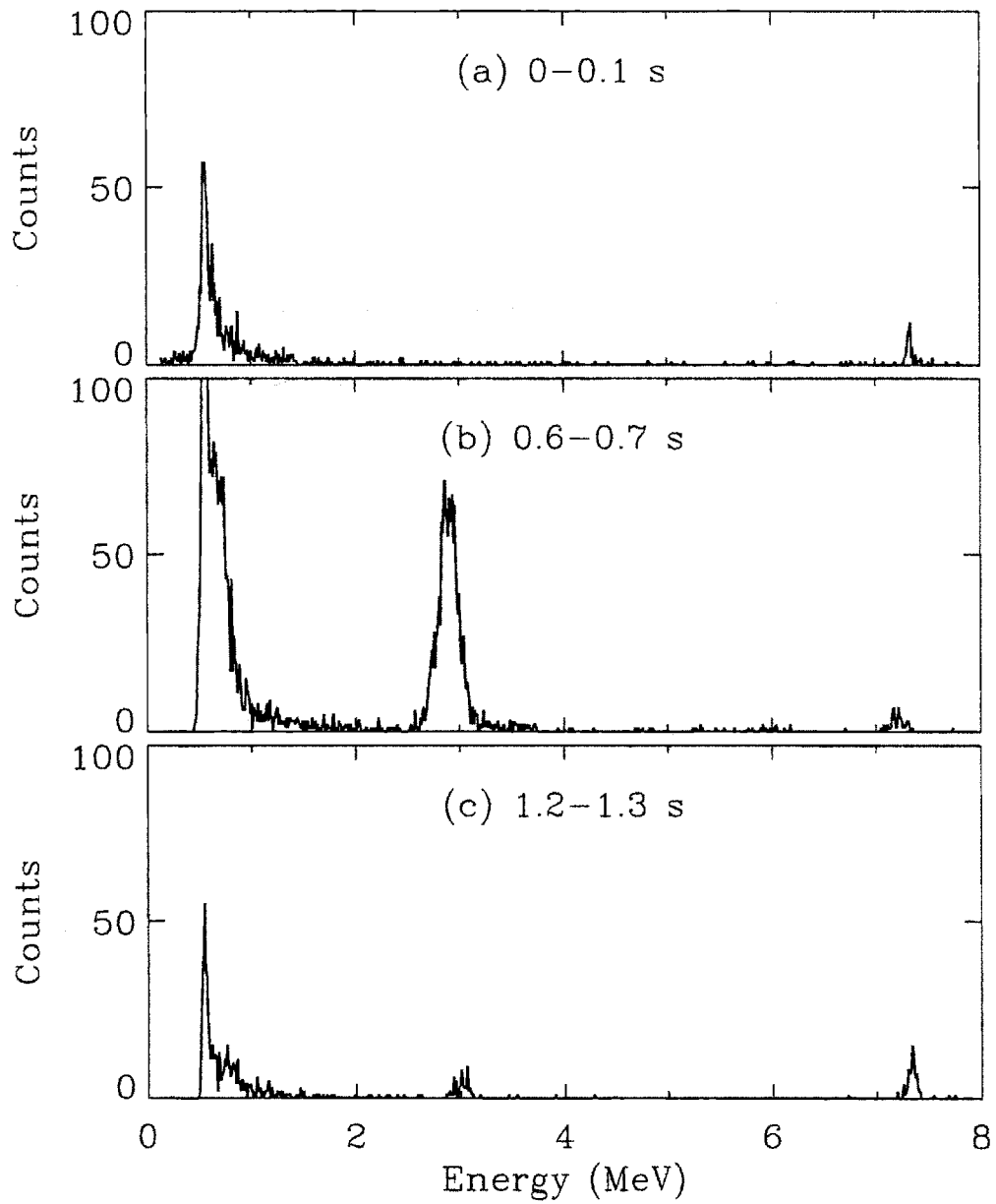
Figure 6.1: CFP spectra during different phases of an ohmic discharge (Shot 951130008, $B_\varphi = 5.3$ T, $I_p = 820$ kA): (a) startup phase, 0–0.1 s; (b) current flattop phase, 0.6–0.7 s; (c) current rampdown phase, 1.2–1.3 s.
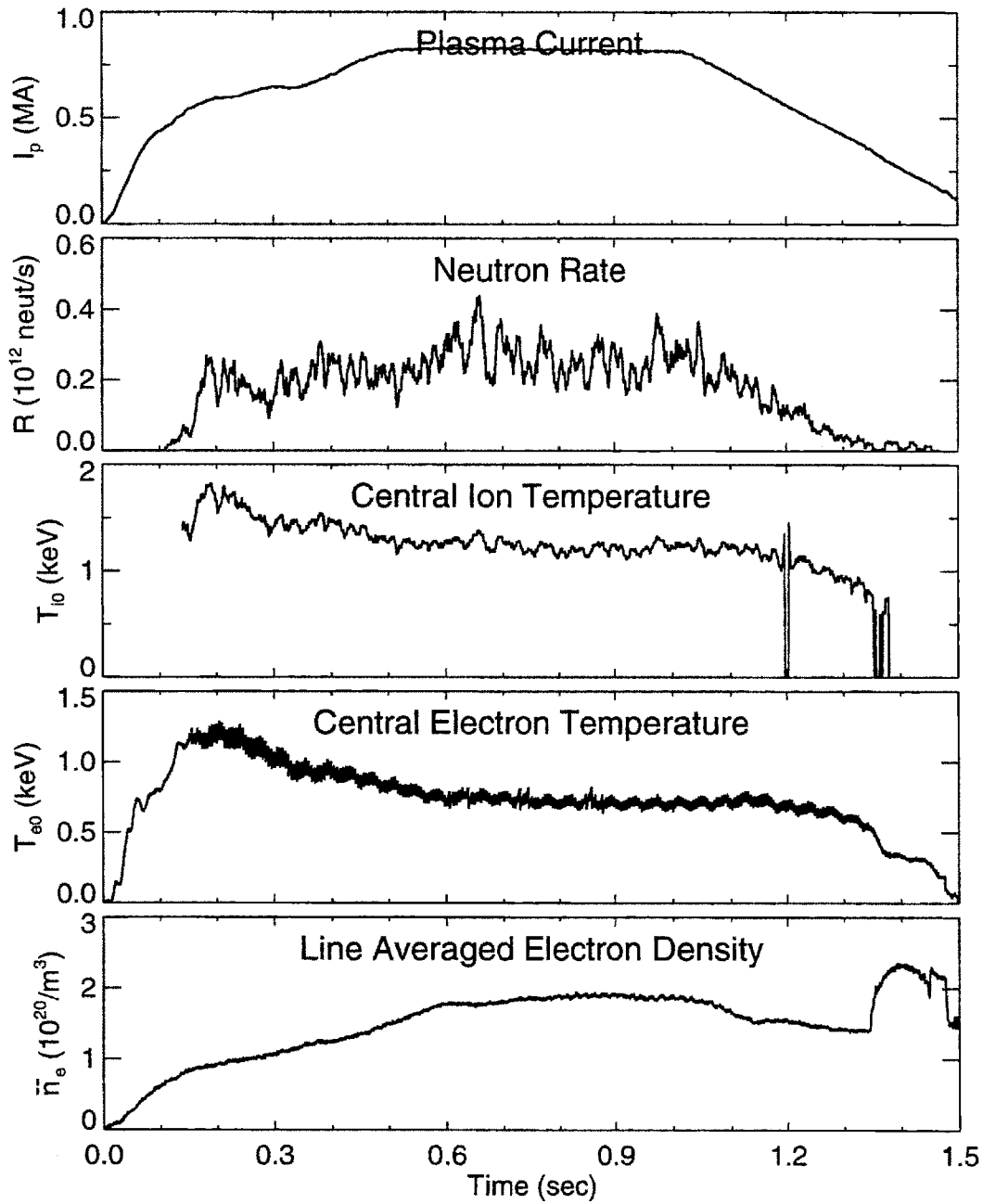
Figure 6.2: Time history of some plasma parameters for the ohmic discharge shown in Fig. 6.1.

(see Chapter 4). The time history of some plasma parameters characterizing the discharge is shown in Fig. 6.2. During the first 100 ms of the discharge, the plasma was just taking shape and the fusion rate was too small for any CFPs to be detected. The low-energy background counts in the spectrum are due to neutron-capture γ rays, fusion neutrons, and hard x rays from runaway electrons as discussed in Chapter 8. The counts about 7 MeV were generated by the pulser.

The plasma current achieved the "flattop" level of 820 kA at around 0.5 s. and was held constant through 1.0 s. The CFP spectrum in Fig. 6.1(b) was taken during this phase. A D-D proton peak is clearly visible at around 3 MeV [see Eq. (1.1)]. The energy of the protons was lowered to about 2.95 MeV because they lost energy while traversing a 3 μm aluminum foil that covered the aperture. Two other features are also visible in this spectrum. The added structure on the low-energy background ($\sim$ 0.7 MeV) is believed to be due to D-D tritons. The energy is consistent with energy loss of 1 MeV tritons (about 265 keV) in the 3 μm aluminum foil at the aperture. However, the low-energy background that persisted throughout the discharge obscures the energy peak and makes the identification difficult. Secondly, the pulser peak has visibly been broadened and its mean "energy" has also been reduced. In the current rampdown phase, the fusion rate gradually dropped as the ion temperature decreased. The CFP spectrum in Fig. 6.1(c) shows few D-D proton counts, a combined result of both a reduced fusion rate (by 4) and a drop in the proton detection efficiency (by more than 10).

6.1.2   Effects of Ranging Foils

One way to be convinced that the structures in Fig. 6.1 are indeed due to D-D protons is to change the thickness of the aluminum foil covering the entrance aperture to the spectrometer. Installed in the CFP spectrometer are apertures with aluminum foils that are 3, 20, and 100 μm thick. The spectrum used in the discussion in §6.1.1 was collected with a 3 μm aluminum foil. If the chosen aluminum foil thickness is 20

108
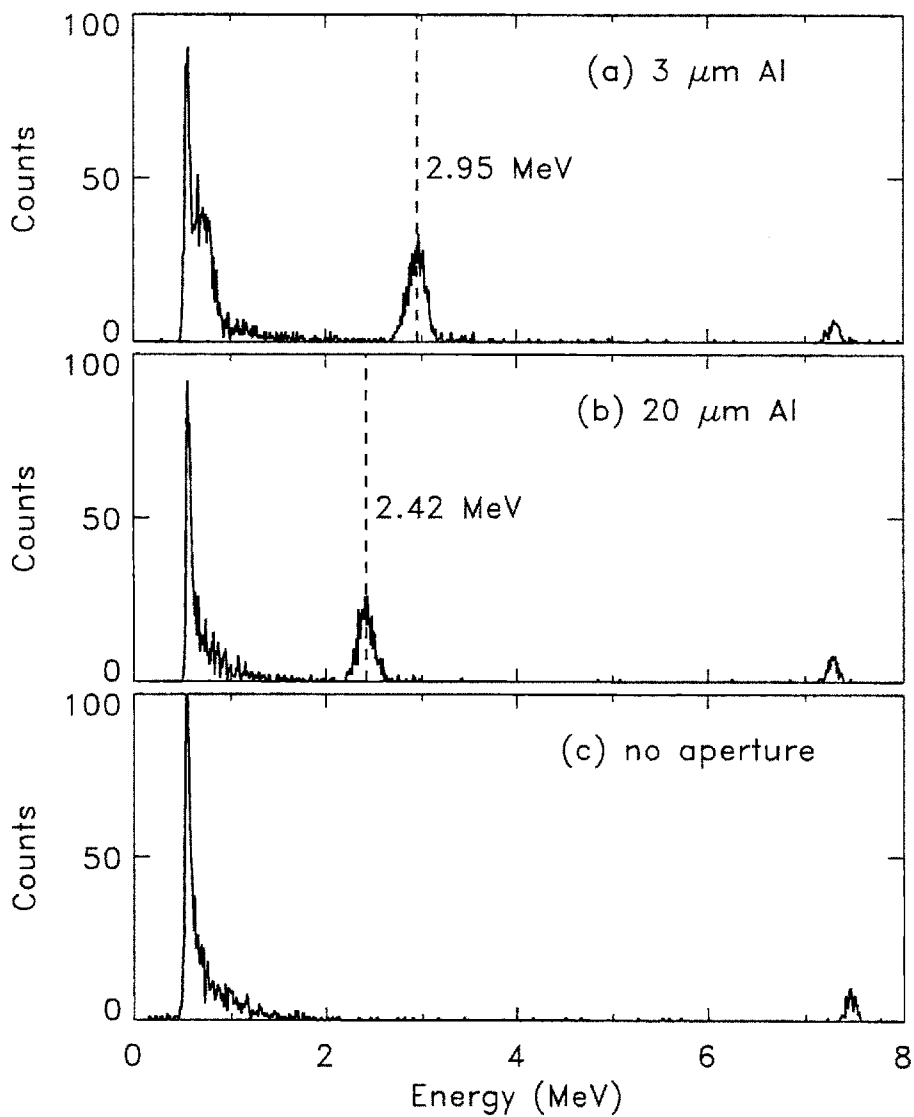
Figure 6.3: CFP spectral downshift due to ranging foil. (a) For shot 951130008 (3 μm aluminum foil), the D-D proton peak is centered about 2.95 MeV, while the triton peak is at ~ 0.7 MeV. (b) For shot 951117001 (20 μm aluminum foil), the D-D proton peak has shifted down to 2.42 MeV, and the triton peak is absent. (c) For shot 951206005 (3.2 mm stainless steel), no CFP is detected, as expected. The pulser position for this run had been changed.

μm, a 3.02 MeV proton is expected to emerge with about 2.53 MeV. The amount of energy loss, however, is dependent on the particle species. If the 3 MeV particle "in question" were not a proton, the energy loss would be different because of a different stopping power relation. In particular, if it were a ^{3}He particle, α particle or any other more massive species with the same energy, it would not be able to penetrate the 20 μm foil. Tabulated in Table 6.1 is a list of light particles, their ranges in aluminum, and their energies after traversing 3 μm and 20 μm aluminum [35], assuming they all have initial energies of 3.02 MeV.

Particle	Range in Al (μm)	Energy (MeV) after 3 μm Al	Energy (MeV) after 20 μm Al
^{1}H	91	2.95	2.53
^{2}H	53.2	2.91	2.22
^{3}H	43.3	2.88	1.97
^{3}He	11.8	2.42	–
^{4}He	10.9	2.32	–

Table 6.1: List of 3.02 MeV particles, their ranges in aluminum, and their energies after traversing 3 μm and 20 μm Al [35].

CFP spectra collected during similar deuterium plasma runs but with different aluminum foils covering the aperture to the spectrometer are shown in Fig. 6.3. Figure 6.3(a) is for the case of a 3 μm thick foil, while Fig. 6.3(b) is for the case of a 20 μm thick foil. Also included is a third run, shown in Fig. 6.3(c) where the aperture was covered with 3.2 mm of stainless steel. (In reality, this was achieved just by positioning the 3.2 mm thick stainless steel aperture cup to allow no aperture.) In all three runs, $B_\varphi = 5.3$ T, $I_p = 820$ kA. Switching from the thinner to the thicker aluminum foil, the peak that was at 2.95 MeV is seen to have downshifted to about 2.42 MeV. The peak that was at about 0.7 MeV has disappeared altogether, giving way to the low-energy background. With the stainless steel, no CFPs are detected. (If an aperture of 1 mm × 1 mm were present, roughly 1800 protons and 1800 tritons would have been registered in this spectrum.) The overall results prove that indeed the structures in the spectra are D-D protons and tritons.
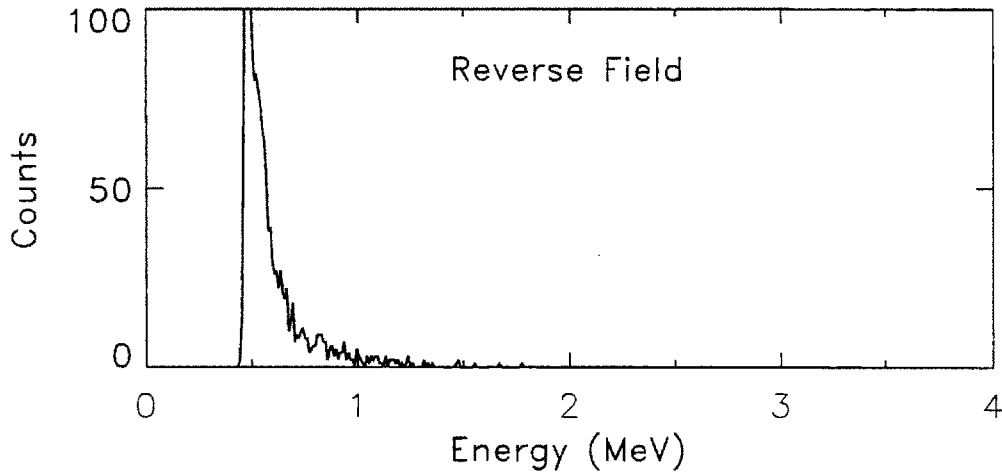
Figure 6.4: CFP spectrum (integrated over 100 ms) during reverse field operation (Shot 950407010, $B_\varphi = 5.3$ T, $I_p = 820$ kA). No CFPs were detected because the ∇B drift is downward. Note that the pulser signal was not available on this day.

6.1.3 Reverse Field Operation

When Alcator C-Mod was operated in a reverse field configuration such that the ∇B drift direction was upward,[1] the proton and triton peaks disappeared, as illustrated in Fig. 6.4. Whereas the CFP spectrometer was located 25.8 cm below Alcator C-Mod's midplane, unconfined CFPs making impact on the vessel and other structures were expected to do so in the upper half of the machine. (This is the direct opposite to the downward ∇B drift scenario depicted in Fig. 5.13.) Even confined CFPs were not expected to be intercepted by the CFP detector because of the relative positions of the aperture and the detector.

---

[1] When both the toroidal field and the plasma current are in the clockwise direction when viewing the machine from above it, the ∇B drift is downward. In the reverse field configuration, both the directions of the field and the current are reversed to give an upward ∇B drift. The current and field directions are kept the same because the field helicity has to stay constant to match the designed slant of the antennae faraday shields and the molybdenum first wall tile bevelling.

6.2 Fusion Rate

With the CFP spectrometer, independent measurements of the fusion rate can be made and compared with fusion rate measurements performed with the neutron diagnostic system. These measurements are presented in two formats. The single channel analyzer (SCA) is operated to measure signal pulses from the CFP spectrometer that correspond to events with energies between 2 MeV and about 6 MeV. These are interpreted to be D-D proton signals. The sampling rate of the SCA is set typically at every 2 ms. However, simply using the SCA to count pulses may not always give an accurate account of the D-D protons. First, there is always a low-energy background in the spectrum. This background, which is not due to D-D protons, can have counts extending to above the 2 MeV level. Secondly, it has been observed that at certain high count rate situations that the D-D proton peak may downshift in energy and broaden such that counts may fall below the 2 MeV level. These and the related issues will be addressed in Chapter 8.

A more reliable method of measuring the fusion rate relies on the multichannel analyzer (MCA). By examining a calibrated energy spectrum directly, the D-D protons detected as a function of time can be accurately accounted for. The spectrum usually contains 1024 channels for the purpose of good energy resolution for ion temperature measurements (discussed in Chapter 7). This limits the number of spectra to 16, and the spectra are collected every 100 ms to cover the entire length of a typical Alcator C-Mod discharge.

6.2.1 SCA Fusion Rate Time History

Figure 6.5(a) shows two independent measurements of the fusion rate as a function of time for discharge 950131003. The flattop of the discharge lasted from 0.5 s to 1.0 s, during which $B_\varphi = 5.3$ T and $I_p = 820$ kA. The solid trace is the fusion rate from the detection of D-D protons by the CFP spectrometer, while the dotted trace is from neutron measurements by the neutron diagnostic system. To get the
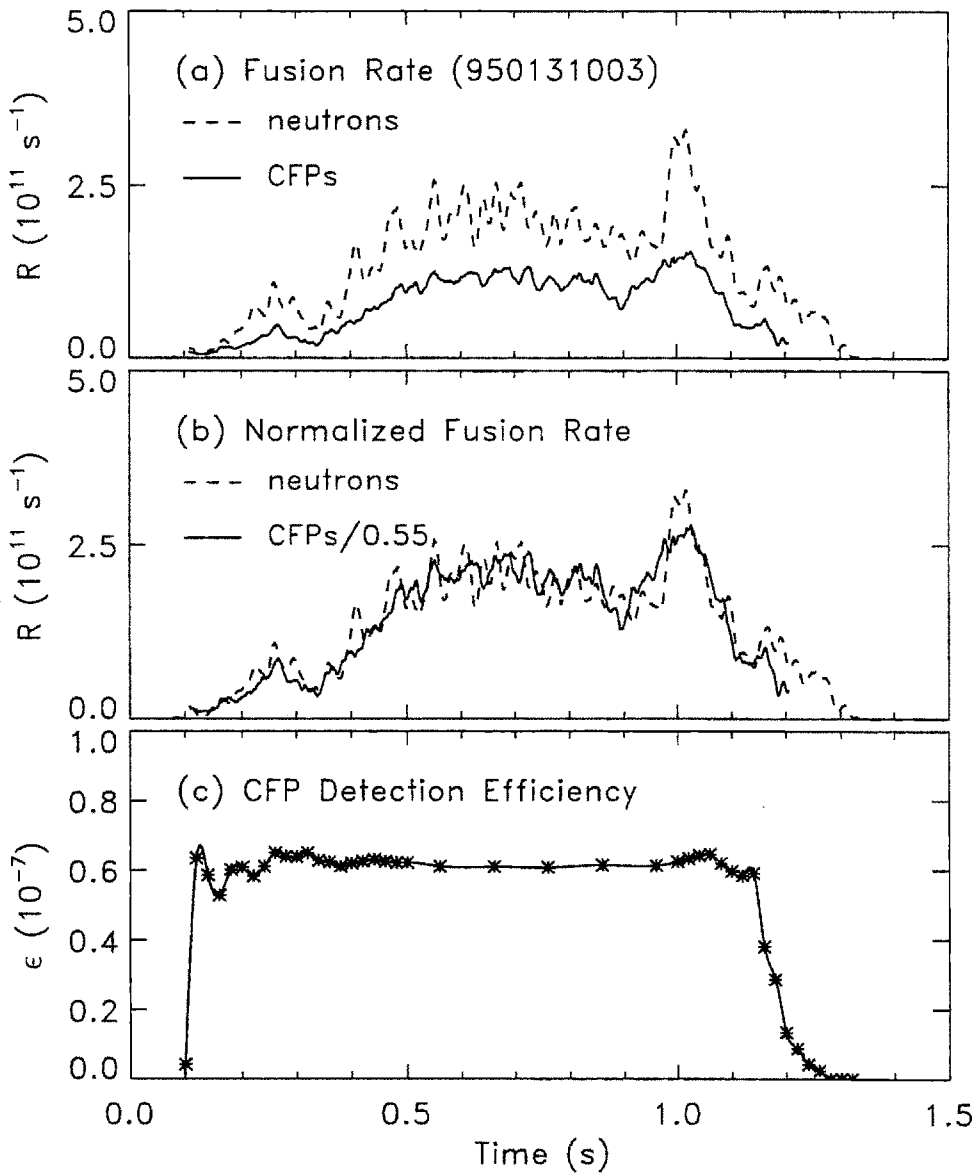
Figure 6.5: The fusion rate as predicted by the D-D proton signal (processed by the SCA) is compared to fusion rate from the neutron diagnostics in (a) for shot 950131003 ($B_\varphi = 5.3$ T and $I_p = 820$ kA during flattop period between 0.5 s and 1.0 s). In (b), the proton-measured fusion rate has been divided by 0.55. The shapes compare quite well, suggesting a systematic difference of about 45%. Shown also is the calculated detection efficiency (c) as a function of time.

113
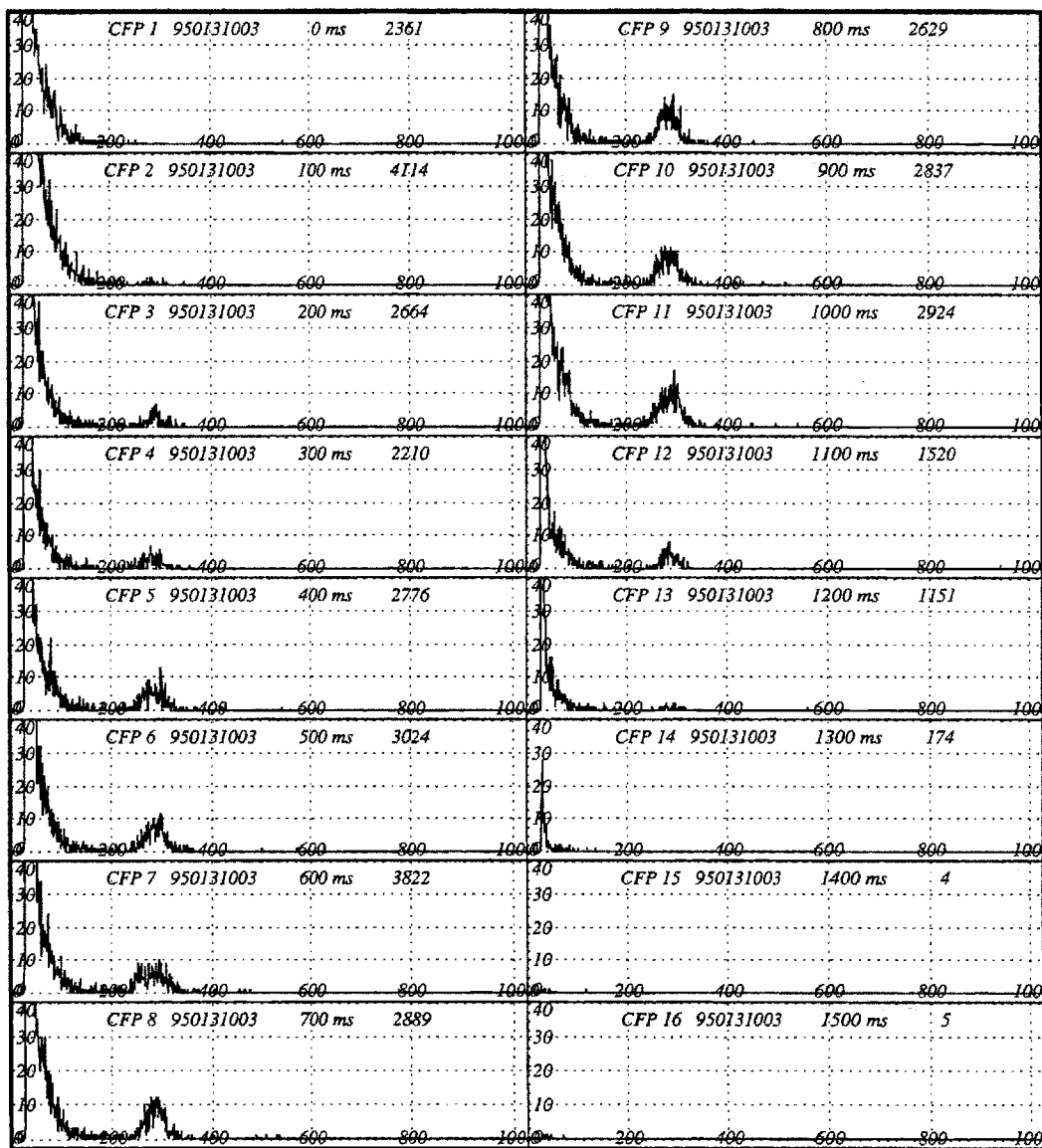
Figure 6.6: Successive spectra (each 100 ms long) collected by the CFP spectrometer during shot 950131003. The structure about channel 300 is the D-D proton peak and the calibration is roughly 10 keV/channel. At the top of each spectrum are listed the spectrum number, the shot number, the starting time of integration, and the overall number of counts. No pulser was available at that time.

114

solid trace, the SCA signal, representing counts of D-D protons, is divided by the proton detection efficiency which is shown in Fig. 6.5(c), divided by the length of the sampling time interval, and corrected for the effects of dead time (discussed in §4.5). As described in Chapter 5, the proton detection efficiency is computed with the orbit code EPSILON, given the physical setup of the spectrometer (*i.e.*, detector aperture orientation and dimensions) and the instantaneous magnetic field geometry within the Alcator vacuum vessel. The field geometry is available as an output from the EFIT equilibrium code [21] every 20 ms throughout a plasma discharge. The corresponding spectra collected during this discharge is given in Fig. 6.6. The structure about channel 300 is the D-D proton peak and the calibration is roughly 10 keV/channel. Counts in the low-energy channels are due to γ rays, hard x rays, and D-D tritons (obscured by the photons).

From the time traces in Fig. 6.5(a), the fusion rate predicted from D-D protons is systematically lower by about 45%. One of the two contributing factors to the uncertainty in the fusion rate measurement is the error in the detection efficiency calculation. This has been determined in §5.2.3 to be about 29%. The other factor has to do with the error in the counting of protons by the electronics. In the present case, the fusion rate is presented with approximately 10% uncertainty during the flattop portion of the discharge. The uncertainty introduced by the dead time correction procedure is about 5% at times when the total count rate is at its maximum. They, therefore, combine to give about 11% uncertainty in the count rate. Therefore, the overall uncertainty of the fusion rate measurement comes to only around 31% and does not fully explain the discrepancy between the two measurements.

To compare just the relative shapes of the two traces, Fig. 6.5(b) repeats the comparison in Fig. 6.5(a), but with the proton trace divided by a factor of 0.55. There is a general agreement in the shape of the two time histories. This qualitative agreement between the proton fusion rate and the neutron rate is typical of many discharges. Such agreement is expected for proton losses dominated by prompt loss
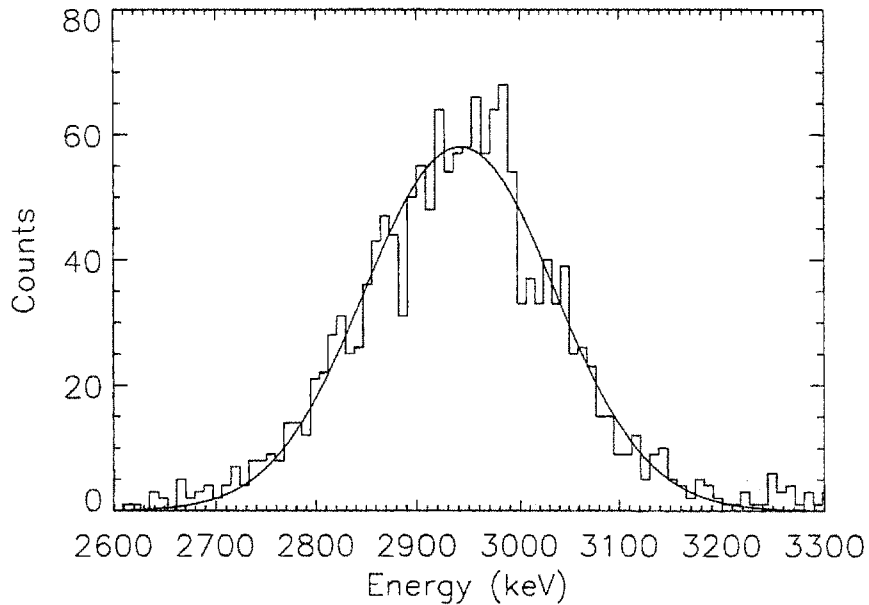
Figure 6.7: Energy spectrum of 3 MeV protons here shown fitted to a gaussian profile.

because the prompt-loss time of a typical 3 MeV proton in Alcator C-Mod is only $\sim$ 1 μs (it is 3 times longer for the 1 MeV triton).

6.2.2 Fusion Rate from Energy Spectrum

Using data from the collected energy spectra from a variety of discharges, the fusion rate over 100 ms time intervals can be deduced. The data are from D-D proton spectral peaks as the D-D triton peaks are always obscured by the low-energy background, as demonstrated in Fig. 6.1(b). Energy calibration of the spectrum facilitates the identification of the D-D proton peak. Each peak is fitted to a gaussian profile, with possible contributions from background counts removed. A fitted proton peak is shown in Fig. 6.7. The area under the peak is the number of protons detected. The fusion rate is calculated by applying the dead time compensation (see §4.5) and dividing by the average proton detection efficiency of the period and by 100 ms.
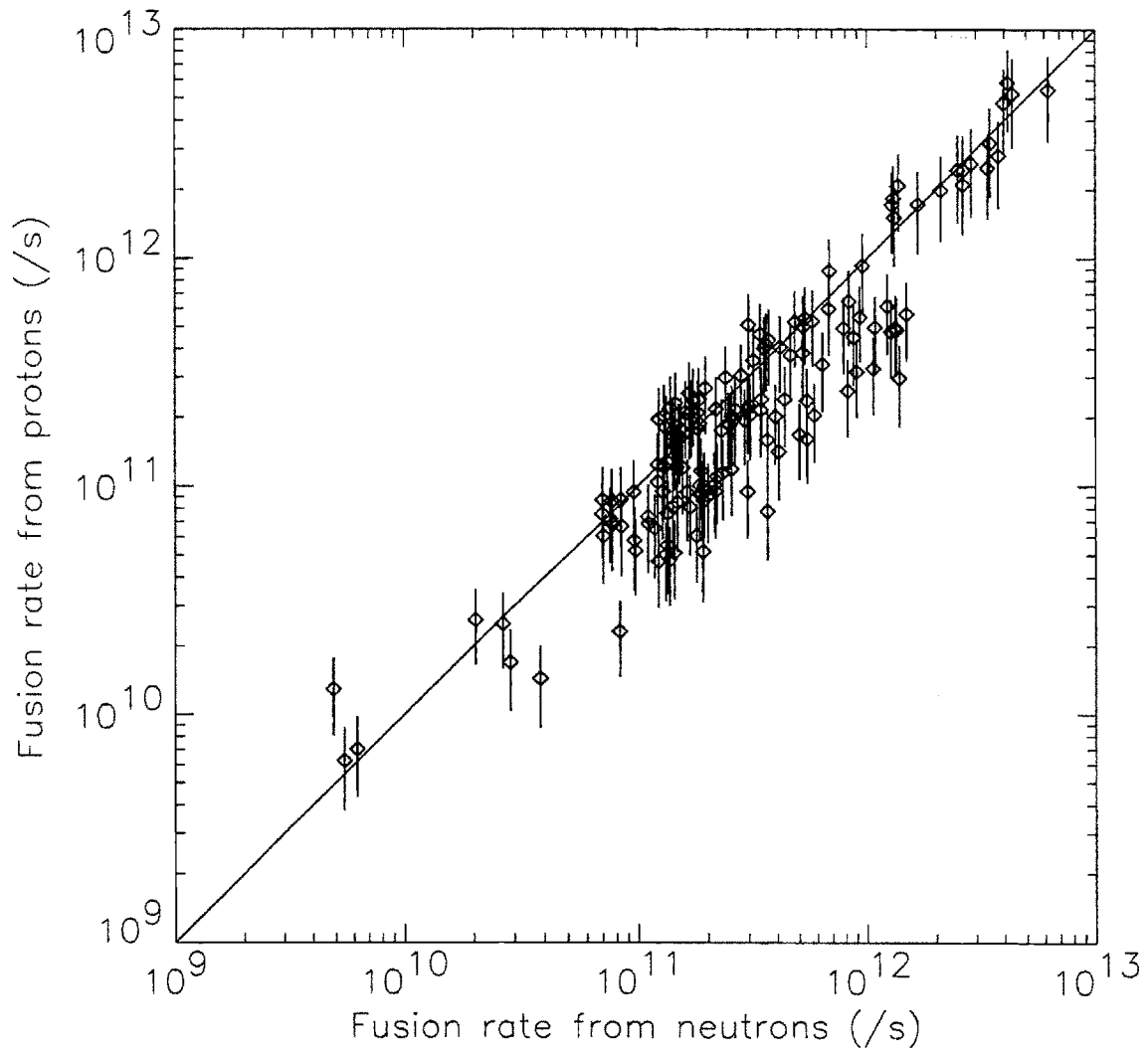
Figure 6.8: Comparison of global fusion rate measurements measured with D-D protons and from D-D neutrons. Each is a 100 ms sampling of the fusion rate.

Figure 6.8 shows a comparison between fusion rate measurements made with D-D proton detection and fusion rate measurements based on the neutron diagnostic, for fusion rates ranging over 3 decades. A data point lying close to the diagonal represents good agreement. On many shots the agreement is good to within the uncertainty of the measurement, although there is a clear indication for the CFP diagnostic to underestimate the fusion rate at times. The error bars included represent the uncertainties (as discussed in the previous section) that can be accounted for. For about 40% of the data points shown, the discrepancy between the proton-measured fusion rate and the neutron-measured fusion rate cannot be fully accounted for by the known uncertainties.

6.3 Current Scan

In Chapter 5, the global prompt-loss fraction of D-D protons is shown to decrease with increasing plasma current. This dependence can be expected in a current scan experiment if all lost protons are collected. However, the single detector housed in the CFP spectrometer assembly provides only a localized measurement of the proton flux as a function of the plasma current. Therefore, any current scan data cannot be compared directly to the simulation results of the current dependence of global prompt losses. Instead, the trajectories of the protons that reach the spectrometer, and how they vary with the plasma current (or the proton detection efficiency *vs.* plasma current) need to be examined.

Two sets of data are presented here on the current dependence studies. Figure 6.9 shows data from a current scan experiment (run 960130) for 0.8–1.1 MA, while the toroidal field was constant at 5.3 T. For each plasma current, the data come from both ohmically-heated and ICRF-heated deuterium plasmas. The entrance aperture had dimensions of 1 mm × 1 mm, and was characterized by a tilt angle of 32.5° and a gyro angle of 80°. (Refer to Fig. 4.4 in §4.1.) Plotted as well is the calculated proton detection efficiency as a function of the plasma current (solid trace). Reasonable
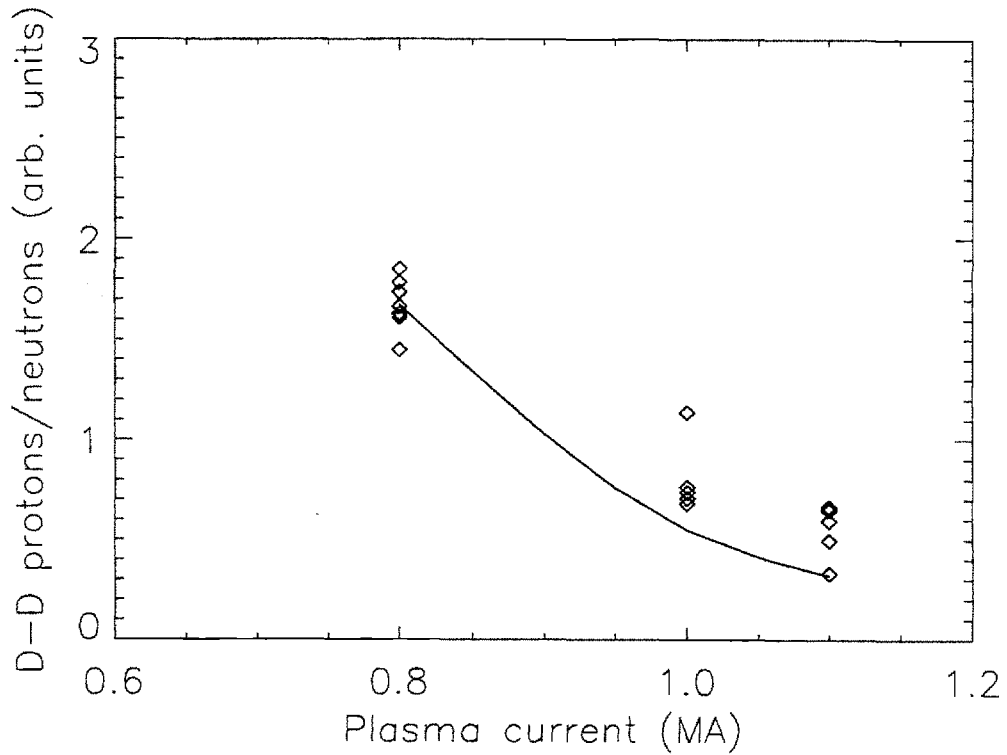
Figure 6.9: D-D proton loss (normalized to the neutron rate) versus plasma current during run 960130. The solid curve shows the relative normalized proton flux calculated using the code EPSILON.

agreement between the data set and the calculated efficiency is found.

Figure 6.10 gives a pictorial explanation of the current dependence observed in this experiment. The orbit shown in each case corresponds to one taken by protons that travel through the center of the selected aperture, which stayed fixed throughout the whole run. For the aperture used and the range of the plasma current scanned during the run, the average proton detected in each of the three cases is banana-trapped. At the same toroidal magnetic field, the pitch angle [Eq. (5.9)] of an incoming proton going through a fixed aperture increases with increasing plasma current. This affects the trajectories of incoming protons and, in particular, the midplane-crossing point of the trajectories.
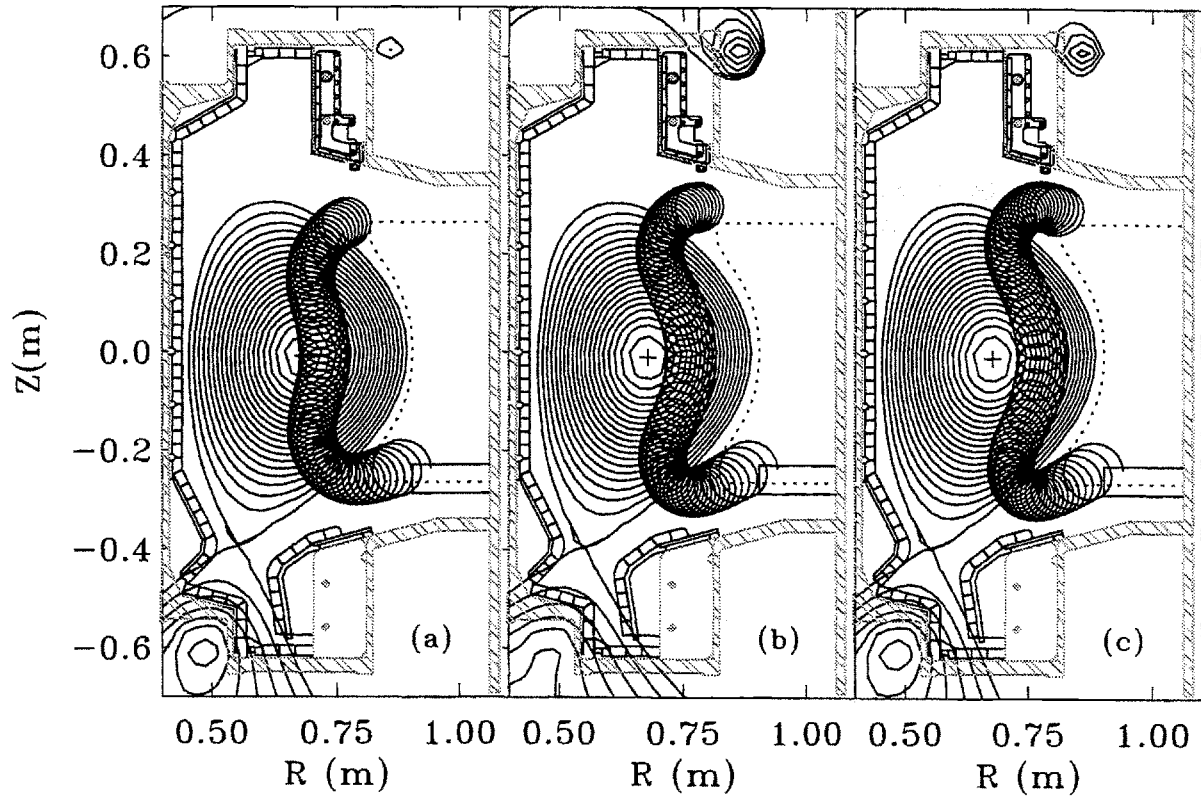
Figure 6.10: Average orbits of protons reaching the spectrometer
through a fixed aperture during run 960130 are shown
for various levels of the plasma current: (a) 0.8 MA, (b)
1.0 MA, and (c) 1.1 MA. At the 0.8 MA, protons reach-
ing the spectrometer tend to originate from closer to the
plasma center; at 1.1 MA, orbits of protons reaching the
spectrometer come from farther out, where the fusion
source strength is lower.
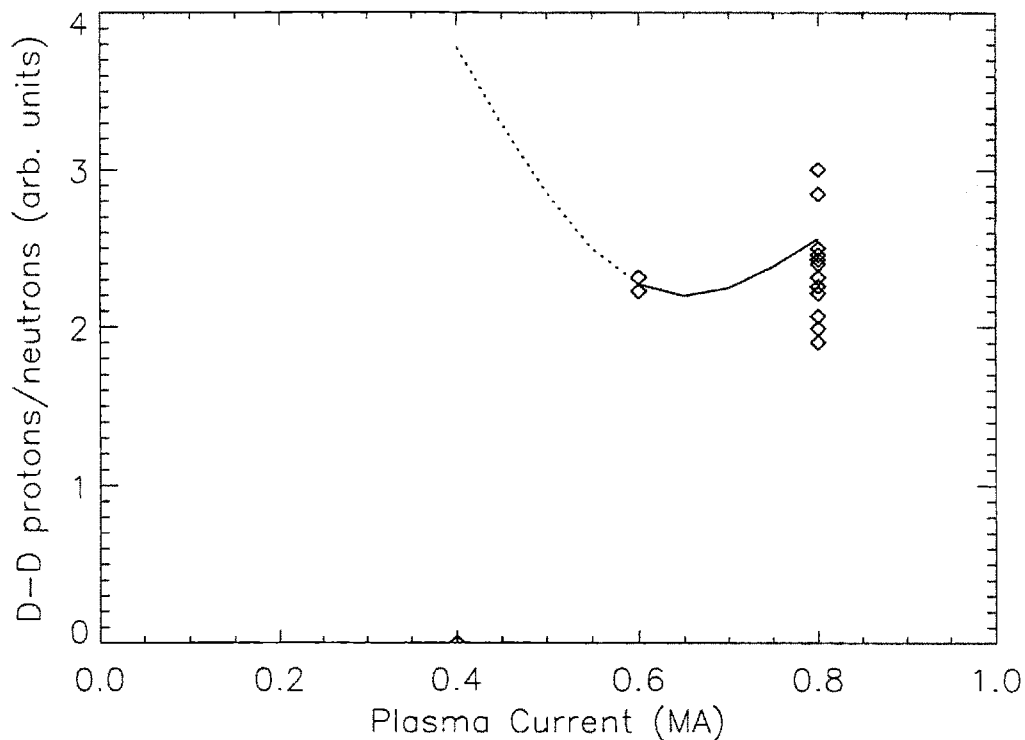
Figure 6.11: D-D proton loss (normalized to the neutron rate) versus plasma current during run 940603. The solid curve shows the relative normalized proton flux calculated using the code EPSILON. For $I_p = 0.4$ MA, the code does predict zero flux due to the presence of the RF limiters. The dotted portion is the calculated result assuming no RF limiter.

At the lower current of 0.8 MA, protons reaching the spectrometer tend to originate from closest to the plasma center. The midplane-crossing point of the proton trajectories shifts radially outward as the current rises. At 1.1 MA, the protons reaching the spectrometer have on average a larger pitch angle at a given major radius. The trajectories of such protons come generally from regions of the plasma further out from the center. Since the fusion source function is peaked at the plasma center, the flux of detected protons normalized to the same neutron rate should fall as the current is raised from 0.8 MA to 1.1 MA. This qualitatively agrees with our observation.

A second current scan experiment yields results summarized in Fig. 6.11. This data set was collected in run 940603, during which the toroidal field was again constant at 5.3 T, and the plasma current ranged from 0.4 to 0.8 MA. The deuterium plasma was heated only ohmically in this run. The size of the entrance aperture was 1 mm × 1 mm, and the tilt angle and gyro angle were 45° and 80°, respectively. The data show that the normalized proton flux was about the same when the plasma current ∼ 0.6–0.8 MA. However, at 0.4 MA essentially no proton was detected. Shown as well (solid trace) is the calculated proton detection efficiency as a function of the plasma current. The proton flux at 0.8 MA is expected to exceed that at 0.6 MA by 7%, while no protons can be expected when the current is at 0.4 MA. The agreement between the data and the prediction is clear. It is interesting, though, to see why the flux should drop when the plasma current is low.

Figure 6.12 shows the D-D proton orbits calculated for the three current conditions. The key factor turns out to be a combination of the local poloidal magnetic field and the choice of the aperture's tilt angle. A decreasing plasma current brings about a lowering of the local poloidal magnetic field and pitch angle, χ, for the path defined by the aperture. The parallel velocity, $v_\parallel$, of a proton that would go through this aperture increases. Table 6.2 lists the pitch angle, the normalized parallel velocity, and the normalized parallel energy of a proton passing through the aperture in the three current cases.

Current, I_p (MA)	0	0.4	0.6	0.8
Pitch angle, χ (deg)	45	50.2	52.2	53.9
$v_\parallel/v$	0.71	0.64	0.61	0.59
$E_\parallel/E$	0.50	0.41	0.38	0.35

Table 6.2: A tabulation of χ, $v_\parallel/v$, and $E_\parallel/E$ for the three current settings during run 940603. Also included is the case of zero current (pure toroidal magnetic field), for comparison.

Of the three cases, $v_\parallel$ is the highest (or the pitch angle is the lowest) at 0.4 MA because the corresponding B_θ is the smallest. In the case of 0.4 MA, the orbit code
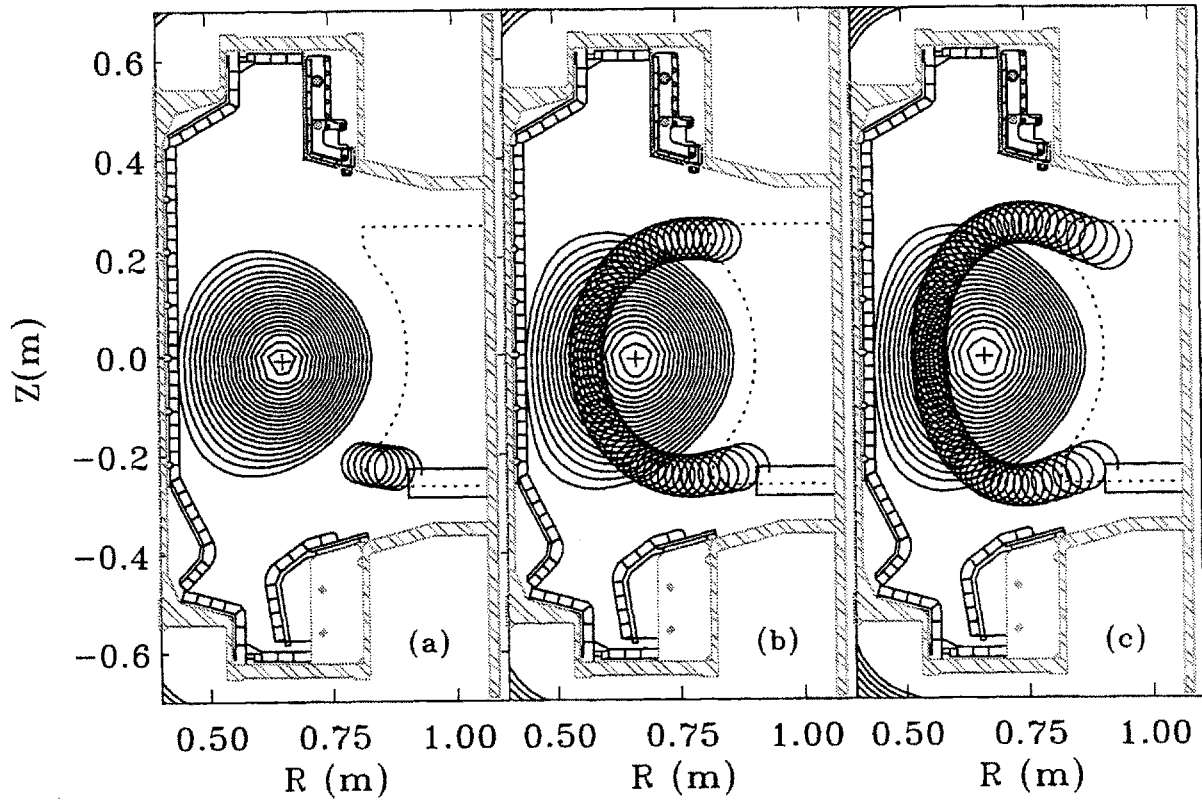
Figure 6.12: Average orbits of protons reaching the spectrometer through a fixed aperture during run 940603 are shown for various levels of the plasma current: (a) 0.4 MA, (b) 0.6 MA, and (c) 0.8 MA. In case (a), the time-reverse orbit terminates at the RF limiter, meaning no proton reaches the spectrometer. In cases (b) and (c), both orbits are passing orbits crossing the midplane at $R < R_{axis}$.

EPSILON traces the orbit backward in time to an RF limiter 90° toroidally away from the spectrometer without ever entering the plasma. This translates to having no proton from the plasma reaching the spectrometer at this current level, as the RF limiter at toroidally 90° away had blocked the aperture. The dotted trace in Fig. 6.11 shows what the relative expected proton flux should be as the current approaches 0.4 MA if the RF limiter were not present.

In the other cases, the "line" of sight was not obstructed. Because of the lower pitch angles (compared to the previous current scan experiment), both orbits were passing orbits crossing the midplane at $R < R_{axis}$. The orbit for the case of 0.6 MA seems to pass closer to the magnetic axis than that for 0.8 MA (see Fig. 6.12), implying a higher detection efficiency for the former case. However, because of the finite dimensions of the aperture and the integration over the entire orbit pathlength, calculations by EPSILON show that the detection efficiency at 0.8 MA was actually higher.

The good agreement between the observations in the two current scan experiments and the prediction based on orbit calculations using EPSILON is in support of prompt loss being the dominant loss mechanism of D-D protons. In addition, it also gives added confidence in the EPSILON code computation of the proton detection efficiency.

Chapter 7

Ion Temperature Diagnostic

As a fraction of the charged fusion products escapes the plasma through the prompt loss mechanism without any collisions, the energy spectrum of the charged fusion products are directly correlated to the energy distribution of the reacting deuteron ions. In particular, in a plasma of deuterium ions having an isotropic Maxwellian distribution, the energy spectrum of the charged fusion products (like 3 MeV protons and 1 MeV tritons) gives a direct measure of the ion (deuteron) temperature. The theory explaining this correlation has been developed by G. Lehner [57].

7.1 Fusion Reaction Rate

The nuclear reaction to be considered takes place in a two-particle system between ions A and B with resulting products C and D and a reaction energy Q:

$$A + B \longrightarrow C + D + Q \; . \tag{7.1}$$

The masses of the particles are m_A, m_B, m_C, and m_D. These reactions will be assumed to occur in a plasma of ion species A and B with densities n_A and n_B and

Maxwellian velocity distribution functions f_A and f_B:

$$f_{A,B} \;=\; \frac{\beta_{\perp A,B} \, \beta_{\parallel A,B}^{\frac{1}{2}}}{\pi^{\frac{3}{2}}} \exp(-\beta_{\perp A,B} \, u_{\perp A,B}^2 - \beta_{\parallel A,B} \, u_{\parallel A,B}^2) \;,$$ (7.2)

where

$$\beta_{\perp A,B} \;=\; \frac{m_{A,B}}{2 \, k \, T_{\perp A,B}} \;, \qquad \beta_{\parallel A,B} = \frac{m_{A,B}}{2 \, k \, T_{\parallel A,B}} \;,$$ (7.3)

and $T_\perp$ and $T_\parallel$ are the perpendicular and parallel temperatures, respectively. These velocity distribution functions are normalized to unity:

$$\int f_{A,B}(\mathbf{u}) \, d^3 u = 1 \;.$$ (7.4)

Consider a simple system of two particles A and B with velocities $\mathbf{u}_A$ and $\mathbf{u}_B$, relative velocity $\mathbf{g}$ and center-of-mass velocity $\mathbf{s}$, related by:

$$\mathbf{u}_A \;=\; \mathbf{s} + \frac{\mu}{m_A} \, \mathbf{g} \;, \qquad \mathbf{u}_B = \mathbf{s} - \frac{\mu}{m_B} \, \mathbf{g}$$ (7.5)

$$\mathbf{g} \;=\; \mathbf{u}_A - \mathbf{u}_B \;, \qquad \mathbf{s} = \frac{m_A \, \mathbf{u}_A + m_B \, \mathbf{u}_B}{m_A + m_B}$$ (7.6)

where

$$\mu \;=\; \frac{m_A \, m_B}{m_A + m_B}$$ (7.7)

is the reduced mass. The reaction rate is given by

$$\begin{aligned} R \;&=\; n_A \, n_B \int \int f_A(\mathbf{s} + \frac{\mu}{m_A} \, \mathbf{g}) \, f_B(\mathbf{s} - \frac{\mu}{m_B} \, \mathbf{g}) \, g \, \sigma(g) \, d^3 g \, d^3 s \\ &=\; n_A \, n_B <\sigma \, g> \;, \end{aligned}$$ (7.8)

where $\sigma(g)$ is the total cross section of this reaction. If the assumption is made that

both particles have the same perpendicular temperature $T_\perp$ and the same parallel temperature $T_\parallel$, then it can be shown that the product $f_A f_B$ can be replaced by a similar product of distribution functions such that s and g can be separated out:

$$f_A(\mathbf{u}_A) f_B(\mathbf{u}_B) \;=\; S(\mathbf{s}) G(\mathbf{g}) \; . \tag{7.9}$$

Note that both S and G are also elliptic and normalized:

$$S(\mathbf{s}) \;=\; \frac{\beta_{\perp M} \beta_{\parallel M}^{\frac{1}{2}}}{\pi^{\frac{3}{2}}} \exp(-\beta_{\perp M} s_\perp^2 - \beta_{\parallel M} s_\parallel^2) \; , \tag{7.10}$$

$$G(\mathbf{g}) \;=\; \frac{\beta_{\perp \mu} \beta_{\parallel \mu}^{\frac{1}{2}}}{\pi^{\frac{3}{2}}} \exp(-\beta_{\perp \mu} g_\perp^2 - \beta_{\parallel \mu} g_\parallel^2) \; . \tag{7.11}$$

Here

$$\beta_{\perp M} \;=\; \frac{M}{2\,k\,T_\perp} \; , \qquad \beta_{\parallel M} = \frac{M}{2\,k\,T_\parallel} \; , \tag{7.12}$$

$$\beta_{\perp \mu} \;=\; \frac{\mu}{2\,k\,T_\perp} \; , \qquad \beta_{\parallel \mu} = \frac{\mu}{2\,k\,T_\parallel} \tag{7.13}$$

and M is the total mass of the system,

$$M = m_A + m_B \; . \tag{7.14}$$

Using the elliptic distribution functions S and G directly, the reaction rate can be written as

$$< \sigma g > \;=\; \int \int S(\mathbf{s}) G(\mathbf{g}) \, g \, \sigma(g) \, d^3g \, d^3s \; . \tag{7.15}$$

After integration with respect to **s**

$$< \sigma g > \; = \; \frac{\beta_{\perp\mu}\, \beta_{\|\mu}^{\frac{1}{2}}}{\pi^{\frac{3}{2}}} \int \exp(-\beta_{\perp\mu}\, g_\perp^2 - \beta_{\|\mu}\, g_\|^2)\, g\, \sigma(g)\, d^3g \; . \tag{7.16}$$

For a Maxwellian that is isotropic (i.e. $T_\perp = T_\| = T$) and with $g^2 = g_\perp^2 + g_\|^2$, the reaction rate can be further simplified to the form:

$$< \sigma g >_{maxw} \; = \; 4\pi \left(\frac{\mu}{2\pi\, k\, T}\right)^{\frac{3}{2}} \int_0^\infty \exp\left(-\frac{\mu\, g^2}{2\, k\, T}\right) g^3\, \sigma(g)\, dg \; . \tag{7.17}$$

7.2   Ion Temperature from Energy Spectra

In the center-of-mass system, the total energy available to the two particles generated (i.e. C and D) is

$$Q + \frac{m_A}{2}(\mathbf{u}_A - \mathbf{s})^2 + \frac{m_B}{2}(\mathbf{u}_B - \mathbf{s})^2 \; = \; Q + \frac{\mu}{2} g^2 \; . \tag{7.18}$$

The fraction given to product C in the center-of-mass system is

$$\hat{E}_C = \frac{m_C\, w_C^2}{2} = \frac{m_D}{m_C + m_D}\left(Q + \frac{\mu}{2} g^2\right) \tag{7.19}$$

where

$$w_C(g) = \sqrt{\frac{2\, m_D}{m_C\,(m_C + m_D)}\left(Q + \frac{\mu}{2} g^2\right)} \tag{7.20}$$

is the velocity of product C in the center-of-mass system. Its velocity in the laboratory system is simply

$$\mathbf{v} = \mathbf{w} + \mathbf{s} \tag{7.21}$$

128

Using, Eq. (7.8), the reaction rate between particle species A and B, which both have Maxwellian distributions, can be expressed as

$$
\begin{aligned}
R &= n_A\, n_B \int \int \int f_A \left(\mathbf{s} + \frac{\mu}{m_A}\mathbf{g} \right) f_B \left(\mathbf{s} - \frac{\mu}{m_B}\mathbf{g} \right) g\, \sigma(g) \frac{\delta(w^2 - w_C^2)}{2\pi w} d^3w\, d^3g\, d^3s \\
&= n_A\, n_B \int \int \int f_A \left(\mathbf{v} - \mathbf{w} + \frac{\mu}{m_A}\mathbf{g} \right) f_B \left(\mathbf{v} - \mathbf{w} - \frac{\mu}{m_B}\mathbf{g} \right) g\, \sigma(g) \\
&\quad \frac{\delta(w^2 - w_C^2)}{2\pi w} d^3w\, d^3g\, d^3v \ .
\end{aligned}
\tag{7.22}
$$

Note that

$$
\int \frac{\delta(w^2 - w_C^2)}{2\pi w} d^3w = \int_0^\infty \frac{\delta(w^2 - w_C^2)}{2\pi w} 4\pi\, w^2\, dw = 1 \ .
\tag{7.23}
$$

Now since the energy E_C of product C in the laboratory system can be made explicit by the manipulation

$$
d^3v = d\Omega\, dv\, v^2 = \frac{d\Omega\, dE_C\, v}{m_C} \ ,
\tag{7.24}
$$

where $d\Omega$ is the solid angle differential in the laboratory system, the energy spectrum of product C can be written as the following general expression:

$$
\begin{aligned}
\frac{d^2 R}{d\Omega\, dE_C} &= \frac{n_A\, n_B\, v}{m_C} \int \int f_A \left(\mathbf{v} - \mathbf{w} + \frac{\mu}{m_A}\mathbf{g} \right) f_B \left(\mathbf{v} - \mathbf{w} - \frac{\mu}{m_B}\mathbf{g} \right) \\
&\quad g\, \sigma(g) \frac{\delta(w^2 - w_C^2)}{2\pi w} d^3g\, d^3w \ .
\end{aligned}
\tag{7.25}
$$

Now, for an isotropic (i.e. $T_\perp = T_\parallel = T$) Maxwellian distribution of particles A

129

and B, this can be written as

$$\frac{d^2R}{d\Omega dE_C} = \frac{n_A\,n_B\,v}{m_C}\int\int S(\mathbf{v}-\mathbf{w})\,G(\mathbf{g})\,g\,\sigma(g)\frac{\delta(w^2-w_C^2)}{2\pi w}d^3g\,d^3w$$

$$= \frac{n_A\,n_B\,v}{m_C}\int_0^\infty \frac{\beta_M^{\frac{3}{2}}\beta_\mu^{\frac{3}{2}}}{\pi^3}\exp\left(-\beta_M v^2 - \beta_\mu g^2\right)\,g\,\sigma(g)\,4\pi\,g^2$$

$$\{\int_0^\infty \exp(-\beta_M\,w^2)\frac{\delta(w^2-w_C^2)}{2\pi\,w}2\pi\,w^2$$

$$\left[\int_{-1}^1 \exp(2\beta_M\,v\,w\cos\theta_w)\,d(\cos\theta_w)\right]\,dw\}\,dg$$

$$= \frac{n_A\,n_B\,v}{m_C}\int_0^\infty \frac{\beta_M^{\frac{3}{2}}\beta_\mu^{\frac{3}{2}}}{\pi^3}\exp(-\beta_M\,v^2 - \beta_\mu\,g^2)2\pi\,g^3\,\sigma(g)$$

$$\exp(-\beta_M\,w_C^2)\frac{\sinh(2\,\beta_M\,v\,w_C)}{\beta_M\,v\,w_C}\,dg$$

$$= \frac{n_A\,n_B\,\mu\,\sqrt{M\,\mu}}{2(\pi\,k\,T)^2\,m_C}\int_0^\infty \exp\left[-\beta_M(v^2+w_C^2) - \beta_\mu\,g^2\right]\,g^3\,\sigma(g)$$

$$\frac{\sinh(2\,\beta_M\,v\,w_C)}{w_C}\,dg \tag{7.26}$$

where

$$\cos\theta_w = \frac{\mathbf{v}\cdot\mathbf{w}}{v\,w}\,. \tag{7.27}$$

Integrating over all solid angles yield

$$\frac{dR}{dE_C} = \frac{2\,n_A\,n_B\,\mu\,\sqrt{M\,\mu}}{\pi(k\,T)^2 m_C}\exp(-\beta_M\,v^2)\int_0^\infty \exp\left[-\beta_M\,w_C^2 - \beta_\mu\,g^2\right]\,g^3\,\sigma(g)$$

$$\frac{\sinh(2\,\beta_M\,v\,w_C)}{w_C}\,dg \tag{7.28}$$

which cannot be evaluated analytically. For fusion plasmas in tokamaks where the ion temperature is typically three orders of magnitude lower than Q (e.g. deuterons with $T = 2$ keV compared with $Q_{D(D,p)T} = 4.03$ MeV), an assumption can be made

130

that the relative velocity $g \ll Q$ such that $w_C(g)$ is approximated by w_{C0} where

$$w_{C0} = \sqrt{\frac{2\,m_D}{m_C\,(m_C + m_D)}}\,Q \qquad (7.29)$$

is the velocity product C would have if the reactants were at rest in the center-of-mass system. This approximation simplifies the integral and allows the sinh function to be approximated by an exponential. Therefore, using Eq. (7.17), the energy spectrum of product C has the form:

$$\frac{dR}{dE_C} \approx \frac{n_A\,n_B}{m_C\,w_{C0}}\left(\frac{\beta_M}{\pi}\right)^{\frac{1}{2}} <\sigma\,g>_{maxw} \exp\left[-\beta_M(v - w_{C0})^2\right] . \qquad (7.30)$$

The spectrum is seen to be a localized peak, centered about the energy $m_C w_{C0}^2/2$. Another characteristic of the spectral peak is its width, and a typical measure is the full width at half maximum ΔE. This quantity is found from letting the exponent be $\ln(1/2)$ and finding the two velocities corresponding to the half maxima of the peak. They are

$$v_{\pm} = w_{C0} \pm \sqrt{\frac{\ln 2}{\beta_M}} . \qquad (7.31)$$

So, the energy spectrum has a full width at half maximum of

$$\begin{aligned}
\Delta E &= \frac{m_C}{2}\left(v_+^2 - v_-^2\right) \\
&= 2m_C w_{C0}\sqrt{\frac{\ln 2}{\beta_M}} \\
&= 4\sqrt{\frac{m_C\,m_D\,\ln 2}{(m_A + m_B)\,(m_C + m_D)}}\,Q\,k\,T \\
&\approx \frac{4}{m_A + m_B}\sqrt{m_C\,m_D\,\ln 2\,Q\,k\,T} .
\end{aligned} \qquad (7.32)$$

Therefore, the ΔE of the spectral peak of fusion products is a simple function of

131
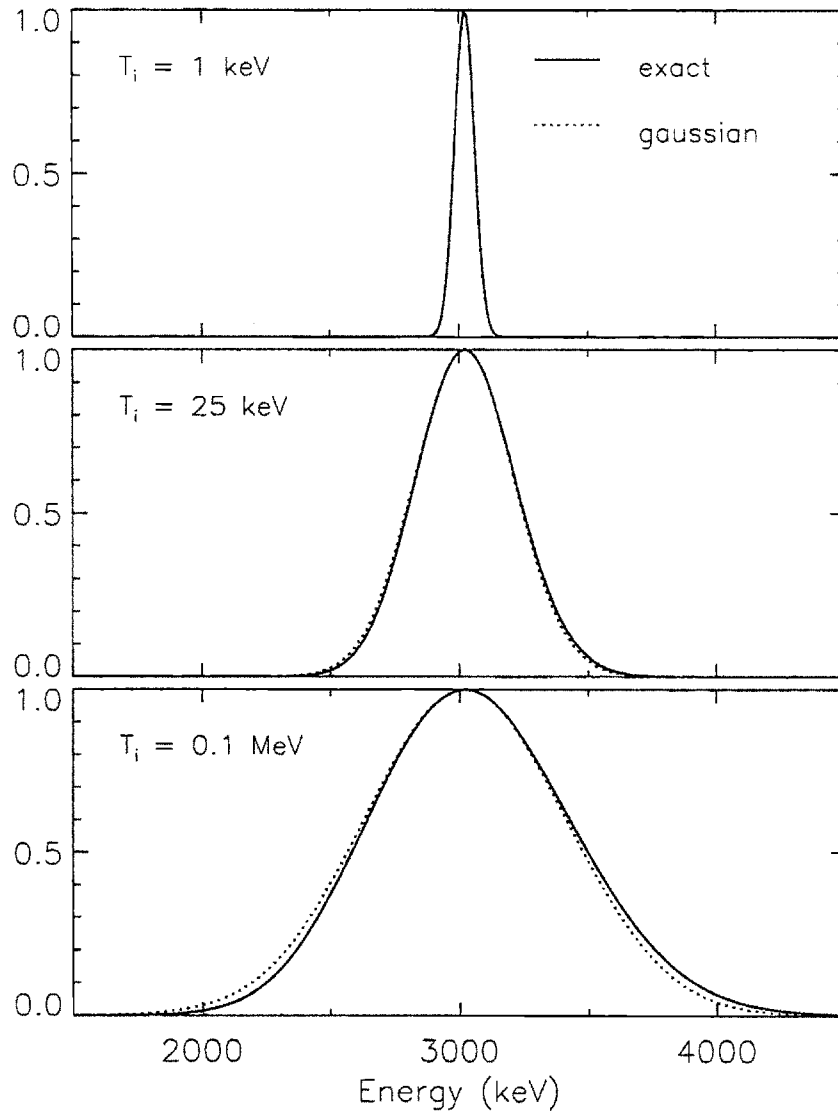
Figure 7.1: Exact spectrum *vs.* gaussian spectrum (normalized) of
D-D protons. For realistic ion temperatures in present-
day fusion devices ($T_i < 10$ keV), the gaussian spectrum
shape is an excellent approximation.

Table 7.1: The FWHM, or ΔE, of the spectral peaks of fusion products is a simple function of the ion temperature.

Reaction	Q (MeV)	ΔE (keV) (T in keV)
D(D,n)^{3}He	3.27	82.5 $\sqrt{T}$
D(D,p)T	4.03	91.6 $\sqrt{T}$
D(T,n)^{4}He	17.6	177 $\sqrt{T}$
D(^{3}He,p)^{4}He	18.3	181 $\sqrt{T}$

the ion temperature in a thermal plasma with a Maxwellian distribution of ions. Table 7.1 shows ΔE for a few fusion reactions. In addition, since the ΔE is symmetric with respect to products C and D, $\Delta E_C = \Delta E_D = \Delta E$. So, for instance, the D-D proton and D-D triton peaks should have the same width. Whereas this chapter's focus is on determining information about the energy (or more precisely, the temperature) of the reacting ions in a thermal Maxwellian plasma through the linewidth of the fusion products, Appendix A gives a personal account where similar energy information of beam particles fusing with target particles has been obtained from studying the linewidth of the detected fusion products.

The energy spectrum is essentially gaussian in shape (it is really gaussian in velocity space). A comparison between the exact spectrum of Eq. (7.30) and a pure gaussian spectrum of the same width (see Fig. 7.1) shows that for realistic ion temperatures in present-day fusion devices ($T_i < 10$ keV), the gaussian spectrum shape is an excellent approximation.

7.3 Temperature Measurements

7.3.1 Spectral Analysis

Figure 7.2 shows a successive series of energy spectra collected with the CFP spectrometer during an ohmic discharge. In this discharge (shot 951130009), the toroidal
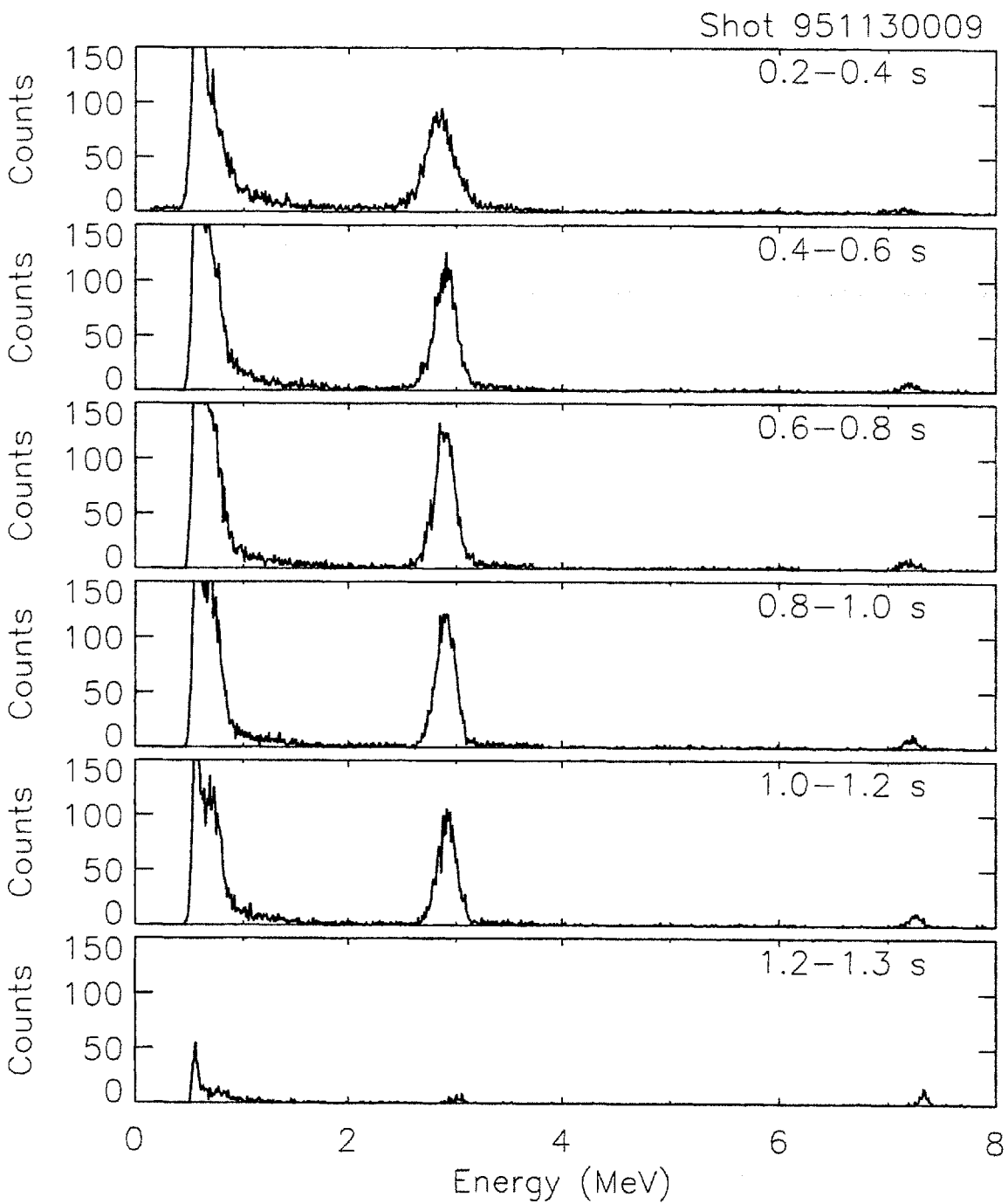
Figure 7.2: Successive energy spectra of D-D protons during an ohmic discharge (shot 951130009, $B_\varphi = 5.3$ T, $I_p = 820$ kA).
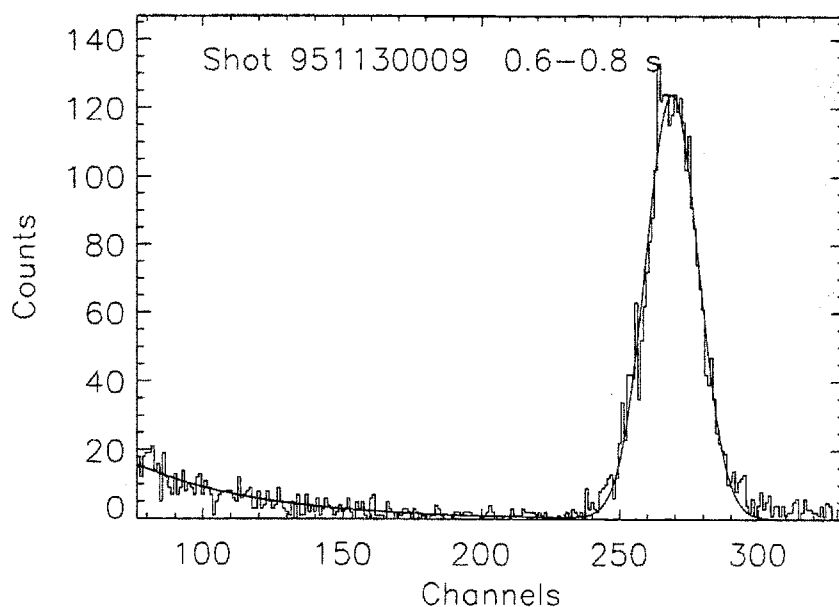
Figure 7.3: Energy spectrum of 3 MeV protons here shown fitted to a gaussian profile. A small amount of low-energy background and high-energy pileup counts are seen.

field on axis was 5.3 T, and the plasma current at flattop (0.5 – 1.0 s.) was 820 kA. Each spectral peak at 2.95 MeV is a collection of D-D protons and its width is directly related to the ion temperature during that time interval. The corresponding peak for D-D tritons is obscured by low-energy background. A hint of D-D tritons at about 700 keV is visible during the time interval 1.0–1.2 s.

Evident as well at above 7 MeV is the pulser peak. As described previously, a periodic pulser signal is introduced into the preamplifier circuit to monitor the conditions of the electronics. In Chapter 4, it has been shown how the changes in the observed pulser count rate are used to study the electronics' dead time behavior. In addition to that, any broadening of the pulser peak (nominally about 30 keV wide) is a measure of any electronic broadening of the spectrum in general. This has to be taken into account in the subsequent analysis in order to correctly measure the ion temperature during the discharge.

Each proton spectrum is fitted to a gaussian profile using a least-squares fitting routine after subtraction of background counts. Figure 7.3 shows an example of such a fit (for the spectrum collected from $t = 0.6$ and 0.8 s during shot 951130009) where there are low-energy background and higher-energy counts due to pileup. This results in a measured spectral width ΔE_{meas}. Corrections, however, have to be made to this measured proton width for two distinctly different processes. First of all, protons that are detected by the charged fusion product spectrometer have passed through an aperture covered by a 3 μm aluminum foil. A 3 MeV proton loses on average about 70 keV [58] while traversing the foil. Thus, the D-D proton peak is downshifted in energy by this amount. In addition, because the stopping power of protons in aluminum increases with decreasing energy in the MeV region, protons with higher energy will on average lose less energy than ones with lower energy. This process, known as energy "straggling," manifests itself through a broadening, ΔE_s, of the spectral peak. This can be estimated by the formula [59–61]

$$\Delta E_s = A_s \sqrt{t}, \tag{7.33}$$

where A_s, the straggling constant, is 12.5 keV/$\sqrt{\mu m}$ for hydrogenic ions in aluminum and t is the foil thickness in μm.

On the other hand, high count rates also broaden the D-D proton peak. This effect, to be discussed in the next chapter, is captured by the broadening of the pulser peak. In most cases, this broadened pulser peak is characterized by also assuming a gaussian profile, with a width ΔE_{pul}.

With correction for the aforementioned broadening effects to the proton peak, the corrected spectral width ΔE_{corr} is given by

$$\Delta E^2_{corr} = \Delta E^2_{meas} - \Delta E^2_{pul} - \Delta E^2_s, \tag{7.34}$$

136

giving an ion temperature (from Table 7.1 for the D-D reaction) of

$$T_i = \left(\frac{\Delta E_{corr}}{91.6} \right)^2 . \tag{7.35}$$

where both T_i and ΔE_{corr} are in units of keV. In practice, a conversion from spectrum channels to energy units has to be applied. Thus, the ion temperature has the expression

$$T_i = \frac{1}{91.6^2} \{ (\Delta C_{meas}^2 - \Delta C_{pul}^2) \, m^2 - \Delta E_s^2 \} , \tag{7.36}$$

where ΔC_{meas} and ΔC_{pul} are, respectively, the measured proton width and pulser width in channels, and m is the conversion factor from channel to energy.

The uncertainty σ_{T_i} of the measurement is calculated by the following equation which shows how the uncertainties of different measurements are propagated in the calculation:

$$\sigma_{T_i}^2 = \left(\frac{\partial T_i}{\partial \Delta C_{meas}} \right)^2 \sigma_{\Delta C_{meas}}^2 + \left(\frac{\partial T_i}{\partial \Delta C_{pul}} \right)^2 \sigma_{\Delta C_{pul}}^2 + \left(\frac{\partial T_i}{\partial m} \right)^2 \sigma_m^2$$

$$+ \left(\frac{\partial T_i}{\partial \Delta E_s} \right)^2 \sigma_{\Delta E_s}^2 , \tag{7.37}$$

where

$$\frac{\partial T_i}{\partial \Delta C_{meas}} = \frac{2 \, \Delta C_{meas} \, m^2}{91.6^2} \tag{7.38}$$

$$\frac{\partial T_i}{\partial \Delta C_{pul}} = \frac{-2 \, \Delta C_{pul} \, m^2}{91.6^2} \tag{7.39}$$

$$\frac{\partial T_i}{\partial m} = \frac{2 \, (\Delta C_{meas}^2 - \Delta C_{pul}^2) \, m}{91.6^2} \tag{7.40}$$

137

$$\frac{\partial T_i}{\partial \Delta E_s} = \frac{-2\,\Delta E_s}{91.6^2}\,.$$ (7.41)

As illustrated in Fig. 7.4, the aperture of the charged fusion product spectrometer accepts protons directly from the hot plasma center during the flattop portion of (in fact, most of) the discharge. Since the fusion source profile is highly peaked at the center, protons predominantly originate from the hot center of the plasma even though all protons born on the orbits intercepting the spectrometer contribute to the detected spectrum. As a result, the spectrometer is, to first order, measuring the central ion temperature $T_i(0)$.

7.3.2 Discussion

Applying the procedure to the CFP spectra shown in Fig. 7.2, we arrive at the central ion temperature, or $T_i(0)$, measurements shown in Fig. 7.5(a) (marked by diamonds). The vertical cross hairs are the calculated error bars while the horizontal cross hairs signify the integrated time intervals. The high uncertainty in the measurement between 0.2 and 0.4 s is due to a high uncertainty in the pulser peak spectral width during this time period.

Also shown are central ion temperature measurements for the same discharge from calculations based on fusion neutron yield [18]. These calculations rely on measured density profiles and assumed temperature profiles and have an overall uncertainty of not more than 10%. To within the uncertainties of the two measurements, they agree well.

The ion temperature in Alcator C-Mod is also measured by the high-resolution x-ray (HIREX) spectrometer [19]. This measurement is based on the Doppler broadening of x-ray impurity lines, in this case, lines of hydrogen-like and helium-like argon injected into the machine. Shown in Fig. 7.5(b) are ion temperature measurements for another ohmic discharge (shot 951115028). The results from all three techniques are provided. It has to be noted that this particular HIREX spectrometer channel

138
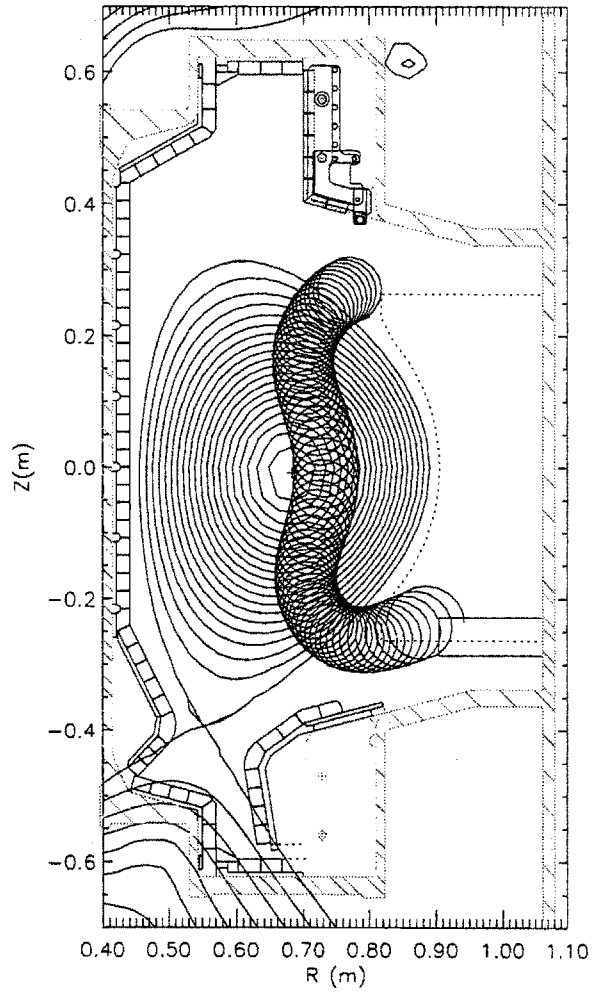
Figure 7.4: A representative proton orbit calculated with the code EPSILON shows that protons originate from the hot center of the plasma during the flattop portion of shot 951130009 ($B_\varphi = 5.5$ T, $I_p = 820$ kA). The plasma equilibrium is calculated using the EFIT code.
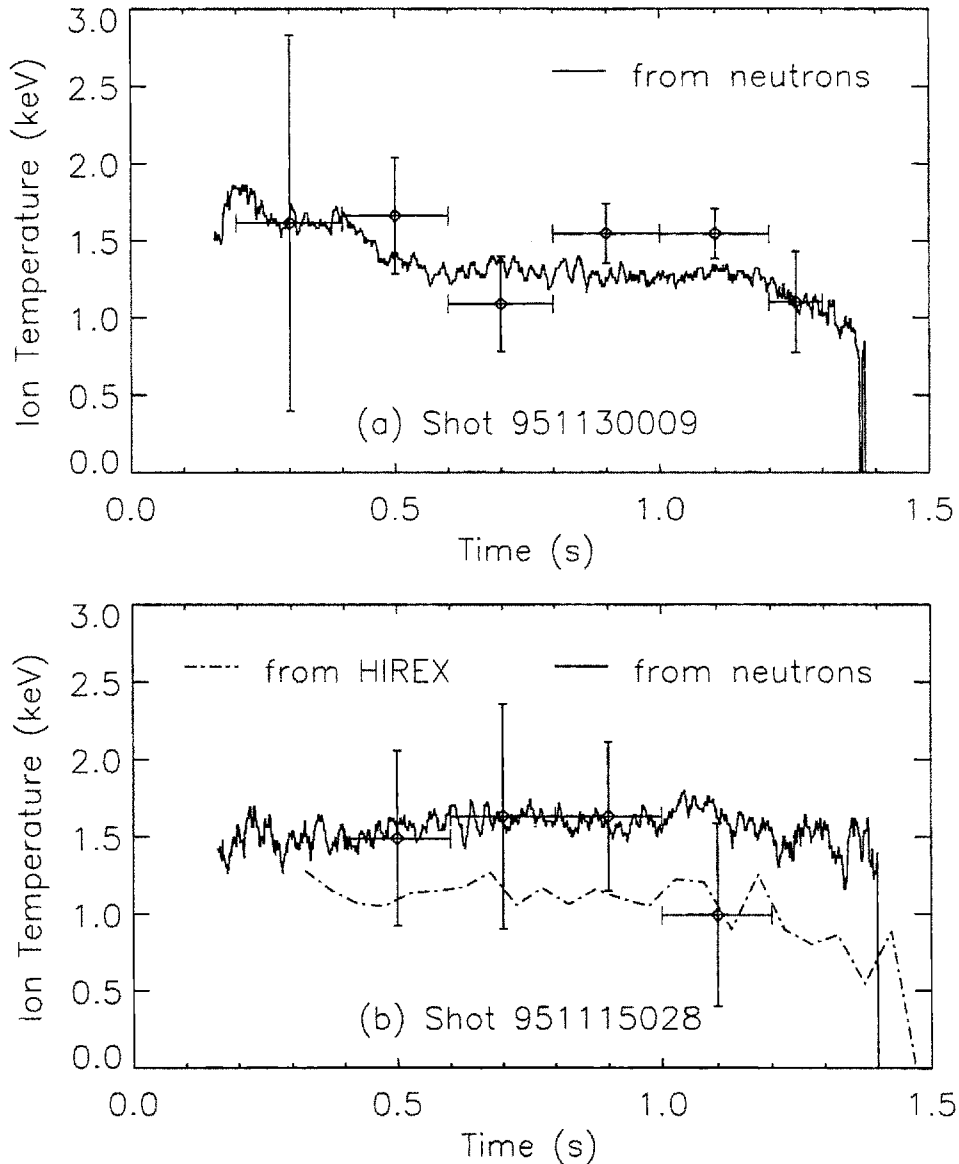
Figure 7.5: Central ion temperature measurements during ohmic discharges. (a) T_i measured from D-D proton spectra (diamonds) and from the neutron yield (solid curve) during shot 951130009 ($B_\varphi = 5.5$ T, $I_p = 820$ kA). The horizontal cross hairs show the integrated time intervals. (b) T_i measured from D-D proton spectra, from neutron yield, and from x-ray line broadening measurements from the HIREX (dash-dot curve; hottest part of the plasma the HIREX viewed corresponds to about $r = a/2$) during shot 951115028 (similar B_φ and I_p).

was not viewing the plasma center during this discharge. The hottest part of the plasma that it was viewing corresponds to about $r = a/2$. Assuming a temperature profile of $T_i \sim [1 - (r/a)^2]^5$, the temperature measured by this HIREX channel is approximately 65% $T_i(0)$. The three independent ion temperature measurements by the three diagnostics show good agreement throughout the discharge.

The dominant contribution to the uncertainty of the present $T_i(0)$ measurement using D-D protons stems from the pulser electronic correction term, i.e., the second term on the right side of Eq. (7.37). The counting statistics from the pulser peak was not high because the pulser frequency employed ($\approx$ 1000 Hz) was low. In the future, a higher-frequency pulser has to be introduced. The least-squares fitting of each pulser spectrum to a gaussian was made more difficult by the substantial electronic broadening encountered. The widths of the pulser peaks, though smaller, are typically of the same order as the widths of the proton peaks. Therefore, the uncertainty in the $T_i(0)$ measurement with charged fusion products was sometimes as high as 50%.

In theory, the ion temperature can similarly be obtained from analyzing the D-D triton spectrum, as the width of the triton peak due to a finite ion temperature should be equivalent to that of the proton peak. In practice, this had been difficult because of the low-energy background that always interfered with the observation of the triton peak. There were also instances where the triton peak was clearly observed but, unfortunately, the pulser was not available.

To conclude, the CFP spectrometer has been demonstrated to measure the ion temperature. The uncertainty of the measurement stems mostly from the pulser electronic correction, which is necessary because of the encountered spectral broadening. The measurement has shown good agreement with the temperature measured by the neutron diagnostic and the HIREX system.
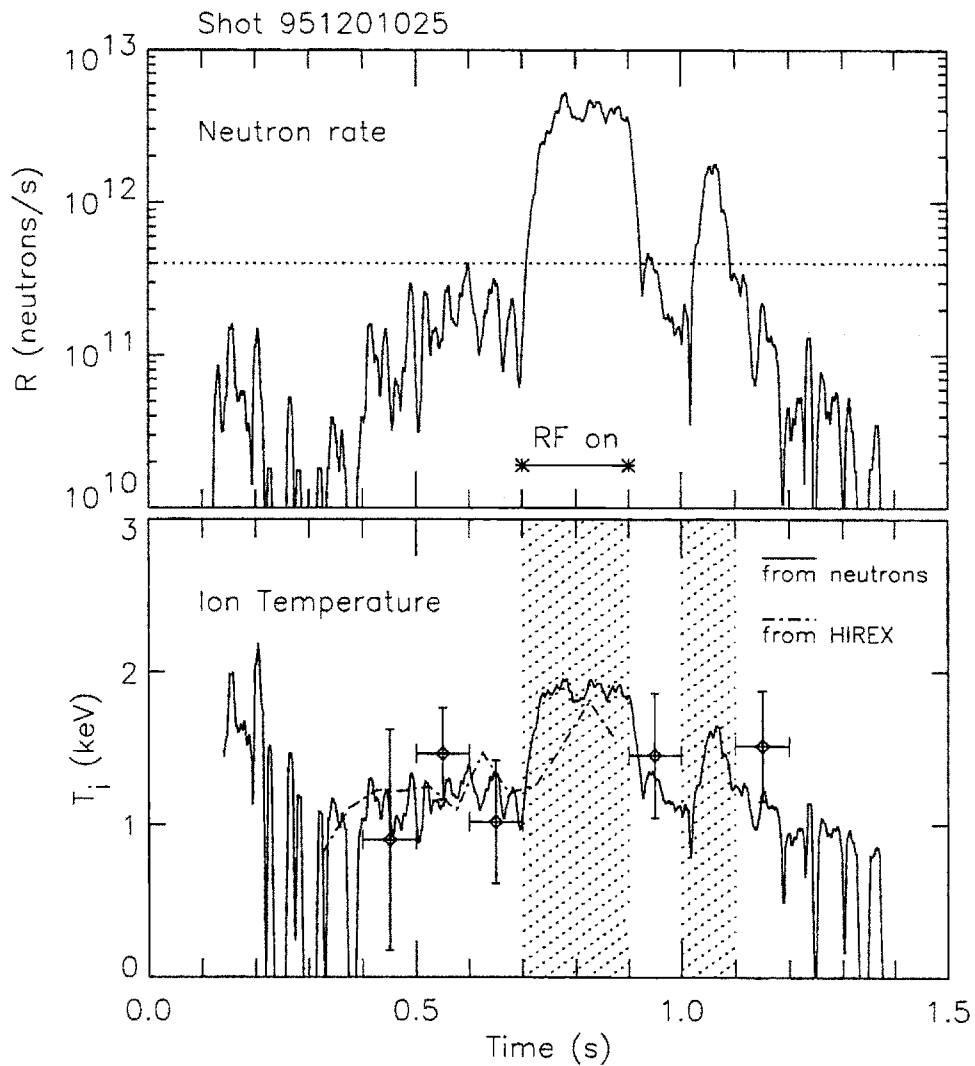
Figure 7.6: Neutron rate and central ion temperature for shot 951130009. ICRF was on from $t = 0.7$ to 0.9 s. At $t = 1$ s, a deuterium pellet was fired in to the plasma. During the two events, the neutron rate showed drastic increases making T_i measurement with D-D protons impossible.
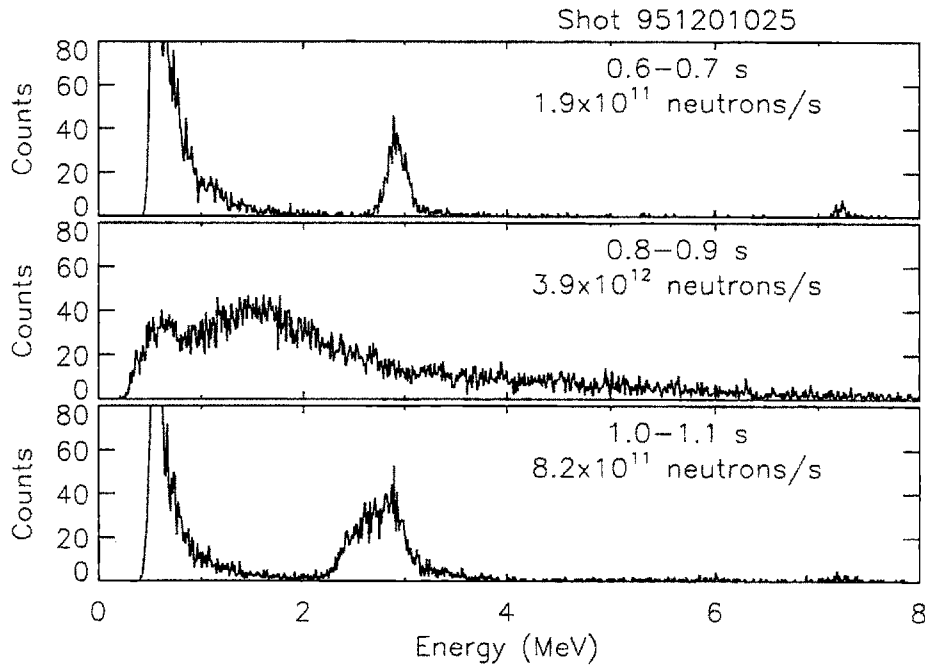
Figure 7.7: Three energy spectra of D-D protons during shot
951201025 are presented.

7.3.3 Difficulties at High Neutron Rate

Figure 7.6 shows the neutron rate and the ion temperature for a plasma discharge
(shot 951201025) with ICRF heating (0.7–0.9 s) and deuterium pellet fueling (fired at
1 s). During the 0.2 s of ICRF heating at 2.5 MW, the ion temperature rose from about
1.2 keV to about 1.9 keV, resulting in a neutron rate of over 4×10^{12} neutrons/s. The
pellet injection also brought about a period of about 20 ms during which T_i was above
1.6 keV and the neutron rate was above 1.5×10^{12} neutrons/s. In the interim periods
when the plasma was purely ohmic, temperature measurements via D-D protons
were possible and gave very agreeable results (see Fig. 7.6). However, temperature
measurement with the CFP spectrometer was made difficult during ICRF heating
and pellet injection.

Energy spectra corresponding to three 100-ms intervals of the three different
plasma conditions (*i.e.*, ohmic, ICRF, and pellet) are given in Fig. 7.7. In each

spectrum, the time interval and the mean neutron rate are shown. In the ohmic case (top spectrum), the mean ion temperature was calculated using the technique outlined in §7.3.1. In the ICRF heating case, the spectrum (middle) has been so badly distorted that no useful information (ion temperature or fusion rate) can be obtained. In the pellet injection case, the spectrum (bottom) shows a broadened D-D proton peak with asymmetric features. The width of the peak is almost 3 times that of the ohmic case. The pulser counts (at about 7.2 MeV) have dispersed similarly compared to the ohmic case. While the spectral degradation still permits an evaluation of the fusion proton yield, it is impossible to calculate the ion temperature from analyzing this spectrum.

The fact that spectral degradation takes place in this last case rules out the possibility that some kind of pickup from the ICRF is responsible. The problem seems to be directly related to the neutron rate. From experience, ion temperature measurements with the CFP spectrometer have been possible only when the neutron rate has been below about 4×10^{11} neutrons/s. This value has been plotted in the neutron rate trace of Fig. 7.6. The dotted line nicely separates the time intervals, depending whether temperature measurement had proved successful or not. This greatly limits the regime of operation of the spectrometer as an ion-temperature diagnostic. The effects of the neutron rate on the CFP spectrometer will be discussed in detail in the next chapter.

Chapter 8

Problems with the CFP

Spectrometer

In the course of the different run campaigns in which the CFP spectrometer has operated, problems with the CFP spectrum have been encountered. These include loss of counts, downshifting in energy, loss of energy resolution, and even the total loss of signal. In the search for an explanation for this, a trend was found: the problem is really count-rate related. The attention was then changed to focus on finding the causes of the high count rate and their nature.

The silicon detector is sensitive to charged particles because electron-hole pairs are generated in the direct interaction between the charged particles and the silicon atoms. These charged pairs, when collected in an applied electric field, constitute the basic electrical signal from the detector. Unfortunately, in the environment of the tokamak, the sensitivity of the detector to other influences, like high energy photons and neutrons, can become important. In this chapter, these factors affecting the diagnostic system are examined in detail.

To help identify the problems with the CFP spectrometer system, a parallel detection system was set up. This will be referred to as the monitor system hereafter. It includes a silicon detector (exactly the same as the detector in the CFP spectrometer),
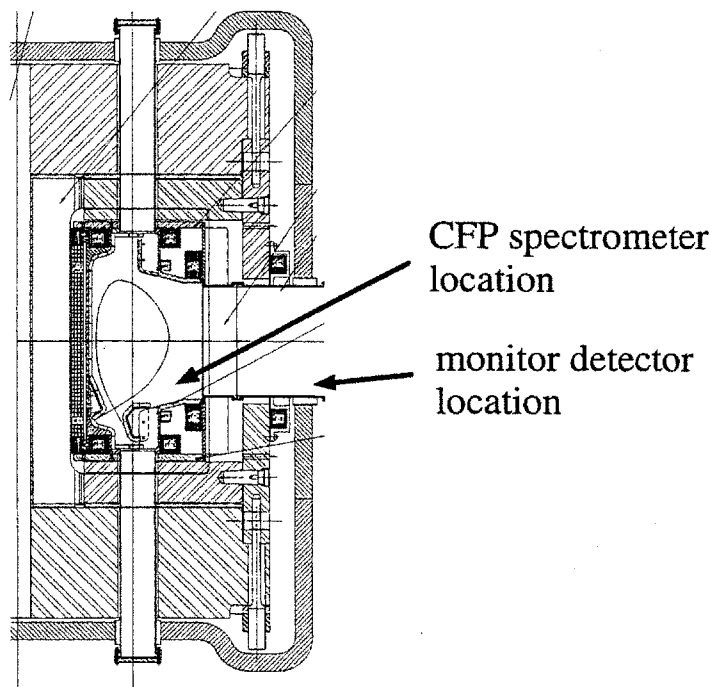
Figure 8.1: Locations of the CFP spectrometer and the monitor system's detector at K port.

but it is placed outside of K port in air (at R $\sim$ 1.7 m). The monitor system is added to monitor the detector response to photons and neutrons alone. Being outside the vacuum vessel, this system does not detect any CFPs. Since only one multichannel analyzer (MCA) is available, the monitor system usually does not include an MCA.[1] The pulses from its shaping amplifier are fed to a single channel analyzer (SCA) that accepts signals of all energies. These are then processed by a scaler, which records the number of counts every 2 ms.

---

[1]The MCA was connected to the monitor system for a few runs.
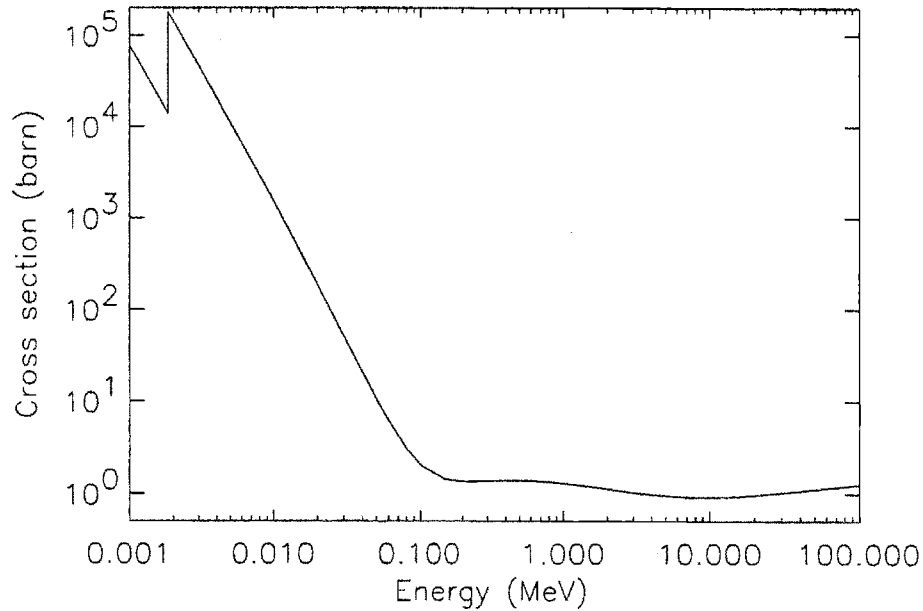
Figure 8.2: Energy dependence of the photon reaction cross section in silicon [62]. A barn is equivalent to 10^{-24} cm^2.

8.1 Influences of Hard X Rays

High energy photons in the form of hard x rays and γ rays from neutron capture, *i.e.*, (n,γ) reactions, are present in the tokamak environment.[2] These photons interact with the silicon in the detector via three main processes: photoelectric effect (dominant for photon energies of up to 50 keV), Compton scattering (50 keV to about 15 MeV), and pair production (above 15 MeV) [62]. The total reaction cross section in silicon as a function of the photon energy is shown in Fig. 8.2 [62]. These processes lead to the partial or complete transfer of the photon energy to the kinetic energy of mobilized electrons, which can be deposited in the silicon detector's active region. In this section, we discuss the observed response of the silicon detector to hard x rays alone. Discussion of the response to γ rays from neutron radiative capture will be deferred to the section on neutrons (§8.2).

---

[2]The small branching ratio [25] for D(D,γ)α of 1.0×10^{-7} makes fusion γ rays virtually irrelevant compared to neutron capture γ rays.
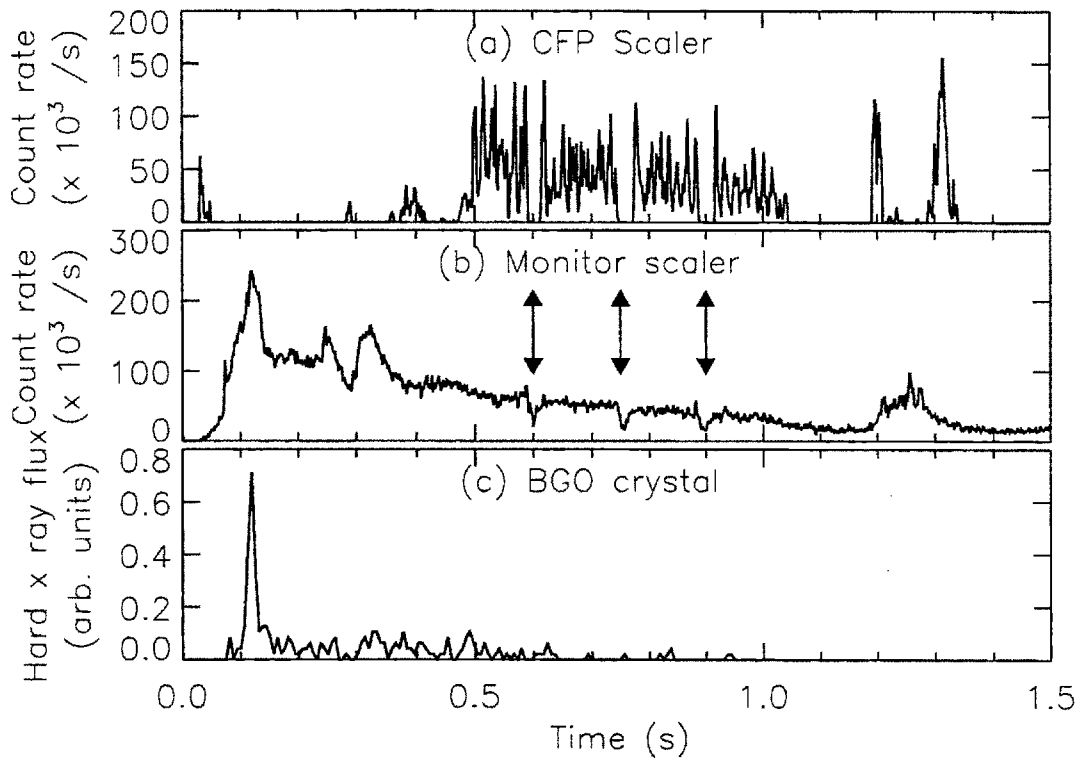
Figure 8.3: Time history of scalers for shot 950216011 showing sensitivity to hard x rays (measured by the $Bi_4Ge_3O_{12}$ scintillator). The CFP scaler recorded system saturation during most of the discharge, and the monitor scaler showed also a tremendous dead-time/pile-up problem. The drop in the scaler signals at 0.6, 0.75, and 0.9 s were due to the insertion of a fast scanning probe in F port, temporarily reducing the runaway electron flux.

The CFP spectrometer system is disturbed strongly by the signal pulses that arise from hard x rays. Hard x rays are produced through bremsstrahlung when runaway electrons hit structures inside the vacuum vessel. When hard x rays are produced, it usually happens in the early phase of the discharge. Under certain conditions, the flux of fast electrons can have a rather long life time, so that hard x rays can sometimes accompany a discharge up to the end.

Figure 8.3 illustrates through shot 950216011 the adverse effect intense hard x rays have on the CFP spectrometer system. The top trace is the scaler signal from the CFP spectrometer. Its SCA was set to accept signals corresponding to energies above 2 MeV. The middle trace comes from the scaler of the monitor system. Its SCA was set to accept signals of all energies. The bottom trace comes from the bismuth germanate ($Bi_4Ge_3O_{12}$) scintillation detector monitoring the hard x ray flux at K port.

The high hard x ray flux measured by the $Bi_4Ge_3O_{12}$ scintillator at 0.12 s was responsible for the tremendous response[3] experienced by both the CFP spectrometer and the monitor systems early on in the discharge. In the case of the CFP spectrometer system, the amplifier actually experienced periods of temporary shutdown because the x ray flux it experienced was too high.[4] This persisted for the better part of the first 0.5 s of the discharge. With a lower hard x ray flux on its detector, the monitor system did not shutdown. However, the system was suffering from a very high dead-time/pile-up problem, especially at the x ray flux spike (over 2×10^5 counts/s). After the initial high hard-x-ray flux, the $Bi_4Ge_3O_{12}$ scintillator showed a much reduced signal for most of the discharge, whereas the two systems showed a gradually decreasing signal level, which lasted for most of the 1.6 s of the discharge.

---

[3] As discussed later in this chapter (§8.4), an upper count rate limit for obtaining undistorted energy spectra is about $(1–1.5) \times 10^4$ counts/s. An ultimate count rate limit is typically $\sim 10^5$ counts/s where saturation and system shutdown becomes imminent.

[4] Amplifier shutdown is observable as a null count rate for a prolonged period of time in the CFP scaler time trace. Note that during those same time periods, the monitor scaler signal level was nonzero. Since the CFP spectrometer was inside the vacuum vessel while the monitor detector was in air outside of K-port's flange and between the igloo blocks, the hard x ray flux impinging on the CFP detector was understandably higher.
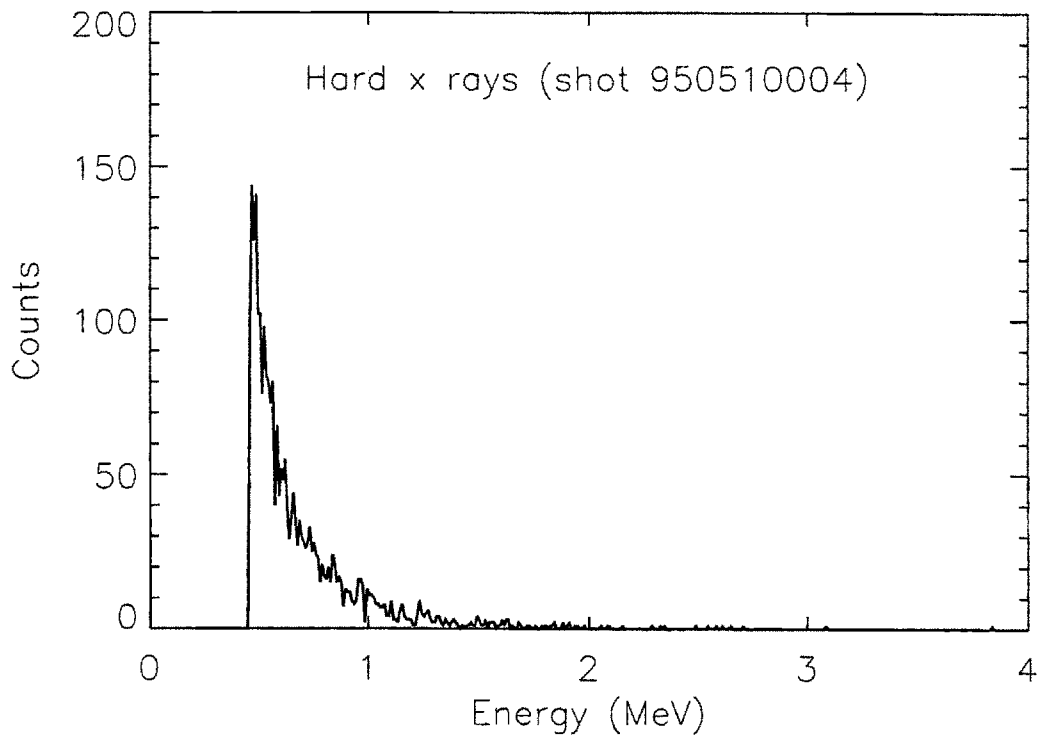
Figure 8.4: Hard x ray spectrum collected by the monitor spectrometer. The calibration is roughly 10 keV per channel, indicating that the energy of some of these events exceeds 1 MeV. This was collected during a run with no neutrons generated.

This is likely due to their different locations.

Something else interesting happened during this discharge. A fast scanning Langmuir probe (FSP), designed to have rapid axial motion in and out of the scrape-off layer of the plasma, was fired into the last closed flux surface three times during the discharge: at $t = 0.6$, 0.75, and 0.9 s. The inserted scanning probe (located in F bottom port) would have gone far enough to have intercepted some of these runaway electrons. At those three discrete times when the probe was inserted, a corresponding reduction in the scaler signals was clear, supporting the earlier assertion that the signals were due to hard x rays.

An energy spectrum of hard x rays generated in Alcator C-Mod as recorded by the monitor spectrometer is shown in Fig. 8.4. This spectrum comes from an integration throughout the whole discharge. This was from a run day (950510) with hydrogen/^{3}He plasma for studying ICRF mode-conversion heating. Very few neutrons were produced due to the lack of deuterium. For discharges during the same run with little hard x rays detected, there were fewer than 100 counts collected throughout a discharge.

In the third run campaign, a 1.27-cm thick stainless steel shield was added around the CFP spectrometer reentrant hardware. It was effective in reducing the hard x ray flux. In addition, the generation of hard x rays can often be avoided by techniques like greater gas prefill of the vessel which, in turn, increases the plasma density for retarding the buildup of runaway electrons. Therefore, the detector's sensitivity to hard x rays is not the main problem that the spectrometer faces. The fundamental source of the observed problem with the CFP spectrometer lies with the detector's sensitivity to neutrons and neutron-induced γ rays, which are discussed and analyzed in the next section.

8.2   Influences of Neutrons

This discussion about the influences of neutrons on the CFP spectrometer is divided into several sections. Evidence is first presented which shows that the undesired low-energy background is correlated with the neutron rate. This is followed by a discussion on neutron interactions with matter, leading to an experimental determination of the detector's sensitivity to both neutrons and γ rays. (γ rays are generated in neutron capture reactions.) A brief analysis is performed with the Monte Carlo Neutron and Photon Transport (MCNP) code [63] to estimate the local neutron and γ-ray fluxes at the detector and the resulting number of interactions. The simulation results show that the undesired low-energy counts result from both elastic collisions of neutrons and interactions of γ ray (from neutron capture) with the silicon detector. However, barring pile-up of lower-energy events, events that deposit more than 0.5 MeV (per

151
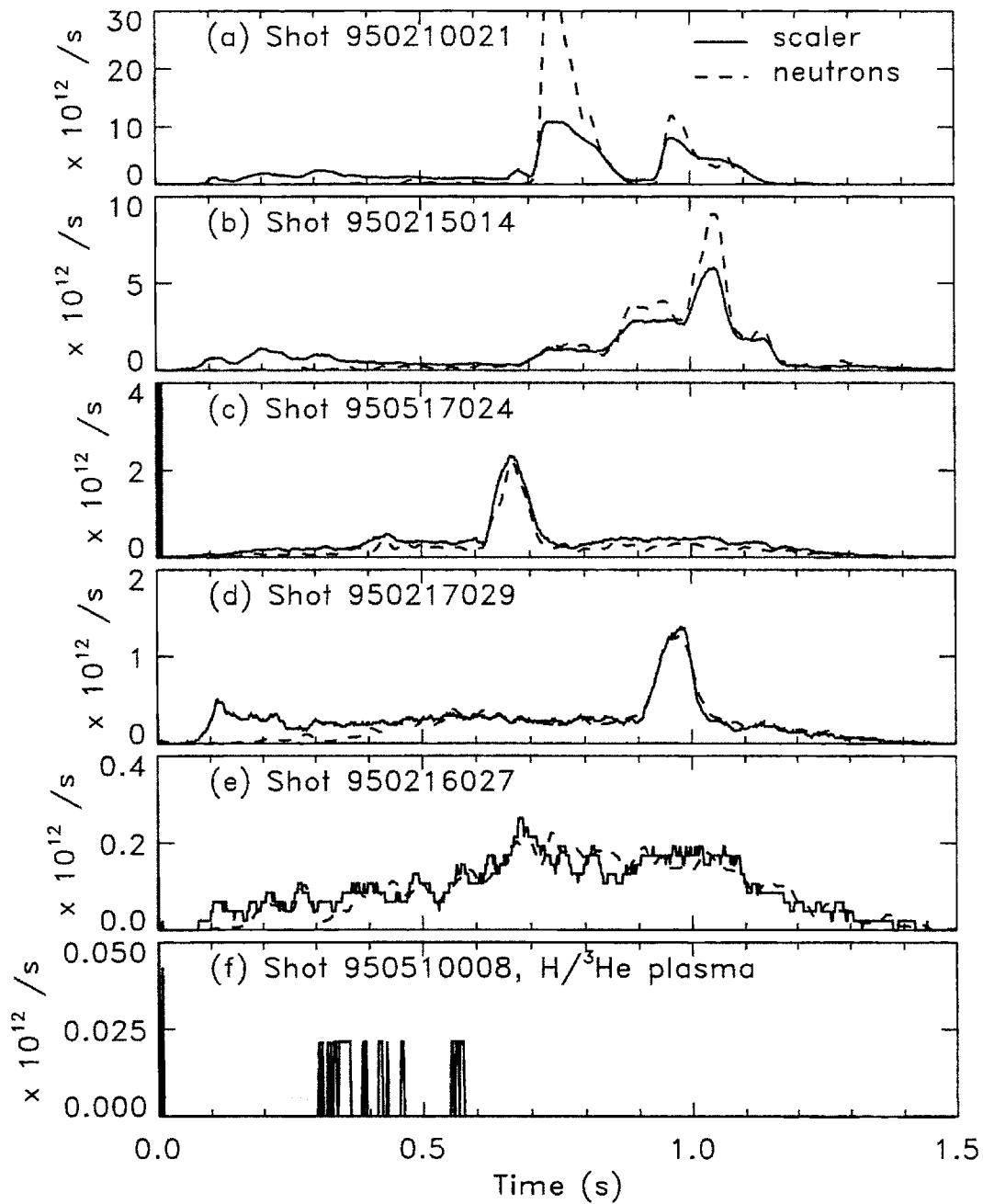
Figure 8.5: Comparison of time traces of the monitor scaler signal and the neutron rate. The same normalization factor, from shot 950217029 for the period from 0.7 s to 1.1 s, is used for all discharges. A clear correlation between the monitor system's signal and the neutron rate is observed.

event) in the silicon detector are the result of γ-ray interactions with the silicon detector alone.

8.2.1 Correlation of Low-Energy Background Counts with Neutron Signal

It has always been known that the silicon detector is sensitive to neutrons. However, other researchers have never reported them to produce any effect on their CFP diagnostics that is more than negligible. On the other hand, the CFP spectrometer in Alcator C-Mod has been plagued by low-energy counts in the spectrum from the early stages of the project. Though the connection was not immediately identified, the number of these low-energy counts was found to be directly proportional to the neutron rate. Since the CFP detector needs to be close to the plasma inside the C-Mod vessel, no practical amount of neutron shielding can be implemented. Furthermore, unlike hard x rays, neutrons are generated whenever CFPs are generated by D-D fusion, and at approximately the same rate.

Figure 8.5 gives a poignant account of the sensitivity of the silicon detector to neutrons, as observed in Alcator C-Mod. Each plot gives a comparison of the time histories of the monitor scaler signal and the neutron rate. As in the case described in Fig. 8.3, the monitor system was identical to the CFP spectrometer system, with the exception that the detector was outside of K port in air. The normalization factor for each discharge is identical: the normalization is from shot 950217029 for the period from 0.7 s to 1.1 s. This gives a monitor detector count rate of $2.34 \times 10^{-8} \times$ the global neutron rate. The measured fluence on this detector was correspondingly less than that on the CFP detector itself, and less prone to saturate. (In fact, for each of the four discharges shown in Figs. 8.5(a)–(d), the electronics of the CFP spectrometer system did experience severe amplifier count rate saturation and prolonged preamplifier saturation for some part of the discharge.)

A general correlation between the monitor system's signal and the neutron rate is

evident, for neutron rates from 10^{11} to close to 10^{13} neutrons/s. This also shows that the silicon detector's response to neutrons is not negligible, as an Alcator neutron yield of 10^{12} neutrons creates a response of 23400 counts.[5] Hard x rays existed in the initial phase , $i.e.$, $t \lesssim 0.5$ s, of discharges (a), (b), and (d). This accounts for the initial disagreement in the two time traces at those time periods. At the same time, signs of pile-up and saturation of the monitor system's electronics are evident for discharges (a) and (b) when the neutron rate was high. The results of pile-up and saturation in the monitor system is the loss of counts. So, in the corresponding time periods, the normalized monitor system's signal appears lower than the neutron rate. During the brief period from 0.73 to 0.77 s in discharge (a), the monitor system's amplifier was processing about 2.5×10^5 counts per second. As will be discussed in §8.4, this count rate is too high, resulting in distortion in the energy spectrum and significant loss of counts. The discharge shown in Fig. 8.5(f) was part of a run (950510) with hydrogen/^{3}He plasma for studying ICRF mode-conversion heating. Very few neutrons were produced due to the lack of deuterium. Correspondingly, very few counts were collected by the detector in the monitor system.

8.2.2 Neutron Spectrum

Figure 8.6 shows two energy spectra obtained due to the presence of neutrons, one from the CFP spectrometer system, and the other from the monitor system. Both spectra have been normalized to correspond to a neutron yield of unity (one neutron). Shot 950407010 is from a day when C-Mod was operated in a reverse field configuration; consequently, no CFPs were detected because of a change in the ∇B drift direction (see §6.1.3). The spectrum for shot 950517024, recorded by the monitor system, was also counting neutrons alone. Figure 8.5(c) has shown that the monitor scaler signal and the neutron rate (from the neutron diagnostic system) time traces for that shot correlate well, an indication that hard x rays were absent.

---

[5]Typical neutron rates of Alcator C-Mod are from 10^{11} to over 10^{13} neutrons/s. As high as 10^{16} neutrons/s is anticipated in future campaigns.
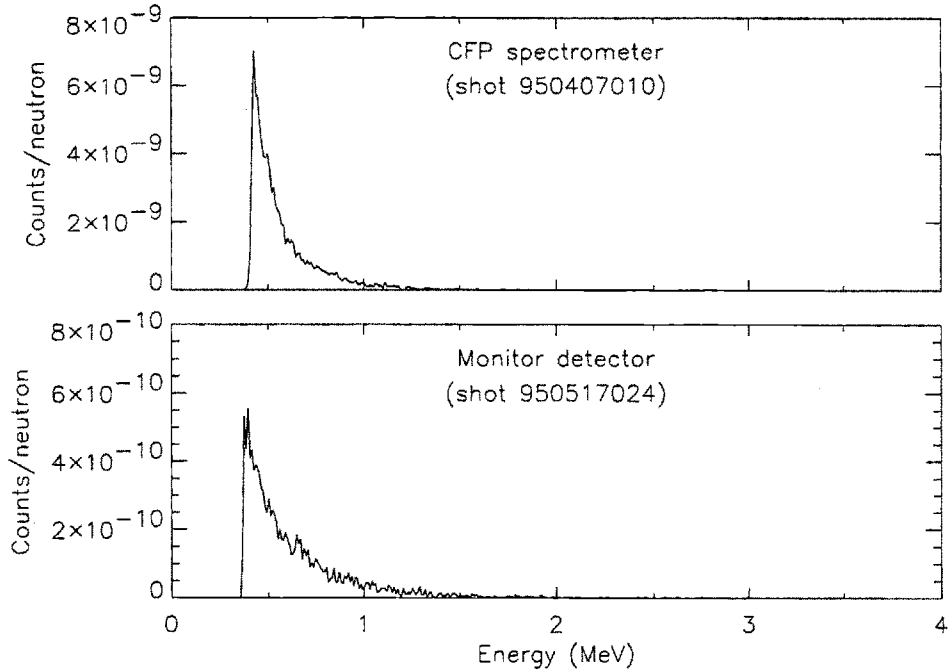
Figure 8.6: Neutron spectra collected by the CFP spectrometer and the monitor spectrometer systems. Both spectra have been normalized to correspond to a neutron yield of unity (one neutron). Note the different scales of the y axes. The spectral shape is very similar to that of the hard x ray spectrum (see Fig. 8.4).

Listed in Table 8.1 are the number of these neutron-induced counts in each system as a function of the region of integration in the spectrum. So, for instance, when the neutron yield is 10^{12} neutrons, one can expect 5.0×10^4 counts in the CFP spectrometer system and 7.1×10^3 counts in the monitor system occupying channels in the spectrum above 0.5 MeV, simply due to neutrons. Note that this result does not conflict with the previously determined number of 2.34×10^4 counts in the monitor system for every 10^{12} neutrons created because of the restricted region of integration in the spectrum.

It can also be seen that the spectra correlated with fusion neutrons and the spectra arising from hard x rays (recall Fig. 8.4) have very similar shapes. Consequently, when significant amounts of both hard x rays and neutrons exist, it is difficult to

Table 8.1: Neutron-induced background counts (per source neutron) as a function of the region of integration in the CFP spectrometer's and monitor system's spectra given in Fig. 8.6.

Lower limit of integration	Counts (CFP system)	Counts (monitor system)	Ratio (CFP/monitor)
0.45 MeV	7.1×10^{-8}	8.6×10^{-9}	8.3
0.5 MeV	5.0×10^{-8}	7.1×10^{-9}	7.1
0.6 MeV	2.8×10^{-8}	4.7×10^{-9}	6.0
0.7 MeV	1.7×10^{-8}	3.3×10^{-9}	5.2
0.8 MeV	1.0×10^{-8}	2.3×10^{-9}	4.5
0.9 MeV	6.3×10^{-9}	1.7×10^{-9}	3.8
1.0 MeV	4.0×10^{-9}	1.2×10^{-9}	3.4

distinguish between them from simply examining the energy spectrum obtained.

8.2.3 Neutron Interaction

Neutrons carry no charge and therefore do not interact with matter via the coulomb force, which dominates the energy transfer mechanisms for charged particles. Instead, neutrons interact directly with the nuclei of the absorbing matter through nuclear reactions, which may result in energetic charged particles that can be detected in the detector's active volume. The most important interactions are elastic scattering, where a portion of the neutron's kinetic energy is transferred to a recoil nucleus, and neutron capture, which results in the emission of a γ ray. In the former case, it is most important to consider neutron scattering within the silicon in the detector because the recoil nucleus of any other neighboring material has a short mean free path (of order a μm) in the material itself and does not reach the detector. In the latter case, however, neutron capture, i.e., (n,γ) reactions, in any structural material in the vicinity of the detector can contribute to the overall γ-ray flux reaching the silicon detector. As discussed in §8.1, the subsequent γ-ray interactions with silicon result in the creation of energetic electrons that can be stopped in the detector. Other less important reactions include inelastic scattering and particle reactions like (n,α) and

(n,p) reactions.[6]

Elastic scattering between neutrons and silicon nuclei, however, cannot satisfactorily explain the perceived response of the detector in the presence of neutrons. When a neutron with mass m has an elastic collision with any nucleus with mass M, the maximum energy gained by the recoil nucleus is [29]:

$$T_{max} = T_n \left[1 - \left(\frac{m - M}{m + M} \right)^2 \right] , \tag{8.1}$$

where T_n is the initial kinetic energy of the neutron. (This occurs when the collision is head-on.) For an initial neutron energy of around 2.5 MeV, which is the birth energy of a D-D neutron, the maximum energy a silicon recoil nucleus $(M/m = 28)$ can have to deposit in the detector is around 330 keV. This is small compared to the typical maximum energy (above 1 MeV) of the observed low-energy background in the presence of neutrons. Thus, the observed low-energy background cannot be attributed to elastic scattering between neutrons and silicon. To explain the spectra observed, reactions between neutron-induced γ rays and silicon, or other reactions involving neutrons will have to be invoked.

The interaction of γ rays with the silicon detector is characterized by the local γ-ray flux ϕ, the detector area A and thickness t, and the relevant reaction cross section σ. The reaction rate is given by

$$Rate = \phi A \cos \theta [1 - \exp(-N \sigma \frac{t}{\cos \theta})] , \tag{8.2}$$

where $N = 5.0 \times 10^{22}$ cm^{-3} is the number density of silicon nuclei, and θ is the angle between the direction of the γ-ray flux and the detector normal vector. The photon cross section with silicon [62] is a complicated function of the photon energy. Taking a representative value of $\sigma \sim 1$ barn $= 10^{-24}$ cm^2 and a silicon thickness of $t = 525 \pm 25$

---

[6]For ^{28}Si, which makes up over 92% of naturally occurring silicon, the (n,α) and (n,p) reactions require neutron threshold energies of 4.5–5.0 MeV [64,65] and are only possible with neutrons from triton burnup (birth energy of 14.1 MeV).
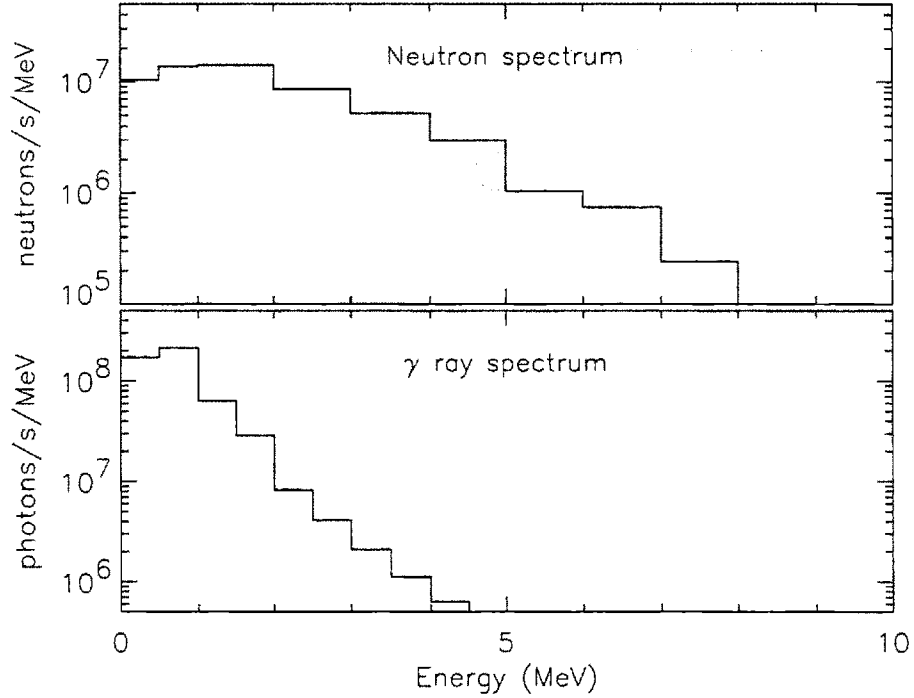
Figure 8.7: Neutron and γ-Ray Spectra of ^{252}Cf. The ^{252}Cf source had a source rate of 4.53×10^7 neutrons/s, and a corresponding γ-ray emission rate of 2.46×10^8 γ/s [66].

μm for the CFP detector, the exponent $N\sigma t / \cos\theta$ has the value of $2.5 \times 10^{-3} \ll 1$ when $\theta = 0$. Even at the acute angle of $\theta = 85°$, the exponent (2.9×10^{-2}) is still small compared to 1. This means that the attenuation of the neutron or γ-ray flux by the detector should be small in most directions. Consequently, the rate of γ-ray interactions with the detector is expected to be proportional to the volume V of the silicon in the detector because, after expanding the right side of Eq. (8.2),

$$Rate \approx \phi A N \sigma t = \phi N \sigma V .\tag{8.3}$$

This is similarly true for neutron interactions, as the neutron cross section [64] is of order a barn.

8.2.4 Experimental Investigation of Detector Sensitivity

To further explore the nature of the spectrometer's response that correlates with the neutron rate, two benchtop counting experiments were conducted. In each case, spectra were collected using a silicon detector (525 ± 25 μm thick) identical to the one in the CFP spectrometer. In the first, a ^{252}Cf spontaneous fission neutron source was used to provide both neutrons and γ rays; in the second experiment, the detector's response to a variety of γ-ray sources was investigated.

Neutrons

The ^{252}Cf source emits at rates of 4.53×10^7 neutrons/s and 2.46×10^8 γ/s. The neutron and γ-ray spectra from a ^{252}Cf source has been reported by Profio [66] and these are shown in Fig. 8.7. Though not exactly the same, the neutron spectrum bears close enough resemblance to the neutron spectrum in the tokamak environment (considering neutron scattering and moderation) that it is used in the calibration of Alcator C-Mod's neutron diagnostic system [18]. In this experiment, the effects of different detector setups were investigated. These included varying the distance between the detector and the source, changing the direction the detector faced with respect to the source, and using an additional detector with a silicon thickness of 2000, not 525, μm. Each detector was covered with a 0.13 mm stainless steel cap to shield against visible light.

Plots of the observed count rate (less background) as a function of the separation distance l between the detector and the neutron source are given in Fig. 8.8 for the two detectors used. In each plot, two sets of data are presented, one for count rates integrated for channels corresponding to $E \geq 500$ keV, and the other for channels corresponding to $E \geq 1$ MeV. Also included are the least squares fit of each set of data to a function that varies as $1/l^2$, $i.e.$, proportional to the solid angle subtended by the detector. As the separation distance l increases, the observed flux seems to exceed the $1/l^2$ dependence. This could be due to an increase in the neutron flux

159
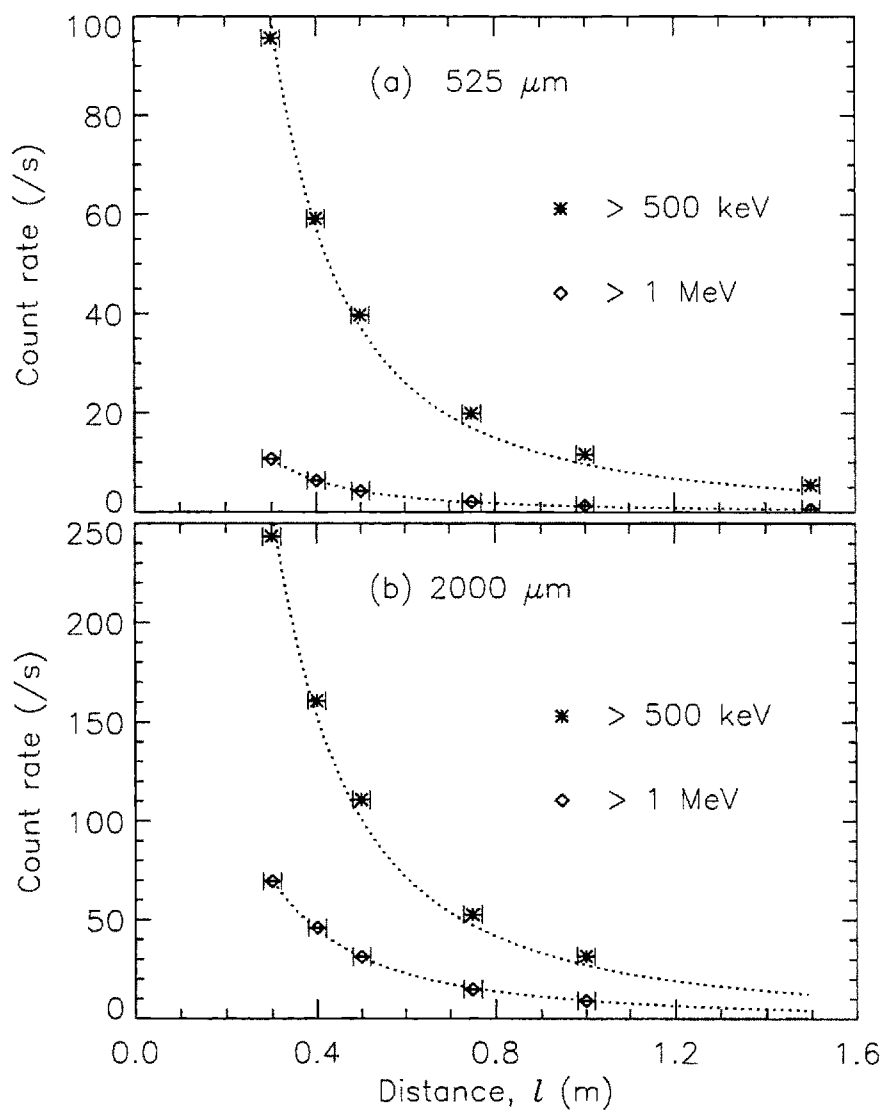
Figure 8.8: The count rate (asterisk for counts integrated over $E \geq$ 500 keV; diamond for $E \geq 1$ MeV) is plotted against the distance, l, between the silicon detector and the ^{252}Cf neutron source. Uncertainty in the count rate (not shown) is $\lesssim 1\%$ because of good counting statistics. The count rate is found to be proportional to $1/l^2$ (dotted curve).

and/or an increase in the γ-ray flux, both being consequences of the experiment's proximity to neighboring structures.[7]

One result that can be extracted from the data is the effective detection efficiency, assuming the $1/l^2$ dependence. If we consider that the response is purely due to neutrons, which are being emitted at 4.53×10^7 neutrons/s, the effective detection efficiency (including only counts for $E \geq 500$ keV) is 2.8% for the 525 μm detector and 7.2% for the 2000 μm detector. However, if the response is in fact exclusively due to γ-ray reactions, then the measurement suggests that the effective γ-ray detection efficiency (including only counts for $E \geq 500$ keV) is only 0.5% for the 525 μm detector and 1.3% for the 2000 μm detector, since the emission rate of γ rays is higher. Note that from the discussion in §8.2.3, the detection efficiency is expected to be directly proportional to the silicon volume, which would suggest a value about 3.8 times as high for the larger detector. Here, the ratio is found experimentally to be 2.6.

In another experiment with a pure γ-ray source, the γ-ray detection efficiency can be measured. If it is found to be around 0.5%, that proves that the detector's response in a neutron-rich environment is really due to the associated γ rays; if it is much less, then some other explanation has to be sought to explain the detector's response. Alternatively, these results can be used in conjunction with the local neutron flux and γ-ray flux to evaluate the detector's response to the neutron environment of Alcator C-Mod during a D-D plasma discharge. The calculated response from such a calculation, however, will only be accurate to within an order of magnitude or so because: 1) the D-D neutron spectrum and the neutron spectrum from the ^{252}Cf source are not the same, and 2) this calculation relies heavily on simulation calculations in determining the neutron and γ-ray fluxes.

The results from rotating the 525 μm detector at the distances of $l = 0.5$ m and $l = 1$ m are plotted in Fig. 8.9. Considering that the detector lies on the surface of

---

[7]In order to minimize the author's accumulated neutron dose, the neutron source was held in its storage compartment during the experiment, allowing the simplest handling procedure of all. This was located about 20 cm from a concrete wall, which acted as a neutron scatterer.
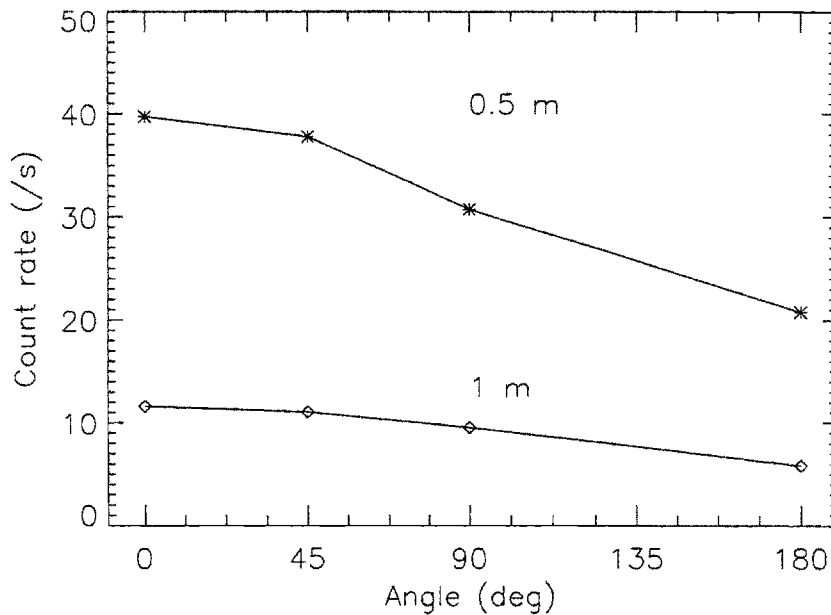
Figure 8.9: The count rate, integrated over $E \geq 500$ keV, from the ^{252}Cf source is at a maximum when the source is directly facing the detector (0°), and at a minimum (nearly 50%) when the source is facing the back of the detector (180°). This is unexpected for neutron interaction with silicon, and points strongly toward the possibility that γ rays dominate the response observed.

a sphere of radius l with the source at the center, an angle of 0° corresponds to the detector facing radially inward, 90° to the detector facing the direction of a tangent to the sphere, and 180° to the detector facing radially outward. At 90°, there is a layer of gold-plated stainless steel (the detector holder) between the source and the silicon; and at 180°, there is also the cable connection in the back of the detector that is in the way. For both locations, the count rate is measured to drop from a maximum level at 0° to a 95% level at 45°, to around 80% at 90°, and 50% at 180°. Intervening matter between the source and the silicon active volume is expected to affect γ rays more than neutrons. The observation, thus, supports the possibility that the detector's response is dominated by γ rays.

162

In this experiment, the sensitivity of the 525 μm detector to different energy γ rays was investigated. Different sources (listed in Table 8.2) were used for this counting experiment to survey the detector's response to γ rays of different energies. Each nuclide emits γ rays at a characteristic energy which is the result of the nuclide's decay to some daughter nuclide and the daughter nuclide's transition between different energy states. Each source was placed directly in front of the detector, whose face was covered with two layers of aluminum foil (total thickness of about 35 μm) to shield against visible light. The distance between the detector and each source was fixed such that 9.0% of the γ rays emanating from the source went through the detector.

Table 8.2: List of γ-ray sources, their activities, the major photon emissions and the intensities (percentage of the activity).

Nuclide	Activity μCi	E_γ (Intensity) MeV
^{60}Co	2.9	1.173 (100%), 1.333 (100%)
^{22}Na	1.7	1.27 (100%), 0.511 (90%)
^{54}Mn	0.13	0.836 (100%)
^{137}Cs	6.9	0.662 (85%)

For each source, the detected spectrum, normalized to per γ ray incident on the detector, is shown in Fig. 8.10. The effective detection efficiency (once again, only including counts for $E \geq 500$ keV) ranges from 0.4% for 1.2–1.3 MeV γ rays to less than 0.02% for 0.66 MeV γ rays. Without a source of γ rays at yet higher energies, the detector's response to higher energy γ rays is not found in this experiment. The order of magnitude of the response to $\sim$1 MeV γ rays agrees well with the result from the experiment with the ^{252}Cf source, assuming the detector's sensitivity is predominantly due to γ rays and not neutrons *per se*.
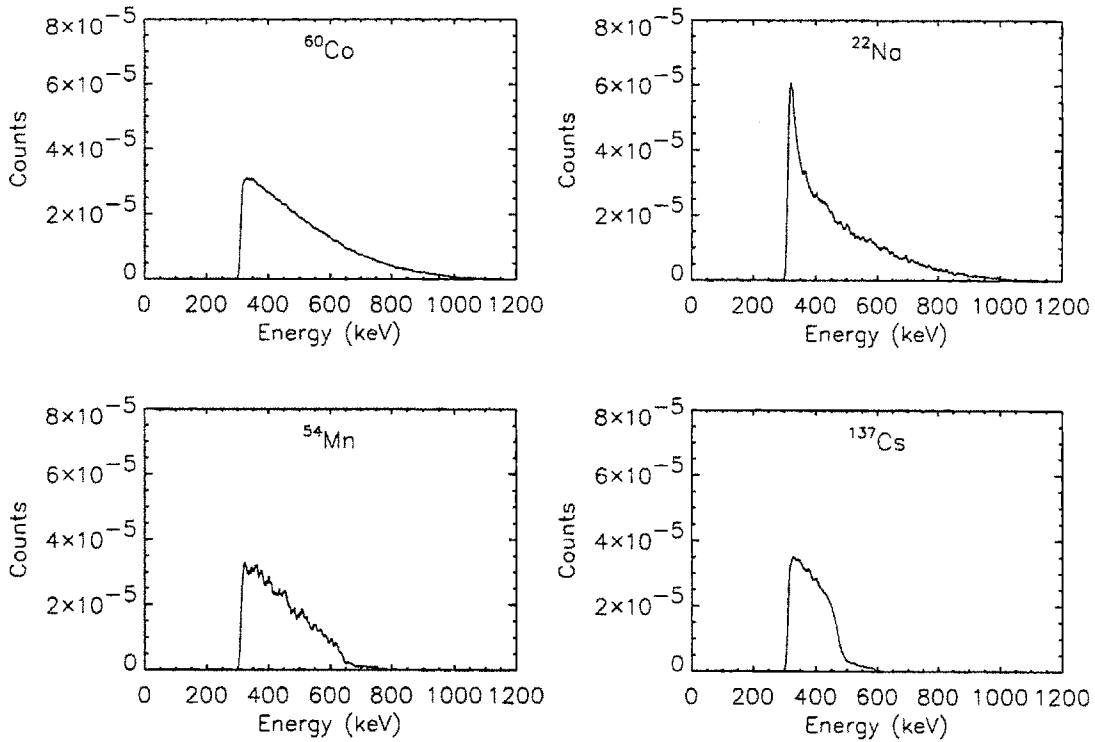
Figure 8.10: Spectra of γ rays from the sources listed in Table 8.2 collected by the 525 μm detector. They are normalized to per γ ray incident on the detector. There are 1000 channels for every 916 keV.

8.2.5 Detector Response

The response of the CFP spectrometer and the monitor system in the neutron environment of Alcator C-Mod hinges on the knowledge of the local neutron and γ-ray fluxes. These have been calculated via the Monte Carlo Neutron and Photon Transport (MCNP) code [63]. The source used in the MCNP calculations was 99% D-D (2.5 MeV) neutrons and 1% D-T (14 MeV) neutrons distributed uniformly in a torus with a minor radius of 10 cm located at the nominal major radius ($R_0 = 67$ cm) of the plasma. The geometry in the computer modelling included the major Alcator C-Mod structural components (like the horizontal and vertical ports, the toroidal and poloidal field magnets, the steel covers, and the borated concrete igloo) and the con-
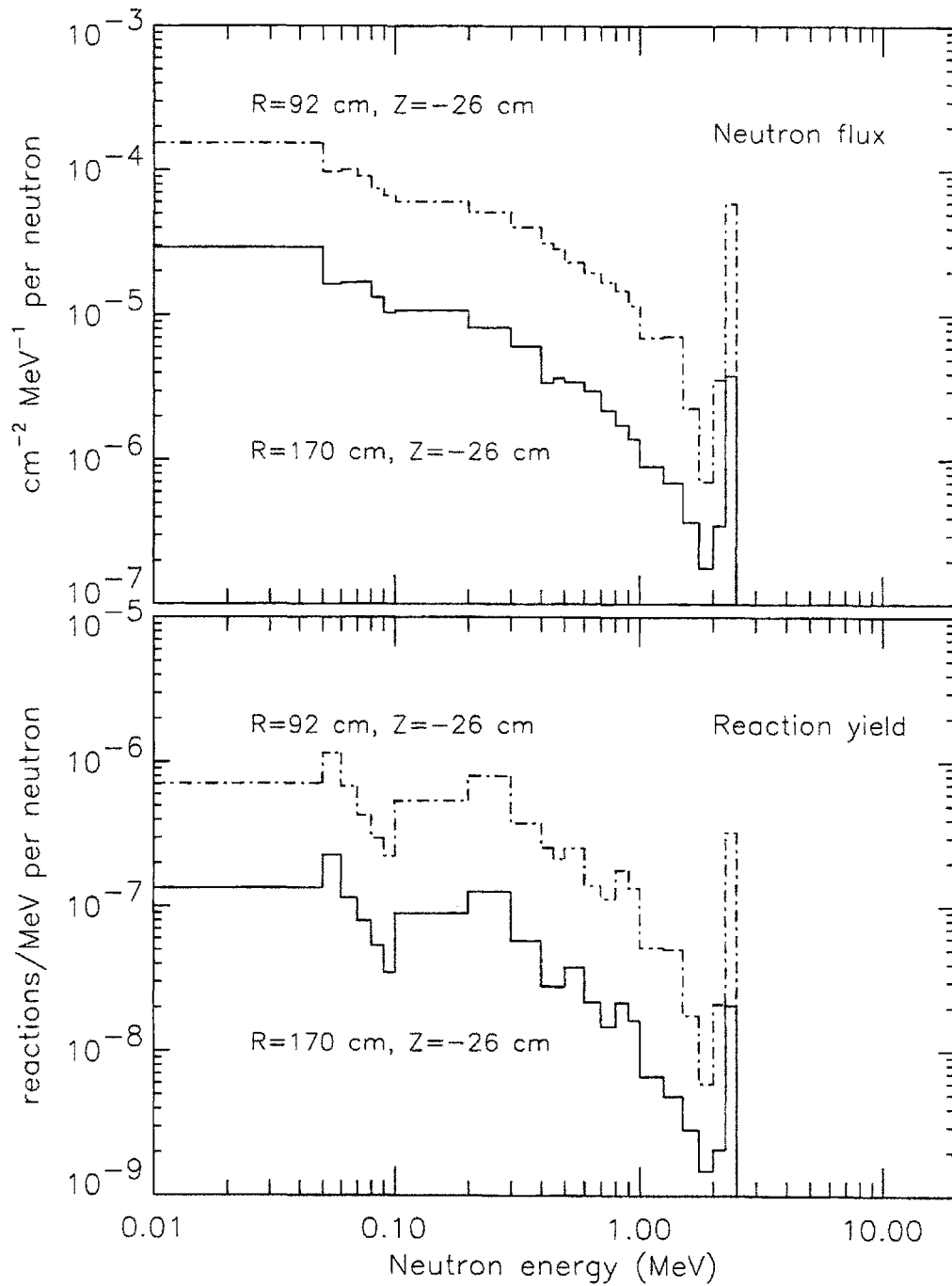
Figure 8.11: MCNP-calculated neutron fluxes and elastic collision yields at the locations of both the CFP spectrometer and the detector of the monitor system.
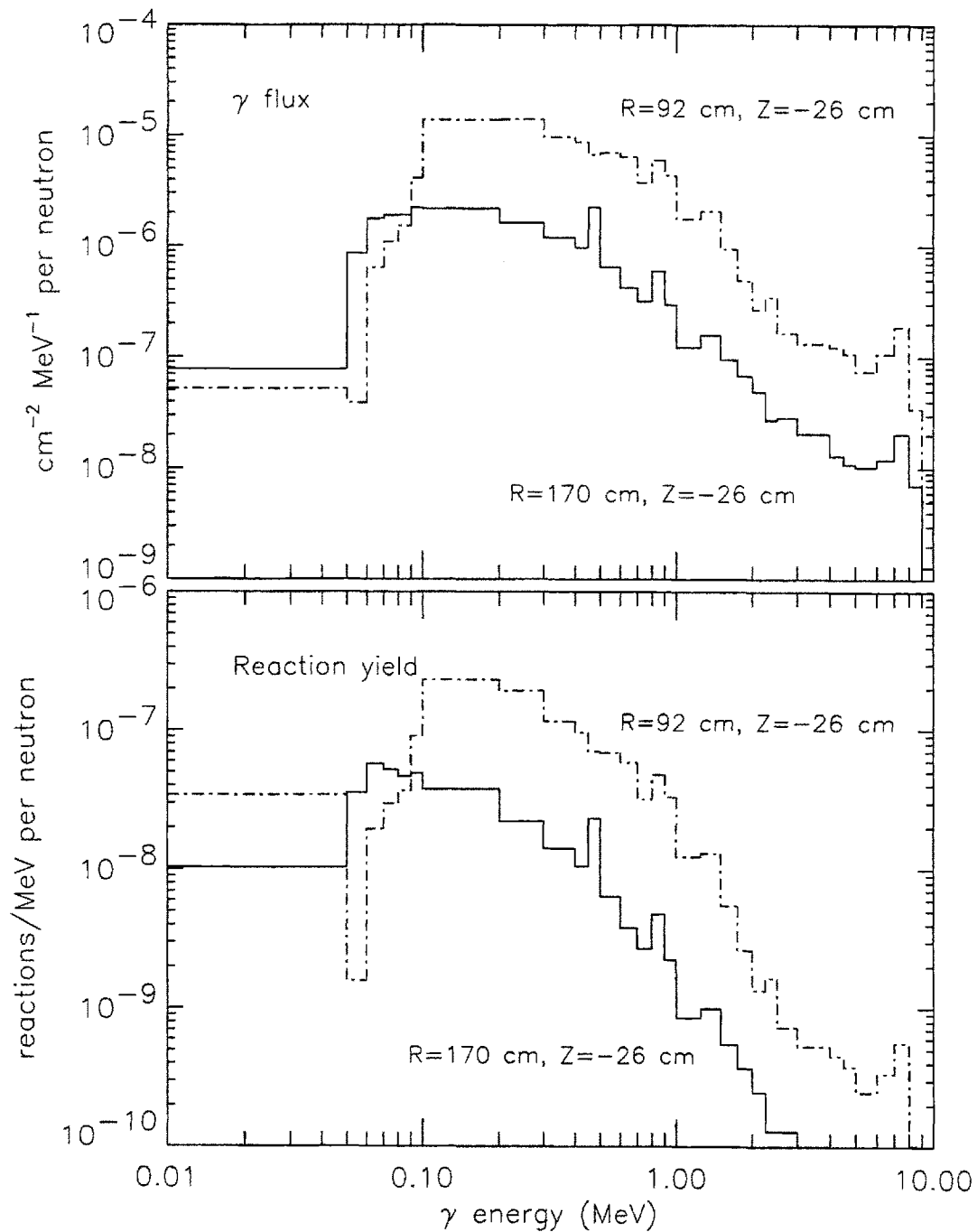
Figure 8.12: MCNP-calculated γ-ray fluxes and reaction yields at the locations of both the CFP spectrometer and the detector of the monitor system. Above 50 keV, Compton scattering dominates over all other reactions.

crete walls of the experimental cell. However, the detailed internal hardware within the vacuum vessel (first wall tiles and vacuum hardware) and the various diagnostic systems around the machine have not been included.[8] The model was originally prepared for investigating the neutron flux for the neutron diagnostic system, which is comprised of four sets of neutron detectors at various locations around the tokamak [67]. Whereas the omission of the internal vacuum hardware may have negligible effect on the primary neutron flux at those neutron detector locations, it is expected to have an influence on the secondary γ-ray flux around the CFP spectrometer and the monitor system. Therefore at this point, the uncertainties in the calculated γ-ray flux can be of the same order of magnitude as the calculated flux itself.

The code yields the neutron flux and γ-ray flux per source neutron within discrete energy bins at any given location. It also calculates for each energy bin the number of some specified reaction(s) having occurred per unit volume per source neutron. Figure 8.11 shows the calculated neutron flux and the occurrence of elastic scattering events as a function of the neutron energy, at the locations of both the CFP spectrometer ($R = 92$ cm, $Z = $ -26 cm) and the monitor system's detector ($R = 170$ cm, $Z = $ -26 cm). Similarly, Fig. 8.12 shows the calculated γ-ray flux and the occurrence of γ-ray interactions as a function of the γ-ray energy. The photoelectric effect, Compton scattering, and pair production are all considered in obtaining Fig. 8.12. A summary of some of the calculated fluxes is included in Table 8.3.

These MCNP calculations indicate that the overall flux level of γ rays is lower than that of neutrons by about an order of magnitude. Moving from the CFP spectrometer location to the location of the monitor system's detector, the 2.5 MeV neutron flux has dropped by 94%, while the overall integrated flux has dropped by 85%. Similarly, the overall γ-ray flux has dropped by 87% according to the calculations. The overall

---

[8]A possibly significant omission in the modelling is the 1.27-cm thick stainless steel tube that was added around the CFP spectrometer for the 1995-96 campaign. Taking the geometry of the tube into consideration, the drop in the transmission of 1 MeV γ rays is estimated to be around 25%. Comparison of the spectrum due to neutrons/capture-γ-rays before and after the installation of the stainless steel tube shows actually a slight increase (around 10% for counts above 0.5 MeV) in the spectral response. (Refer to Table 8.1.)

167

Table 8.3: Tabulated summary of the calculated neutron and γ-ray fluxes at the CFP spectrometer location and the location of the monitor system. Fluxes are in unit of cm^{-2} per source neutron.

	CFP system	Monitor system
ϕ_n (overall)	6.4×10^{-5}	9.2×10^{-6}
ϕ_n (2.5 MeV)	1.5×10^{-5}	9.5×10^{-7}
ϕ_n (> 0.5 MeV)	2.9×10^{-5}	2.8×10^{-6}
ϕ_γ (overall)	9.6×10^{-6}	1.2×10^{-6}
ϕ_γ (> 0.5 MeV)	5.0×10^{-6}	4.5×10^{-7}

shapes of both flux distributions (Figs. 8.11 and 8.12) for energies above 0.1 MeV experience little change between the two locations, aside from a general depression in the overall magnitude for the detector farther from the plasma. The γ-ray flux and the resulting reaction yield, in particular, are seen to generally increase with decreasing energy in the region above 0.1 MeV. This is not inconsistent with the general shape of the silicon detector's low-energy background spectrum.

Table 8.4: Tabulated summary of the calculated number of silicon/γ-ray reactions at the CFP spectrometer location and the location of the monitor system for a neutron yield of 10^{12} neutrons.

		CFP system	Monitor system
MCNP:	> 0.1 MeV	9.8×10^4	1.2×10^4
	> 0.5 MeV	3.6×10^4	3.1×10^3
	> 1 MeV	1.2×10^4	1.1×10^3
C-Mod (from Table 8.1):		5.0×10^4	7.1×10^3

We concentrate first on the γ-ray reactions to explain the observed spectrum. For a D-D neutron yield of 10^{12} neutrons, the number of reactions calculated are compared with the number that was experimentally determined (summarized in Table 8.4). Shown in the top block are the number of silicon/γ-ray reactions directly calculated by MCNP for γ rays of all energies, those with energy above 0.5 MeV, and those above 1 MeV. These are followed by the expected number of counts above 0.5 MeV

in the spectrum in accordance with the observed response listed in Table 8.1 based on data from C-Mod plasma discharges. A reasonable comparison can be made using the number of reactions calculated with MCNP for γ rays with energy above 0.5 MeV. Lower energy γ rays are not expected to contribute to the detected energy spectrum. For the CFP spectrometer, the calculated 3.6×10^4 counts compare well with the measured 5.0×10^4 counts found in C-Mod. In the case of the monitor system, the calculated 3.1×10^3 counts are 44% of the measured 7.1×10^3 counts. Considering the substantial uncertainty in the calculated γ-ray fluxes, it is not unreasonable to conclude that the observed counts in the energy spectrum (above 0.5 MeV) are due to γ-ray interaction with the silicon in the detector.

Counts below the low-energy cutoff in the collected spectrum correspond to energies that are below 0.5 MeV. (Recall that the monitor scaler collects about 2.3×10^4 counts for every 10^{12} neutrons created by fusion.) These are believed to be partly due to γ-ray interactions and partly due to recoil silicon nuclei from neutron elastic collisions. In particular, considering just 2.5 MeV neutrons alone, for a fusion neutron yield of 10^{12} neutrons, MCNP calculates that there are 5.2×10^3 elastic collisions in the monitor system's detector, and 8.2×10^4 in the CFP spectrometer. There are also considerable γ-ray reactions in the silicon (see Table 8.4) due to γ rays with energy below 0.5 MeV, thus contributing to the overall number of events.

Another contributing factor to counts observed in the spectrum is the pile-up effect on counts from neutron elastic scattering with silicon. Individual elastic scattering events from 2.5 MeV neutrons produce silicon recoil nuclei with a highest possible energy of around 330 keV. However, when the neutron count rate is high, the probability that two such neutron events occur so close in time that they are interpreted as a single event can become significant. The severity of these peak pile-up events can be estimated from the 2.5 MeV neutron reaction rate in the silicon and the peak-detection time of the MCA.[9]

---

[9]Note in Fig. 8.11 that for neutron energy $\gtrsim 1$ MeV, the 2.5 MeV neutrons dominate. Yet, using just the neutron reaction rate in this calculation is an approximation. The population of silicon

The degree of pile-up can be evaluated using Poisson statistics by finding the probability $P(0)$ that no event is recorded over an interval of length t, given by

$$P(0) = \frac{(rt)^0 exp(-rt)}{0!} = exp(-rt) \,, \tag{8.4}$$

where the average rate of events is r. To avoid pile-up, the interval following an event must be greater than the peak-detection time, which was set at 1 μs. In the case of a fusion neutron rate of 10^{12} neutrons/s, MCNP calculated that r is 8.2×10^4 /s in the CFP spectrometer and 5.2×10^3 /s in the monitor system. The corresponding probability that pile-up does occur is $1 - P(0)$, which is 8% in the CFP spectrometer and less than 0.5% in the monitor system. Therefore, pile-up adds more than 6500 counts to the CFP spectrometer, but only around 27 counts to the monitor system. Compared to the values discussed in Table 8.4, this is a significant addition to the CFP spectrometer's spectrum and not so important for the monitor system's. (Note that for a fusion neutron rate of 10^{13} neutrons/s, *i.e.*, a factor of 10 increase, this becomes 4.6×10^5 additional counts in the CFP spectrometer and 2600 in the monitor system.)

In summary, the correlation between the undesired low-energy counts and the neutron yield in C-Mod has been shown, and these counts are attributed to both elastic collisions of neutrons and interactions of γ ray (from neutron capture) with the silicon detector. However, events that deposit more than 0.5 MeV (per event) in the silicon detector are the result of γ-ray interactions with the silicon detector alone.

---

recoil nuclei from elastic collisions with 2.5 MeV neutrons is uniformly distributed in the energy spectrum from 0 to 330 keV [29]. So clearly, not all possible recoil-recoil pileup events add counts to the detected spectrum above 0.5 MeV. On the other hand, pile-up can also occur between a neutron elastic scattering event and a γ ray Compton scattering event where the Compton electron originally has less than 0.5 MeV, or two such Compton scattering events.

8.3 No ICRF Pickup

There is no evidence of any ICRF pickup by the CFP spectrometer system. During run 950510 dedicated for studying ICRF mode-conversion heating where there was essentially no deuterium in the hydrogen/^{3}He plasma, the launching of ICRF waves into the plasma did not result in any counts collected by the CFP spectrometer. During other runs when ICRF was used to heat deuterium plasmas, correlation between the CFP spectrometer's signal and the ICRF power absorbed could be attributed to the corresponding changes in the fusion neutron rate. Time traces already shown in Fig. 8.5(a)–(d) are examples of such a neutron effect.

8.4 Electronics

The detector's sensitivity to high-energy photons and neutrons is problematic really because the electronics of the system are limited in their signal processing capabilities. The fact that pulses from detected events are randomly spaced in time can lead to interfering effects between pulses when the count rate is high. For the electronics used in the CFP spectrometer, a conservative count rate limit for optimal spectral resolution is about $(1-1.5) \times 10^4$ counts/s. Going over this rate results in undesirable spectral degradation and growing loss of counts and correction has to be made in the analysis of the spectra. These include the deadtime correction discussed in §4.5, and the linewidth correction in calculating the ion temperature as described in §7.3.1. An ultimate counting limit is about 10^5 counts/s. At such a count rate, not only has very severe spectral degradation been taking place, the apparent count rate is really a small fraction of the real count rate experienced due to the system's deadtime. The system is really at the brink of saturation, and very little useful information about the various events generating counts in the system is preserved or retrievable.

During the last few campaigns, Alcator C-Mod's fusion neutron rate ranged from around 10^{11} to above 10^{13} neutrons/s. (The projected rate in future campaigns is as
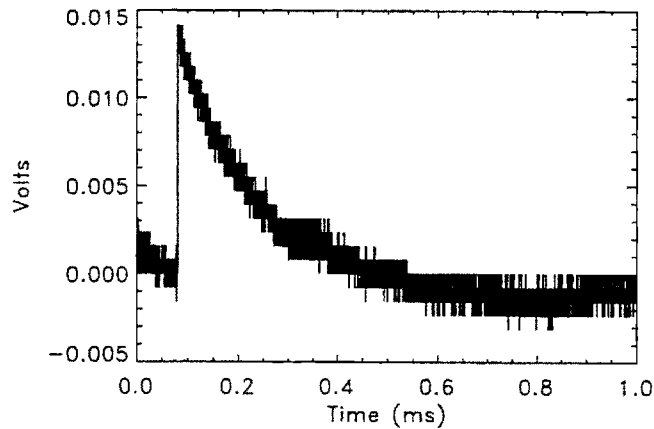
Figure 8.13: The preamplifier output pulse (captured during discharge 950324012) has a short rise time and a long decay time.

high as 10^{16} neutrons/s.) The problem is that, as outlined in §8.2, for a neutron rate of 10^{12} neutrons/s, the CFP spectrometer has to process over 5×10^4 counts/s due to γ rays alone.[10] This undesirable and yet unavoidable count rate is already a few times the aforementioned conservative limit. In Chapter 7, it has been found that a satisfactory ion temperature measurement is only achievable when the neutron rate stays below about 0.4×10^{12} neutrons/s. At a high neutron rate, the spectral peak of D-D protons is severely broadened and downshifted in energy. And in the fusion rate measurements discussed in Chapter 6 (Fig. 6.8), no global fusion proton rate above 6×10^{12} s^{-1} was presented. The reason is that no useful spectral information can be obtained from the D-D protons at such high rates. In the following, the different components in the chain of electronics (*i.e.*, the preamplifier, the shaping amplifier, and the multichannel analyzer) are examined to evaluate the problem that each has at a high count rate.

---

[10]In some sense, it is as if the CFP spectrometer has an inherently unavoidable "γ-ray/fusion-neutron" detection efficiency of about $5 \times 10^4/10^{12} = 5 \times 10^{-8}$.

8.4.1 Charge Sensitive Preamplifier

The charge sensitive preamplifier is the interface between the detector and the pulse processing and analysis electronics that follow. The preamplifier provides a high impedance to the detector to minimize loading and a low impedance output to drive the pulse processing and analysis electronics that follow. Intermediate pulse amplification takes place, where the output voltage is proportional to the total integrated charge in the input signal pulse from the detector. The output pulse has a short rise time, consistent with the charge collection in the detector, but a long decay time, typically $\sim 200~\mu s$ (see Fig. 8.13). The typical pulse height is ~ 10 mV.

Because its output pulse has a long decay time, it is possible for the charge sensitive preamplifier to saturate when the count rate becomes very high and the pulses are large. As the average count rate increases, the likelihood that a pulse may arrive before a previous pulse has decayed back to zero increases. At times, the preamplifier saturation level of 12 volts may be exceeded. This can result in severe pulse distortion in a marginal case; in the more severe case, the preamplifier can remain in saturation for a prolonged period until the waveform drops back to below the saturation level. However, it is more likely that the shaping amplifier saturates before the preamplifier does.

8.4.2 Shaping Amplifier

One problem at high count rate that can take place in the amplifier is the baseline shift of the amplifier output signal. Because capacitors cannot conduct direct current, the average dc voltage of any point downstream from the capacitor in a differentiating network must be zero. (If the dc voltage were nonzero, a finite dc current must flow through the rest of the network to ground. But since any such current would have to come through the capacitor, this is physically impossible.) Therefore, the apparent baseline on which the amplifier output pulses lie is depressed below the "true" zero level such that the areas enclosed by the output waveform above and

173

below the zero axis are equal. The higher the pulse rate, the larger this baseline shift becomes. The result of such a baseline shift is the energy downshifting of the spectrum. The fluctuation of the count rate on top of the baseline shift contributes also to the broadening of spectral peaks.

The amplifier can also saturate totally when the count rate is high. This is related to the amplifier's current limit, and so is a function of the instantaneous count rate and individual pulse heights, which typically are a few volts. Such cases of saturation manifest themselves as periods during which the apparent count rate is zero. The observed upper count rate limit for our mode of operation has been about 2.5×10^5 counts/s.

8.4.3 Multichannel Analyzer

Interfering effects between pulses when the count rate is high also affects the interpretation of the amplifier output pulses. The phenomenon, generally referred to as pulse pile-up, occurs when two pulses are sufficiently close together (less than 1 μs apart in the case of the CFP spectrometer system) that they are treated as a single pulse by the MCA. The combined pulse has an amplitude that is the sum of the amplitudes of the two individual pulses, *e.g.*, two 3 MeV D-D protons giving a single pulse at 6 MeV.

The more common D-D proton pile-up event, however, involves the low-energy background. Most of the time, the desired count rate of D-D protons does not exceed 15000 counts/s. This can be achieved by pre-adjusting the aperture size for the type of run. However, the rate of the neutron-induced reactions in the detector (discussed earlier in §8.2) cannot be controlled as the CFP spectrometer is fixed. Therefore, when the neutron rate is high, the neutron-induced low-energy background count rate can be higher than the proton count rate. The resulting pile-up effect on the D-D proton peak is that it is more likely to have pile-up between a proton event and a low-energy neutron-induced background event than between two proton events. The

174
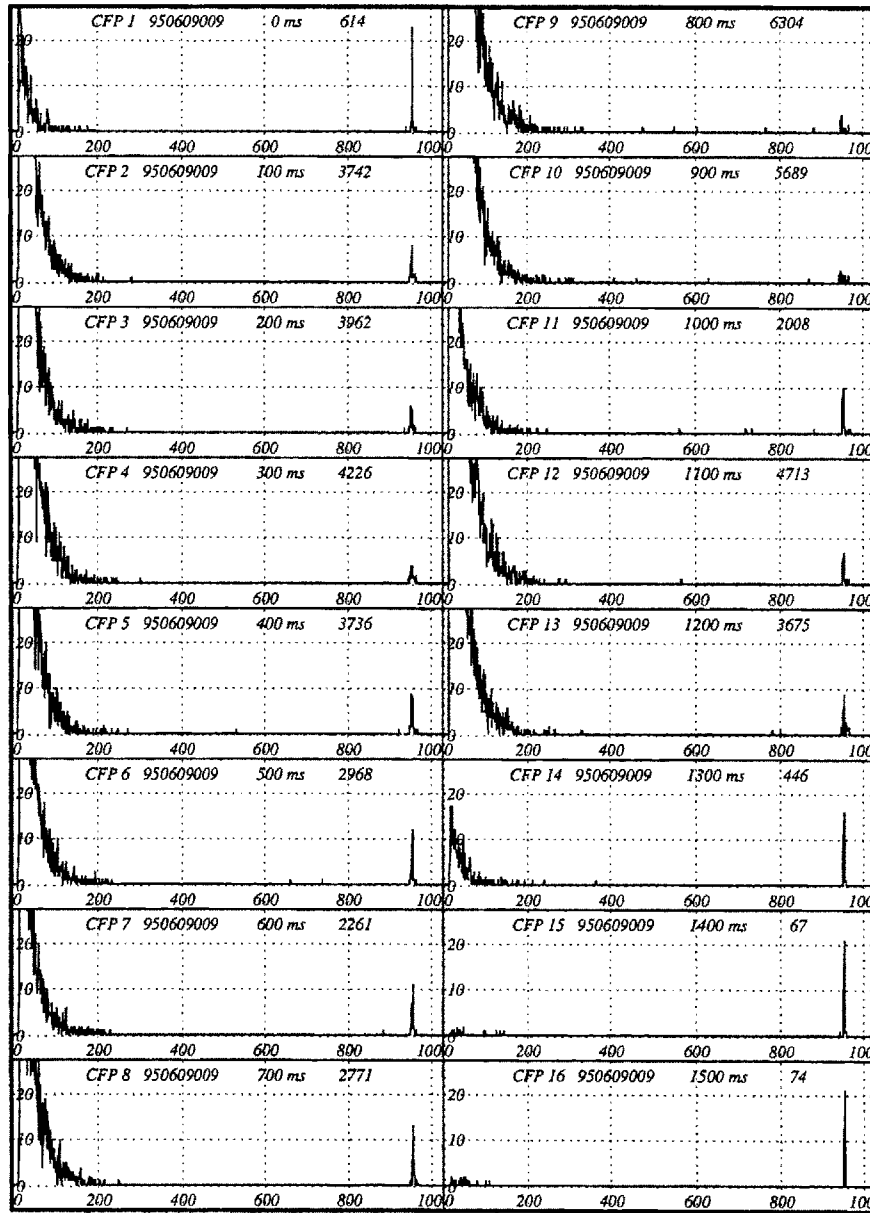
Figure 8.14: Successive monitor system spectra (each 100 ms long) from a single C-Mod discharge showing background (below channel 400) and pulser counts (about channel 950). At the top of each spectrum are listed the spectrum number, the shot number, the starting time of integration, and the overall number of counts. Notice that the broadening of the pulser peak is count rate related, as can be seen from the overall number of counts.

175

summed pulses translate to counts that appear on the high-energy side of the proton peak in the energy spectrum.

As demonstrated in §4.5, the overall dead time of the spectrometer system is not more than 7 μs and is due to the multichannel analyzer (MCA). (This has been demonstrated independently on the bench as well.) This is the time that the MCA requires to properly process the information of a detected event. This means that the system can tolerate a purely periodic pulse rate of about 1.4×10^5 counts per second without any loss in throughput. With pulses from the detector arriving in irregular intervals, compensation for pulses lost between the shaping amplifier and the MCA due to its dead time is required at count rate far lower than this ideal limit. This correction, *i.e.*, Eq. (4.1), has been consistently applied to the data presented in this thesis.

8.4.4 Overall High Count Rate Scenario

Since all these components of the electronics are interconnected, high count rate tends to bring about a combination of these effects. The general changes to a CFP spectrum with both a D-D proton peak and a pulser peak is as follows. At moderately high count rates, $\sim$ 10000–15000 counts/s, effects like spectral broadening and pile-up with subsequent losses of counts begin to appear. A collection of successive spectra collected with the monitor system is included in Fig. 8.14 as an example to illustrate the count rate dependence of spectral broadening. Ideally, the peak due to the pulser signal should have a FWHM of between 2 and 3 channels centered at about channel 950. The background counts shown changed from being dominated by hard x rays (0–700 ms) to being neutron dominated. Broadening of the pulser counts were the most severe in spectra 9 and 10 when the total count rate was the highest.

When the count rate goes above around 50000 counts/s, spectral energy downshift owing to the baseline shift in the amplifier usually starts becoming a problem. These problems deteriorate with increasing count rate. At the same time, depending on the

176

instantaneous detection efficiency of CFPs, the low-energy background from neutron-induced events or hard x rays may become dominant in the energy spectrum. If that is the case, the proton peak and pulser peak start disappearing from the spectrum altogether, because most of these counts are removed from under their respective spectral peaks because of pile-up or dead time problems. In the extreme case of over 10^5 counts/s, the amplifier suffers from a complete saturation which can last for hundreds of ms.

In light of the behavior of the electronics at high count rate, the development of the CFP spectrometer as a plasma diagnostic has been greatly hampered. In terms of measuring the fusion rate, the spectrometer performs well, with corrections applied, up to a neutron rate of around $(5-6) \times 10^{12}$ /s. On the other hand, only when the neutron rate remains below about 0.4×10^{12} /s can a satisfactory ion temperature measurement be made. When the neutron rate is significantly above 10^{12} /s, which is the case for any typical ICRF-heated plasma, great distortion of the spectrum sets in.

Chapter 9

Summary and Future Work

9.1 Summary

This thesis has discussed the development and experimental results of a charged fusion product (CFP) spectrometer for the Alcator C-Mod tokamak. Based on an ion-implanted silicon detector, the spectrometer has a reentrant design that brings the detector inside the vacuum vessel of Alcator C-Mod for intercepting charged fusion products. For the sake of calculating the CFP detection efficiency, a 3-D orbit-following code, EPSILON, has been written.

The detection of D-D protons has made possible the independent measurements of the fusion rate in Alcator C-Mod. These fusion rate measurements are also compared to those measured with the neutron diagnostic system. The plasma current dependence of the detected D-D proton flux has been presented. From the measured D-D proton linewidths in the energy spectrum, central ion temperature measurements have been made in ohmic discharges. These were found to compare well with the temperature measurements made by both the neutron diagnostics and high-resolution x-ray spectrometer (HIREX).

The usefulness of the CFP spectrometer in measuring the fusion rate and in making temperature measurements was discovered to be limited. This is due to competing

179

signals that populate the low-energy region of the spectrum. The number of these counts was found to be proportional to the neutron rate. Given the finite counting capability of the electronics, these counts dominate at high neutron rates. Consequently, fusion rate measurements have been possible for discharges with neutron rate of up to about 6×10^{12} /s, whereas satisfactory ion temperature measurements have been restricted to cases where the neutron rate is below 0.4×10^{12} /s. Through two benchtop experiments and MCNP modeling of the neutron and γ ray fluxes in C-Mod, these interfering low-energy counts were identified to be due to neutron-capture γ rays and fusion neutrons permeating the detector during a discharge. Counts from γ-ray interactions can have energy extending to a few MeV, while neutron interactions primarily result in counts with an upper energy limit of about 330 keV. Pile-up of these neutron events do contribute to counts at higher energy, and the importance of pile-up rises with an increasing global fusion neutron rate.

9.2   Further Investigation

In view of the count-rate related problems that the spectrometer faced, ways of dealing with the tremendous response to γ rays and neutrons have to be devised for this diagnostic technique to be useful for a wider range of fusion yields. The compactness of C-Mod prevents the moving of the spectrometer away from the plasma as a solution for the simple reason that no CFPs can reach the spectrometer then.

One obvious way to alleviate the deleterious effects of γ rays and neutrons on the spectrum is to reduce the active volume of the silicon detector. In §8.2.4, it has been demonstrated that the detector's response to γ rays and neutrons scales roughly with the detector's volume. By reducing both the area and the thickness of the silicon, the detection efficiency for charged fusion products (governed by the choice of aperture) will not be altered while the undesirable "detection efficiency" for γ rays and neutrons can be greatly reduced.

Another way to counter the problem is to optimize the counting capabilities of

the electronics. Components like a pile-up rejecting circuit and a baseline restorer should be added to the electronics. The present electronics have an optimal counting limit of about 10000–15000 counts/s, and an ultimate counting limit of about 10^5 counts/s. The corresponding processing time of 10 μs is in sharp contrast with the typical charge collection time of $\sim$1–10 ns. Faster electronics (especially the MCA and shaping amplifier), if available, will extend the present count-rate limit.

Local shielding against γ rays is a remote possibility as a remedy but it is still worth investigating. (Shielding against neutrons is impossible in the tight configuration of C-Mod.) Careful modeling work will have to be performed with MCNP to find a combination of materials that can fulfill the following objectives: 1) The shield should bring about a net reduction in the γ ray flux at the detector. Both the attenuation of the γ ray flux from outside this shield, and the neutron capture reactions that can take place within the shield itself have to be considered. 2) The shield must be compact for the implementation to be practical. 3) The materials chosen must also satisfy stringent vacuum, structural, high-temperature, and other plasma-related requirements.

Appendix A

The Cluster-Impact Fusion Debacle

Beuhler, Friedlander, and Friedman of the Brookhaven National Laboratory published findings in 1989 in Physical Review Letters, [68] and again in 1990 in the Journal of Physical Chemistry, [69] on an anomalous phenomenon which they named cluster-impact fusion. The anomaly, great news if it were true, is that by bombarding deuterated targets with $(D_2O)_N^+$ clusters (N $\sim$ 25-1000) accelerated to $\approx$325 keV [i.e. $\approx$0.3 keV lab energy for D in $(D_2O)_{100}^+$], they recorded fusion rates that were around 25 orders of magnitude higher than can be explained through conventional established nuclear physics. After closer examination of their data, it became clear that the presence of light-ion-beam contaminants (e.g. D^+ of order 100 keV) had not been ruled out. The presence of such contaminants in their "cluster" beam can certainly explain their observations. Therefore, we were able to refute their claims. This work is another case illustrating the information available through the analysis of an energy spectrum.

Spectral Linewidth

Beuhler *et al.* showed D-D proton peaks ($\approx$3 MeV) with widths (FWHM) of about 330 keV obtained with a surface barrier detector (SBD) [68,69]. Beuhler *et al.* [68] attributed this width to differential energy loss of 3-MeV protons passing through the
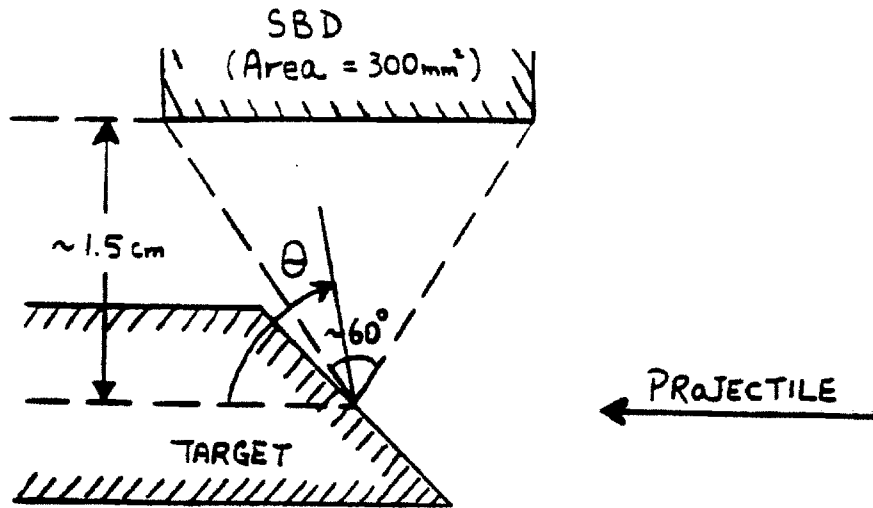
Figure A.1: Geometry of the experiment by Beuhler, Friedlander, and Friedman. In their experiments, the cluster beam hit a deuterated target ~1.5 cm from a 300-mm^2 SBD. Thus the SBD subtended an angle (at its extreme) of about 60°.

50-μg/cm^2 Al front layer of the SBD at various angles. However, we calculated this effect to be only ~1 keV [35]. Broadening due to energy straggling is ~5 keV [28]. About 20 keV is the electronic detector noise specified by the manufacturer; however, in our experience, ~50 keV is easily obtained. Thus, a broadening of still ≈330 keV must be attributed to some other process, which we discuss henceforth.

In Beuhler *et al.*'s experiments, the cluster beam hit a deuterated target ~1.5 cm from a 300-mm^2 SBD (Fig. A.1). Thus, the SBD subtended an angle (at its extreme) of about 60°. The D-D proton energy in the lab frame depends on the D-D center-of-mass velocity (a function of the initial D energy) and the angle (θ) between the proton and the initial deuteron directions (see Table A.1 and Fig. A.1). From Table A.1 and the linewidth of the proton peak collected by Beuhler *et al.*, we concluded that the fusing deuterons had a lab energy of $\gtrsim$50 keV. (A smaller *effective* angle, which should apply to Beuhler *et al.*'s experiments, would imply a higher energy, thus the ">" in $\gtrsim$50 keV.)

Table A.1: D-D proton energy (MeV) depends on the D-D c.m. velocity (a function of the D lab energy, E_D) and the lab angle, θ (Fig. A.1). ΔE_p is the energy (MeV) range of protons collected by an SBD at 90° when it subtended an angle of $\approx 60°$, a value appropriate for the experiments of Beuhler *et al.*

E_D (keV)	1	10	50	100	200	300
ΔE_p (keV)	.039	.123	.276	.391	.554	.683

Charged Particle Interaction with Matter

As a test for beam contaminants, Beuhler *et al.* argued that ranging their cluster beam through 500 $\mu g/cm^2$ of Au would eliminate "cluster fusion" but not light-ion contaminant fusion (from D^+, D_2^+, D_3^+). This argument is not generally valid. A contaminant of, *e.g.*, ~ 100 keV D^+ would indeed penetrate 500 $\mu g/cm^2$ of Au; however, it would lose 70 keV in ranging through [58], and the fusion yield would be reduced by ~ 20 times. [The same reduction in fusion yield holds for D_2^+ (D_3^+) at ~ 200 keV (300 keV).] Indeed Beuhler *et al.* did observe in such an experiment very roughly an order of magnitude decrease in the fusion rate (the experiment statistics were poor), but they interpreted this as proof that light contaminants were not causing their observed rate. [69,70] (They invoked this non sequitur again in a later paper.)We disagree. Furthermore, while Beuhler *et al.* believed they had eliminated oxygenated light contaminants from the ion source up to the first stages of their accelerator [70], we felt that contaminants formed by, for example, ionization in the accelerator tube subsequent to splash-back from the apertures had not been *convincingly* precluded [71,72]. Finally, we note that with a ~ 100 keV D^+ (~ 300 keV D_3^+) contaminant, for instance, only of order 1 D^+ (D_3^+) per 3000 (10000) clusters [$(D_2O)_{100}^+$ at 1 nA] was needed to produce the fusion rate observed by Beuhler *et al.*

Therefore, from our analyses of Beuhler *et al.*'s data, from the negative theoretical

attempts to explain the observations [71, 73], and from the cluster experiment with *post*-acceleration mass and energy analyses that failed to reproduce the observation [72], we concluded that a light-ion contaminant had not been ruled out. To do such would probably require *post*-acceleration mass and energy analyses. [72]

Two Years Later...

Two years after our article [74] was published, Beuhler *et al.*, after having performed experiments with *post*-acceleration mass and energy analyses, did retrieve their original claims. Indeed, light-ion contaminants were present in their cluster beam.

Appendix B

Evaluation of $\int S \, dV$ and $\int S \, dr$

The fusion source profile S bears the form

$$S = S_o[1 - \tilde{r}^2]^\alpha \, , \tag{B.1}$$

where $\tilde{r}$ is the normalized minor radius. The source-weighted integral $\int S \, dV$ of the plasma volume is evaluated as follows:

$$
\begin{aligned}
\int S \, dV &= \iiint S_o[1 - \tilde{r}^2]^\alpha (R_0 + a\tilde{r}\cos\theta)a^2\tilde{r} \, d\tilde{r} \, d\theta \, d\varphi \\
&= 2\pi \, S_o \iint [1 - \tilde{r}^2]^\alpha (R_0 + a\tilde{r}\cos\theta)a^2\tilde{r} \, d\tilde{r} \, d\theta \\
&= 2\pi \, S_o \left\{ 2\pi \, a^2 \int R_0[1 - \tilde{r}^2]^\alpha \tilde{r} \, d\tilde{r} + a^3 \int [1 - \tilde{r}^2]^\alpha \tilde{r}^2 \, d\tilde{r} \int \cos\theta \, d\theta \right\} \\
&= 4\pi^2 \, a^2 R_0 S_o \frac{-1}{2(\alpha + 1)}[1 - \tilde{r}^2]^{\alpha+1} \Big|_0^1 \\
&= 2\pi^2 \, a^2 R_0 \frac{S_o}{\alpha + 1} = V_{plasma} \frac{S_o}{\alpha + 1} \tag{B.2}
\end{aligned}
$$

To perform the line integral $\int S \, dr$ along a minor radius, it is convenient to rewrite

187

α	4	6	8	10	12
$\sum_{x=0}^{\alpha} \frac{(-1)^x}{2x+1}\binom{\alpha}{x}$	0.406	0.341	0.300	0.272	0.248

Table B.1: Line integral coefficient in Eq. (B.4) *vs.* the source profile peaking factor α.

the source profile as

$$S = S_o \sum_{x=0}^{\alpha} \frac{\alpha!}{x!(\alpha-x)!}(-1)^x \tilde{r}^{2x} = S_o \sum_{x=0}^{\alpha}(-1)^x \binom{\alpha}{x}\tilde{r}^{2x} \ . \qquad (B.3)$$

Therefore, one can write

$$\begin{aligned}
\int S\, dr &= a\int S\, d\tilde{r} \\
&= aS_o \sum_{x=0}^{\alpha}(-1)^x \binom{\alpha}{x} \int \tilde{r}^{2x} d\tilde{r} \\
&= aS_o \sum_{x=0}^{\alpha}(-1)^x \binom{\alpha}{x} \frac{\tilde{r}^{2x+1}}{2x+1}\bigg|_0^1 \\
&= aS_o \sum_{x=0}^{\alpha} \frac{(-1)^x}{2x+1}\binom{\alpha}{x} \qquad (B.4)
\end{aligned}$$

The value of the summation in Eq. (B.4) as a function of the source profile peaking factor α is tabulated in Table B.1.

Bibliography

[1] W. C. Gough. Why Fusion? In M. Kristiansen and M. O. Hagler, editors, *Proc. Symp. Thermonuclear Fusion Reactor Design, Texas Tech University, Lubbock, Texas, June 1970*, number ORO-3778-3, page 256, Springfield, VA, 1971. Clearinghouse for Federal, Scientific, and Technical Information.

[2] J. Wesson. *Tokamaks*. Oxford Engineering Science Series 20. Oxford University Press, Oxford, 1987.

[3] K. Miyamoto. *Plasma Physics for Nuclear Fusion*, chapter 16. MIT Press, Cambridge, MA and London, England, revised english edition, 1989. First (Japanese) edition published by Iwanami Shoten, Tokyo 1976.

[4] F. F. Chen. *Introduction to Plasma Physics and Controlled Fusion*, volume 1. Plenum Press, 2nd edition, 1984.

[5] S. J. Zweben, R. L. Boivin, M. Diesso, S. Hayes, H. W. Hendel, H. Park, and J. D. Strachan. Loss of Alpha-Like MeV Fusion Products from TFTR. *Nucl. Fusion*, **30**(8):1551–1574, 1990.

[6] D. E. Nagle, W. E. Quinn, F. L. Ribe, and W. B. Riesenfeld. Velocity Spectrum of Protons and Tritons from the D-D Reaction in Scylla. *Phys. Rev.*, **119**:857, 1960.

[7] T. J. Murphy and J. D. Strachan. Spatially Resolved Measurement of Alpha Particle Emission from PLT Plasmas Heated by ICRH. *Nucl. Fusion*, **25**(3):383–386, 1985.

[8] R. E. Chrien and J. D. Strachan. D-^{3}He Reaction Measurements During Fast Wave Minority Heating in the PLT Tokamak Experiment. *Phys. Fluids*, **26**(7):1953–1964, July 1983.

[9] W. W. Heidbrink. Fusion Reaction Spectra Produced By Anisotropic ^{3}He Ions During ICRF. *Nucl. Fusion*, **24**(5):636–639, 1984.

[10] G. Martin, O. N. Jarvis, J. Källne, V. Merlo, G. Sadler, and P. van Belle. 15 MeV Proton Emission from JET Plasmas Exhibiting Sawtooth Behaviour: Results and Interpretation. *Phys. Scripta*, **T16**:171–175, 1987.

[11] J. D. Strachan, R. E. Chrien, and W. W. Heidbrink. Measurement of plasma density using nuclear techniques. *J. Vac. Sci. Technol.*, **A1**(2):811–817, Apr–June 1983.

[12] H.-S. Bosch. Diagnostics with Charged Fusion Products in ASDEX. *Rev. Sci. Instrum.*, **61**(6):1699–1707, June 1990.

[13] W. W. Heidbrink and J. D. Strachan. Tokamak Ion Temperature and Poloidal Field Diagnostics Using 3-MeV Protons. *Rev. Sci. Instrum.*, **56**(4):501–518, April 1985.

[14] W. W. Heidbrink, J. Lovberg, J. D. Strachan, and R. E. Bell. Fusion Product Measurements of the Local Ion Temperature Gradient in the PLT Tokamak. *Nucl. Fusion*, **27**(1):129–133, 1987.

[15] H. H. Duong and W. W. Heidbrink. Confinement of Fusion Produced MeV Ions in the DIII-D Tokamak. *Nucl. Fusion*, **33**(2):211–224, 1993.

[16] R. L. Boivin. *Measurements of Charged Fusion Product Diffusion in TFTR*. PhD thesis, Princeton University, Princeton, NJ, 1991.

[17] I. H. Hutchinson, H. Becker, P. Bonoli, N. Diatchenko, S. Fairfax, C. Fiore, R. Granetz, M. Greenwald, D. Gwinn, S. Hakkarainen, D. Humphreys, J. Irby, B. Lipschultz, E. Marmar, D. B. Montgomery, C. Park, R. Parker, N. Pierce, R. Pillsbury, M. Porkolab, J. Ramos, J. Rice, J. Schultz, D. Sigmar, F. Silva, Y. Takase, J. Terry, E. Thibeault, and S. Wolfe. The Physics and Engineering of Alcator C-Mod. Technical Report PFC/RR-88-11, MIT Plasma Fusion Center, Cambridge, Mass., 1988.

[18] C. L. Fiore and R. L. Boivin. Performance of the Neutron Diagnostic System for Alcator C-Mod. *Rev. Sci. Instrum.*, **66**(1):945–947, January 1995.

[19] J. E. Rice and E. S. Marmar. Five-Chord High-Resolution x-Ray Spectrometer for Alcator C-Mod. *Rev. Sci. Instrum.*, **61**(10):2753–2755, 1990.

[20] T. C.-T. Luke. *Measurement of Particle Transport Coefficients on Alcator C-Mod*. PhD thesis, MIT, Cambridge, MA, 1994.

[21] L. L. Lao, H. St. John, R. D. Stambaugh, A. G. Kellman, and W. Pfeiffer. Reconstruction of Current Profile Parameters and Plasma Shapes in Tokamaks. *Nucl. Fusion*, **25**(11):1611–1622, 1985.

[22] J. T. Prud'homme. Texas Nuclear Corporation Neutron Generators. Technical Report Publication No. 5845, Texas Nuclear Corporation, Austin, Texas, March 1962.

[23] K. W. Wenzel, D. H. Lo, R. D. Petrasso, J. W. Coleman, C. K. Li, J. R. Lierzer, C. Borrás, T. Wei, E. Hsieh, and T. Bernat. A Fusion-Product Source. *Rev. Sci. Instrum.*, **63**(10):4837–4839, October 1992.

[24] M. C. Borrás, K. W. Wenzel, D. H. Lo, R. D. Petrasso, D. A. Pappas, C. K. Li, and J. W. Coleman. 14 MeV Neutron Yields from D-T Operation of the MIT Cockcroft-Walton Accelerator. *Journal of Fusion Energy*, **12**(3):317–322, 1993.

[25] K. W. Wenzel, R. D. Petrasso, D. H. Lo, C. K. Li, J. W. Coleman, J. R. Lierzer, E. Hsieh, and T. Bernat. MIT Fusion γ-Ray Diagnostic Development. *Rev. Sci. Instrum.*, **63**(10):4840–4842, October 1992.

[26] C. K. Li, K. W. Wenzel, R. D. Petrasso, D. H. Lo, J. W. Coleman, J. R. Lierzer, E. Hsieh, and T. Bernat. PIXE x Rays: from $Z = 4$ to $Z = 92$. *Rev. Sci. Instrum.*, **63**(10):4843–4845, October 1992.

[27] J. D. Cockcroft and E. T. S. Walton. Experiments with High Velocity Positive Ions–(I) Further Developments in the Method of Obtaining High Velocity Positive Ions. *Proceedings of the Royal Society of London*, **Series A 136**:619–630, 1932.

[28] R. D. Evans. *The Atomic Nucleus.* Krieger, Melbourne, FL, 1982.

[29] W. E. Meyerhof. *Elements of Nuclear Physics.* McGraw-Hill, New York, 1967.

[30] U. Littmark and J. F. Ziegler. *Handbook of Range Distributions for Energetic Ions in All Elements*, volume 6 of *The Stopping and Ranges of Ions in Matter.* Pergamon Press, 1980.

[31] K. Gendreau, M. Bautz, and G. Ricker. Proton Damage in X-Ray CCDs for Space Applications: Ground Evaluation Techniques and Effects on Flight Performance. *Nucl. Instrum. Meth. in Phys. Res. A*, **335**:318–327, 1993.

[32] M. J. Loughlin, J. M. Adams, and G. Sadler. Measurement of the Response Function of a ^{3}He Ionisation Chamber to Monoenergetic Neutrons in the Energy Range from 2.0 to 3.0 MeV. *Nucl. Instrum. Meth. in Phys. Res. A*, **294**(3):606–615, 1990.

[33] Cross-Section Library DOSCROS84, ECN-160, 1984.

[34] D. H. Lo, R. D. Petrasso, K. W. Wenzel, J. W. Coleman, C. K. Li, J. R. Lierzer, E. Hsieh, and T. Bernat. Response of SBDs to MeV Protons, Tritons, and Alphas: Evidence that the Charged-Particle Sensitive Depth is Not Generally the Depletion Depth. *Rev. Sci. Instrum.*, **63**(10):4850–4852, October 1992.

[35] J. F. Ziegler, J. P. Biersack, U. Littmark, and H. H. Andersen. The Stopping and Ranges of Ions in Matter, vol. 1-6, 1977–1985. Based on the series, a FORTRAN computer code called TRIM was written by the authors to simulate ion interaction with matter.

[36] J. D. Jackson. *Classical Electrodynamics*. John Wiley & Sons, Inc., New York, 2nd edition, 1975.

[37] R. A. Langley. Study of the Response of Silicon-Barrier Detectors to Protons and Alpha-Particles. *Nucl. Instrum. Meth.*, **113**(1):109–112, 1973.

[38] T. Elevant, H. W. Hendel, E. B. Nieschmidt, and L. E. Samuelson. Silicon Surface Barrier Detector for Fusion Neutron Spectroscopy. *Rev. Sci. Instrum.*, **57**(8):1763–1765, August 1986.

[39] R. D. Petrasso, M. Gerassimenko, F. H. Seguin, R. Krogstad, and E. S. Marmar. x-Ray Imaging Studies of Alcator-A Radiation and Internal Disruptions. *Nucl. Fusion*, **21**(7):881, 1981.

[40] R. D. Petrasso, D. J. Sigmar, K. W. Wenzel, J. E. Hopf, M. Greenwald, J. L. Terry, and J. Parker. Observation of Centrally Peaked Impurity Profiles Following Pellet Injection in the Alcator-C Tokamak. *Phys. Rev. Lett.*, **57**(6):707, 1986.

[41] K. W. Wenzel and R. D. Petrasso. x-Ray Response of Silicon Surface-Barrier Diodes at 8 and 17.5 keV: Evidence that the x-Ray Sensitive Depth is Not Generally the Depletion Depth. *Rev. Sci. Instrum.*, **59**(8):1380–1387, August 1988.

[42] K. W. Wenzel and R. D. Petrasso. x-Ray Imaging Arrays for Impurity Transport Studies on the Texas Experimental Tokamak. *Rev. Sci. Instrum.*, **61**(2):693–700, February 1990.

[43] G. F. Knoll. *Radiation Detection and Measurement*. John Wiley & Sons, Inc., New York, 2nd edition, 1989.

[44] J. F. Ziegler, G. Cuomo, and J. P. Biersack. Trim-88, a computer code based on the series the stopping and ranges of ions in matter.

[45] IMSL, Houston. *IMSL User's Manual: Math/Library*, softcover edition, 1987.

[46] C. W. Gear. *Numerical Initial-Value Problems in Ordinary Differential Equations*. Prentice-Hall, Englewood Cliffs, New Jersey, 1971.

[47] M. Chen and P. Townsend. Efficient and Consistent Algorithms for Determining the Containment of Points in Polygons and Polyhedra. In G. Maréchal, editor, *Eurographics '87*, pages 423–437. Elsevier Science Publishers B. V., North-Holland, 1987.

[48] S. P. Hakkarainen and J. P. Freidberg. Reconstruction of Vacuum Flux Surfaces from Diagnostic Measurements in a Tokamak. Technical Report PFC/RR-87-22, MIT Plasma Fusion Center, December 1987.

[49] D. L. Book. NRL Plasma Formulary. Naval Research Laboratory, Washington, DC, 1997.

[50] J. Rice. private communication, 1996.

[51] R. E. Chrien. *Measurements of Fusion Reactions from a Tokamak Plasma*. PhD thesis, Princeton University, Princeton, NJ, 1981.

[52] W. W. Heidbrink. *Tokamak Diagnostics Using Fusion Products*. PhD thesis, Princeton University, Princeton, NJ, 1984.

[53] S. Wolfe. private communication, 1996.

[54] G. Knorr. Equilibrium of a Toroidal Plasma with Finite Resistivity and Inertia. *Phys. Fluids*, **8**:1334, 1965.

[55] Y. I. Kolesnichenko. The Role of Alpha Particles in Tokamak Reactors. *Nucl. Fusion*, **20**(6):727–780, June 1980.

[56] D. Anderson, H. Hamnén, and M. Lisak. Thermonuclear Tokamak Plasmas in the Presence of Fusion Alpha Particles. Technical Report EUR-FU/80/88-91, NET, December 1988.

[57] G. Lehner. Reaction Rates and Energy Spectra for Nuclear Reactions in High Energy Plasmas. *Z. Physik*, **232**:174–189, 1970.

[58] H. H. Andersen and J. F. Ziegler. *Hydrogen: Stopping Powers and Ranges in All Elements*, volume 3 of *The Stopping and Ranges of Ions in Matter*. Pergamon Press, New York, 1977.

[59] W. K. Chu. Calculation of Energy Straggling for Protons and Helium Ions. *Phys. Rev. A*, **13**(6):2057, June 1976.

[60] J. W. Mayer and E. Rimini. *Ion Beam Handbook for Material Analysis*. Academic, New York, 1977.

[61] J. Kemmer and R. Hofmann. Determination of the Energy Straggling of Am-Alpha Particles in Aluminum Foils. *Nucl. Instrum. Meth.*, **176**(3):543–544, 1980.

[62] E. Strom and H. I. Israel. Photon Cross Sections from 0.001 to 100 MeV for Elements 1 through 100. Technical Report LA-3753, Los Alamos Scientific Laboratory, Los Alamos, New Mexico, June 1967.

[63] J. Briesmeister. MCNP-A General Monte Carlo Code for Neutron and Photon Transport. Technical Report LA-7396-m, Rev. 2, Los Alamos National Laboratory, September 1986.

[64] D. I. Garber and R. R. Kinsey. Neutron Cross Sections: Volume II, Curves. Technical Report BNL 325, National Neutron Cross Section Center, Brookhaven National Laboratory, Upton, New York 11973, January 1976.

[65] G. Sadler, O. N. Jarvis, P. van Belle, and M. Pillon. Use of the ^{28}Si(n,p)^{28}Al Reaction for the Measurement of 14 MeV Neutrons from Fusion Plasmas. *Rev. Sci. Instrum.*, **61**(10):3175–3177, October 1990.

[66] A. E. Profio. *Radiation Shielding and Dosimetry*. John Wiley & Sons, Inc., New York, 1979.

[67] C. L. Fiore and R. S. Granetz. Neutron Diagnostic Experiment for Alcator C-Mod. *Rev. Sci. Instrum.*, **61**(10):3166–3168, October 1990.

[68] R. J. Beuhler, G. Friedlander, and L. Friedman. Cluster-Impact Fusion. *Phys. Rev. Lett.*, **63**(12):1292, September 1989.

[69] R. J. Beuhler, Y. Y. Chu, G. Friedlander, L. Friedman, and W. Kunnmann. Deuteron-Deuteron Fusion by Impact of Heavy-Water Clusters on Deuterated Surfaces. *J. Phys. Chem.*, **94**(19):7665, 1990.

[70] R. J. Beuhler, Y. Y. Chu, G. Friedlander, L. Friedman, J. G. Alessi, V. LoDestro, and J. P. Thomas. Cluster-Impact Fusion: Time-of-Flight Experiments. *Phys. Rev. Lett.*, **67**(4):473, July 1991.

[71] M. H. Shapiro and T. A. Tombrello. Simulation of Cluster Impacts on Metallic Surfaces. *Phys. Rev. Lett.*, **65**(1):92, July 1990.

[72] M. Fallavier, J. Kemmler, R. Kirsch, J. C. Poizat, J. Remillieux, and J. P. Thomas. Search for Nuclear Fusion in Deuterated Targets Under Cluster-Beam Impact. *Phys. Rev. Lett.*, **65**(5):621, July 1990.

[73] C. Carraro, B. Q. Chen, S. Schramm, and S. E. Koonin. Estimates of Cluster-Impact Fusion Yields. *Phys. Rev. A*, **42**(3):1379, August 1990.

[74] D. H. Lo, R. D. Petrasso, and K. W. Wenzel. Comment on 'Cluster-Impact Fusion'. *Phys. Rev. Lett.*, **68**(13):2107, March 1992.